

# GEODESIC TRACTOGRAPHY SEGMENTATION FOR DIRECTIONAL MEDICAL IMAGE ANALYSIS

A Dissertation  
Presented to  
The Academic Faculty

by

John Melonakos

In Partial Fulfillment  
of the Requirements for the Degree  
Doctor of Philosophy in the  
School of Electrical and Computer Engineering

Georgia Institute of Technology  
May 2009

# GEODESIC TRACTOGRAPHY SEGMENTATION FOR DIRECTIONAL MEDICAL IMAGE ANALYSIS

Approved by:

Professor Allen Tannenbaum, Advisor  
School of Electrical and Computer  
Engineering  
*Georgia Institute of Technology*

Professor Patricio Vela  
School of Electrical and Computer  
Engineering  
*Georgia Institute of Technology*

Professor Jeff Shamma  
School of Electrical and Computer  
Engineering  
*Georgia Institute of Technology*

Professor Christopher F. Barnes  
School of Electrical and Computer  
Engineering  
*Georgia Institute of Technology*

Professor Marc Niethammer  
Department of Computer Science  
*University of North Carolina at Chapel  
Hill*

Date Approved: October 30, 2008

## **ACKNOWLEDGEMENTS**

Content of this page has been redacted.

# TABLE OF CONTENTS

ACKNOWLEDGEMENTS . . . . .	iii
LIST OF FIGURES . . . . .	vii
SUMMARY . . . . .	x
I INTRODUCTION . . . . .	1
1.1 Organization of this Thesis . . . . .	1
II FINSLER ACTIVE CONTOURS . . . . .	4
2.1 Introduction . . . . .	4
2.2 Energy Minimizing Curves . . . . .	8
2.2.1 Geodesic (Conformal) Active Contours . . . . .	8
2.2.2 Dynamic Programming . . . . .	9
2.3 Geodesic Active Contours in a Finsler Metric . . . . .	10
2.3.1 Evolving space curves . . . . .	10
2.3.2 First variation . . . . .	12
2.4 Direction-Dependent Dynamic Programming . . . . .	13
2.4.1 Optimal control and the principal of optimality . . . . .	14
2.4.2 Numerics . . . . .	15
2.5 Applications and Simulations . . . . .	17
2.5.1 Closed curves evolving according to the Finsler flow . . . . .	17
2.5.2 Simulated Example . . . . .	19
2.5.3 Curve Detection in Imagery . . . . .	21
2.5.4 High angular diffusion MRI tractography . . . . .	22
2.5.5 A Note on Timings . . . . .	29
2.6 Conclusions . . . . .	29
III FINSLER TRACTOGRAPHY . . . . .	31
3.1 Introduction . . . . .	31
3.2 The Cingulum Bundle . . . . .	33

3.3	Anchor Tracts on a Finsler Manifold . . . . .	34
3.4	Level Set Fiber Bundle Segmentation . . . . .	36
3.5	Experiments & Results . . . . .	37
3.6	Conclusions & Future Work . . . . .	39
IV	DW-MRI VOLUMETRIC SEGMENTATION . . . . .	41
4.1	Introduction . . . . .	41
4.2	Background . . . . .	42
4.3	The Cingulum Bundle . . . . .	44
4.4	The Algorithm . . . . .	45
4.4.1	Motivation for Local Constraints . . . . .	46
4.4.2	Prior Work . . . . .	46
4.4.3	Bayesian Framework . . . . .	48
4.5	Experiments . . . . .	52
4.6	Tensor Warping . . . . .	56
4.6.1	Motivation and Algorithm . . . . .	56
4.6.2	Results . . . . .	57
4.7	Conclusions . . . . .	61
V	BRAIN MRI TISSUE CLASSIFICATION . . . . .	64
5.1	Introduction . . . . .	64
5.2	Bayesian Classification Algorithms . . . . .	65
5.2.1	2D Tracking Algorithms . . . . .	66
5.2.2	Volumetric Medical Image Classification . . . . .	67
5.2.3	Tissue Tracking . . . . .	67
5.3	Experiment . . . . .	70
5.4	Results . . . . .	71
5.5	Conclusion . . . . .	73
VI	BAYESIAN METHODS IN COLON CAD . . . . .	75
6.1	Introduction . . . . .	75

6.2	Shape from Principal Curvatures . . . . .	76
6.2.1	The Geometric Model . . . . .	77
6.2.2	Distribution of Curvatures . . . . .	78
6.3	Experiments and Results . . . . .	80
6.4	Conclusions and Future Work . . . . .	82
VII	CONCLUSION . . . . .	85
APPENDIX A	FINSLER FOR NON-CONVEX FUNCTIONS . . . . .	87
APPENDIX B	FINSLER FLOW IN TERMS OF $F$ . . . . .	90
REFERENCES	. . . . .	94

## LIST OF FIGURES

1	Synthetic 2D example. These three different local costs depend only on direction. They are represented as polar plots (first row). The corresponding deforming shapes are presented on the following rows (black). The initial curve (gray dashed) is bean-shaped. See text. . .	18
2	Simulated 2D example: (a) The synthetic baseline 'L' shaped corner, (b) Finsler results (red), Riemannian results (green), Isotropic results (blue), (c) A zoomed-in view showing the directional data of 9 pixels surrounding the corner, (d) A zoomed-in view showing the Riemannian image of 9 pixels surrounding the corner, created by applying the Stejskal-Tanner equation to the directional data . . . . .	20
3	Road image and manually determined curve used for learning the pattern detector. . . . .	23
4	Particle-based Curve Evolution with Different Initializations . . . . .	24
5	Results of road detection on noisy images using dynamic programming.	24
6	Curve evolution on a real image. The local cost is determined using a pattern detector. . . . .	25
7	Vessel detection using dynamic programming. The procedure was run independently for two seed points (large discs) and several target points (small discs). On the right, noise was added. This changes the recovered curves as one of the branches at the bottom is no longer visible.	25
8	Cost per unit length of end points of optimal curves for different $b$ -values is a validity index. Best results are achieved for the highest $b$ -value. . . . .	27
9	Fiber tracking from high angular resolution dataset ( $b=1500 \text{ s/mm}^2$ ).	27
10	Proposed technique on high angular resolution data (blue) compared with streamline technique on tensor field (red) ( $b=1500 \text{ s/mm}^2$ ). . . .	27
11	Cingulum Bundle Anchor Tracts from: (a) detailed view of a normal control case, (b) streamline example on a schizophrenic case. . . . .	38
12	Cingulum Bundle Anchor Tracts: (a) anterior and (b) posterior views of a normal control case. . . . .	39
13	Cingulum bundle level set segmentation result on a schizophrenic case.	39

14	Example of the need for local constraints on region-based segmentation algorithms which attempt to segment the cingulum bundle. Notice that tensor anisotropy and orientation vary across the length of the cingulum bundle. . . . .	47
15	The prior profile: Blue is the initial step function, Red is the actual profile after smoothing. Note the region of uniform priors (0.5), centered around the clinically defined mean fiber radius. . . . .	53
16	The prior energy (left), likelihood energy (middle), and posterior energy (right). . . . .	54
17	A 3D view of the result. . . . .	54
18	Front evolution time steps: Top Row is the evolution with only the priors. Middle Row is the evolution with only the likelihoods. Bottom Row is the evolution from the Bayesian inclusion of both the likelihoods and priors. . . . .	55
19	Tensor reorientation concept. The spatially varying tensor orientation can largely be removed by reorientation with respect to a representative fiber tract (blue). . . . .	57
20	Segmentation of a synthetic example. Reorienting diffusion information based on the representative streamline (top left) result in almost uniform tensor distributions interior and exterior to the fiber bundle. While segmentation for the original data is difficult and leads to unsatisfactory results, segmentation of the reoriented data is much easier leading to a faithful segmentation with the proposed approach. . . . .	59
21	Sagittal slice of the cingulum bundle, before and after tensor reorientation. The cingulum bundle appears more uniform in direction (green) after reorientation. Reorientation greatly improves the segmentation result of the proposed approach. . . . .	60
22	Effect of reorientation on orientation and segmentation, depicted for a posterior coronal slice. Reorientation results in a consistent orientation of the cingulum bundle changing from blue to green, indicating a directional change from inferior-superior to posterior-anterior. While segmentation using the proposed approach fails for the original data it succeeds after reorientation. . . . .	61
23	Superior coronal slices: Original data; results for streamline (S) and full brain streamline (FBS) tractography, for the proposed segmentation on original data (O) and on reoriented data (RO). Only the proposed approach segments up to the perceived bundle boundary in orientation space. . . . .	62
24	Medical Image Classification Strategies . . . . .	65

25	Tissue Tracking General Structure . . . . .	68
26	Tissue Tracking Algorithm . . . . .	69
27	Overlap of Gray Voxels for Each Brain Scan . . . . .	72
28	Overlap of White Voxels for Each Brain Scan . . . . .	73
29	Case 5-8, Slice 36 . . . . .	74
30	Case 4-8, Slice 12 . . . . .	74
31	Case 11-2, Slice 44 . . . . .	74
32	<i>The Curvature Computation System</i> . . . . .	77
33	<i>The Haustra Model</i> . . . . .	78
34	<b>Partitioning of <math>\kappa_1</math>-<math>\kappa_2</math> space with overlying scatter plot data:</b> <i>(a) Model-based partitioning of <math>\kappa_1</math>-<math>\kappa_2</math> space, red = pedunculated polyps, green = sessile and flat polyps, blue = haustral folds, yellow = haustra, (b) Binary partitioning of <math>\kappa_1</math>-<math>\kappa_2</math> space, red = polyp responses, blue=non-polyp responses . . . . .</i>	80
35	<b>Visual Haustra Results:</b> <i>(a) polyp responses without the haustra model in a window centered at an actual polyp, (b) polyp responses with the haustra model, (c) haustra responses alone, and (d) Raw image data</i>	81
36	<i>ROC curve for the performance of a colon CAD system using the proposed haustra model. A sensitivity of 83% is achieved ad a cost of 6.25 false positive detections per case. . . . .</i>	83
37	Slicer3 Integration. The Geodesic Tractography Segmentation module. Currently under development. . . . .	85

## SUMMARY

Medical image analysis algorithms aim at increasing the speed, accuracy, and reliability by which medical images are processed and ultimately understood. Active contour and energy minimization techniques are commonly used in medical image analysis applications. The results of these techniques are *optimal* under certain assumptions and provide meaningful clinical insights.

In this thesis, we develop energy minimization techniques for medical image analysis. The primary focus of this thesis is the construction of a theoretical and applied framework for:

- *Geodesic Tractography*: In this work, we develop a mathematical framework for finding optimal paths in oriented domains. In oriented domains, image data depends both upon position and upon direction. In other words, for each position and direction in the domain there exists a unique voxel intensity. The use of a Finsler metric is shown to be particularly suited for this type of problem. In fact, we show that the Finsler condition is necessary to ensure that the flow is well-posed. The development of this theory is couched in an application to diffusion-weighted magnetic resonance imagery (DW-MRI). It is shown that representative or anchor tracts are found which optimally connect two regions of interest in the brain.
- *Tractography Segmentation*: In this work, we show how these optimal paths may be used to initialize a volumetric segmentation which captures neural fiber bundles. We present a key problem for volumetric segmentation along with two approaches for overcoming this problem: via either a local constraining of

statistics or a tensor warping preprocessing step.

Also, in this work, we present medical image analysis algorithms using Bayesian segmentation frameworks. In the first, we present our work on the segmentation of brain MRI tissue into tissue classes. In the second, we present the construction of a model of colon haustra for use in computer-aided detection (CAD) within a Bayesian framework.

The core software components of this thesis are being made available in the NAMI-MIC toolkit (see <http://www.na-mic.org>).

# CHAPTER I

## INTRODUCTION

Geodesic Tractography Segmentation is the two component approach presented in this thesis for the analysis of imagery in oriented domains, with emphasis on the application to diffusion-weighted magnetic resonance imagery (DW-MRI). The computer-aided analysis of DW-MRI data presents a new set of problems and opportunities for the application of mathematical and computer vision techniques. The goal is to develop a set of tools that enable clinicians to better understand DW-MRI data and ultimately shed new light on biological processes.

This thesis presents a few techniques and tools which may be used to automatically find and segment major neural fiber bundles from DW-MRI data. For each technique, we provide a brief overview of the advantages and limitations of our approach relative to other available approaches.

### ***1.1 Organization of this Thesis***

This thesis is organized into the following chapters:

- *Chapter 2:* In this chapter, we propose an image segmentation technique based on augmenting the conformal (or geodesic) active contour framework with directional information [59]. In the isotropic case, the Euclidean metric is locally multiplied by a scalar conformal factor based on image information such that the weighted length of curves lying on points of interest (typically edges) is small. The conformal factor which is chosen depends only upon position and is in this sense isotropic. While directional information has been studied previously for other segmentation frameworks, here we show that if one desires to

add directionality in the conformal active contour framework, then one gets a well-defined minimization problem in the case that the factor defines a Finsler metric. Optimal curves may be obtained using the calculus of variations or dynamic programming based schemes. Finally we demonstrate the technique by extracting neural tracts from diffusion-weighted magnetic resonance imagery.

- *Chapter 3:* In this chapter, we present a novel approach for the segmentation of white matter tracts based on Finsler active contours [57]. This technique provides an optimal measure of connectivity, explicitly segments the connecting fiber bundle, and is equipped with a metric which is able to utilize the directional information of high angular resolution data. We demonstrate the effectiveness of the algorithm for segmenting the cingulum bundle.
- *Chapter 4:* In this chapter, we present an approach for the volumetric segmentation of neural fiber bundles from DW-MRI data [58]. We describe a method for segmenting fiber bundles from diffusion-weighted magnetic resonance images using a locally-constrained region based approach. From a pre-computed optimal path, the algorithm propagates outward capturing only those voxels which are locally connected to the fiber bundle. Rather than attempting to find large numbers of open curves or single fibers, which individually have questionable meaning, this method segments the full fiber bundle region. The strengths of this approach include its ease-of-use, computational speed, and applicability to a wide range of fiber bundles. In this work, we show results for segmenting the cingulum bundle. Finally, we explain how this approach and extensions thereto overcome a major problem that typical region-based flows experience when attempting to segment neural fiber bundles.
- *Chapter 5:* In this chapter, we present an approach for the segmentation of brain MRI tissue into gray matter, white matter, and cerebral spinal fluid [55].

Bayesian classification methods have been extensively used in a variety of image processing applications, including medical image analysis. The basic procedure is to combine data-driven knowledge in the likelihood terms with clinical knowledge in the prior terms to classify an image into a pre-determined number of classes. In many applications, it is difficult to construct meaningful priors and, hence, homogeneous priors are assumed. In this chapter, we show how expectation-maximization weights and neighboring posterior probabilities may be combined to make intuitive use of the Bayesian priors. Drawing upon insights from computer vision tracking algorithms, we cast the problem in a *tissue tracking* framework. We show results of our algorithm on the classification of gray and white matter along with surrounding cerebral spinal fluid in brain MRI scans. We show results of our algorithm on 20 brain MRI datasets along with validation against expert manual segmentations. In particular, the white matter segmentation may be used as a mask for the guidance and constraint of the geodesic tractography segmentation algorithms presented in the previous chapters.

- *Chapter 6:* In this chapter, we present a bayesian probabilistic model for haustral curvatures with applications to colon CAD [56]. Among the many features used for classification in computer-aided detection (CAD) systems targeting colonic polyps, those based on differences between the shapes of polyps and folds are most common. We introduce here an explicit parametric model for the *haustra* or colon wall. The proposed model captures the overall shape of the haustra and we use it to derive the probability distribution of features relevant to polyp detection. The usefulness of the model is demonstrated through its application to a colon CAD algorithm.

## CHAPTER II

### FINSLER ACTIVE CONTOURS

In this chapter, we propose an image segmentation technique based on augmenting the conformal (or geodesic) active contour framework with directional information [59]. In the isotropic case, the Euclidean metric is locally multiplied by a scalar conformal factor based on image information such that the weighted length of curves lying on points of interest (typically edges) is small. The conformal factor which is chosen depends only upon position and is in this sense isotropic. While directional information has been studied previously for other segmentation frameworks, here we show that if one desires to add directionality in the conformal active contour framework, then one gets a well-defined minimization problem in the case that the factor defines a Finsler metric. Optimal curves may be obtained using the calculus of variations or dynamic programming based schemes. Finally we demonstrate the technique by extracting neural tracts from diffusion-weighted magnetic resonance imagery.

#### ***2.1 Introduction***

Geodesic active contours [43, 14] have proven to be a very useful tool for a number of segmentation tasks. Basically, the idea is to define an active contour model based on the theory of conformal metrics and on Euclidean curve shortening evolution. This type of curve evolution defines the gradient direction to be that for which a curve will shrink as fast as possible relative to its Euclidean arc-length. One multiplies the Euclidean arc-length by a conformal factor defined by the features of interest which one wants to extract and then computes the corresponding gradient evolution equations. The features which one wants to capture therefore lie at the bottom of a potential well to which the initial contour will flow. The key point is that the

conformal structure defines a Riemannian metric in the plane for which the features of interest appear as closed geodesic curves.

In this chapter, motivated by certain problems in pattern detection and medical imaging, we develop a version of geodesic active contours in a *Finsler metric* [4, 96]. See our discussion in Section 2.3 below for the formal mathematical definition. The basic idea is that directionality is added to the active contours which allows for the segmentation of image data in oriented domains. As alluded to above, isotropic active contour models have been used to segment image data in isotropic domains, meaning that the value of each voxel depends only upon its position in the domain and *not* upon an associated direction. However, in oriented domains, image data depends *both* upon position and direction. In other words, for each position and direction in the domain there exists a unique voxel intensity. It is then that the concept of the Finsler metric becomes crucial. In fact, if one desires to add directionality to the geodesic active contour framework, we show that the Finsler condition is necessary to ensure that the flow is well-posed.<sup>1</sup> We show that there are some applications for which the Finsler metric outperforms the Riemannian metric, but certainly there are others for which the Riemannian metric may be more desirable. For oriented domains, as long as the metric satisfies the Finsler condition, the choice of a particular metric is subject to the given application.

Flows relative to anisotropic metrics have been studied in the mathematics and physics literature; see [2, 25] and the references therein. A very simple directional flow was proposed in some of our earlier work; see [80].

There are many applications of image data in oriented domains. Examples include diffusion-weighted magnetic resonance imaging in which the magnetic field is biased in several directions in order to measure the water diffusivity of biological tissue. In this case, for each position in the tissue and for each direction of the bias field, the

---

<sup>1</sup>Note that the Riemannian metric satisfies the Finsler conditions and is well-posed.

corresponding image intensity provides a measure of water diffusivity at that position and direction.

Furthermore, this technique may be used in pattern detection. Consider a small image pattern patch which we desire to match to our image. Through translations and rotations of the patch throughout the image, we can evaluate a measure of similarity between the patch and the image for the given patch position and direction. Thus, this is also a problem in an oriented domain because for each position and rotation of the patch there exists a unique measure of similarity.

Geodesic active contours in the Finsler framework provide a mechanism for the minimization of energy functionals defined on oriented domains. We derive both the curve evolution and dynamic programming based implementations for Finsler active contours. The latter is necessary since we will want to consider the evolution of open curves for which the level set methodology is not appropriate. Preliminary results for directional-dependent segmentations may be found in [82, 81].

The idea of using Finsler type metrics for various purposes is of course not original in this work. First of all regarding curve shortening, Gage [25] has considered curvature driven flows in a Minkowski space. General mean curvature flows relative to Finsler metrics are studied in [8]. Gurtin and Angenent have proposed the use of anisotropic Finsler flows for problems in crystal growth in [2]. In the computer vision literature such directionally-dependent metrics have appeared in [44, 110, 12, 46, 11]. In some nice work, the connections of graph cuts and such metrics have been described in [12, 46, 11]. Geodesic active contours and graph cut methods have been combined in [46, 12]. Further, in [46] the explicit connection between Finsler distances and the flux methods of [110] is considered in some detail.

This chapter continues the above line of research. Here we describe Finsler flows in a completely continuous setting valid for both open and closed curves embedded in a Euclidean space of *any* dimension. The key observation is that if one defines a

conformal active contour flow for a direction-dependent conformal factor, then in order for the flow to be well-defined, one needs the standard Finsler convexity condition (see Section 2.3). Without this condition, the flow will be a backwards heat equation. Thus, this present work extends the results of [43, 14] who consider conformally Euclidean metrics which only depend on position, and are in this sense *isotropic*. (In this chapter, we will follow the standard terminology of the mean curvature flow literature in which *isotropic* flows are defined relative to a Riemannian metric while *anisotropic* flows are defined relative to a direction-dependent Finsler metric; see [4].) It is important to note that while one can get *directionality* in the Riemannian framework for image segmentation by a suitable choice of metric (ellipses have directionality), nevertheless, we believe that the Finsler geodesic active contour approach gives a natural way of performing segmentation in oriented domains.

We now summarize the contents of this chapter. In Section 2.2, we review the theory of energy minimizing flows and geodesic active contours as well as dynamic programming. Section 2.3 is the key part of this chapter. Here we define the notion of a Finsler metric and derive the geodesic active contour flow relative to such a structure. In Section 2.4, we describe the dynamic programming based solution and the numerical implementation of such an approach. In Section 2.5, we show results of experiments using these techniques on both MRI tractography and pattern detection applications. In Section 2.6, we draw some conclusions and describe some future research directions. Finally, we have included two mathematical appendices. The first justifies the use of dynamic programming in our situation in which we have a data driven anisotropic conformal factor, and the second gives another derivation of the Finsler geodesic flow which also captures some of its interesting properties.

## 2.2 *Energy Minimizing Curves*

Energy minimization approaches to image segmentation have been very popular; see [63, 73, 92, 89] and the references therein. These approaches allow one to define a meaningful energy for a given application and to systematically construct contours which minimize the energy. In this section, we describe two of the key approaches for the minimization of such energy functionals: conformal active contours (based on gradient descent) and dynamic programming. The former works for closed curves, while the latter method is valid for curves in which we fix seed and target regions as well.

### 2.2.1 Geodesic (Conformal) Active Contours

In the conformal (or geodesic) active contour model, a local cost,  $\psi : \mathbf{R}^2 \rightarrow \mathbf{R}^+$ , is defined based on image information [43, 14]. For a given curve  $\Gamma$  the total cost  $\mathcal{L}(\Gamma)$  is defined as the integration of local costs along the curve:

$$\mathcal{L}_\psi(\Gamma) \triangleq \int_\Gamma \psi(\Gamma) \, ds. \quad (1)$$

This energy can be interpreted as the  $\psi$ -weighted length of the curve. Minimal curves will therefore tend to go through regions where  $\psi$  is small while at the same time constraining the total conformal Euclidean length to be as small as possible. Convergence of this flow is studied in [43, 14]. It is important to note that  $s$  is the arc-length parameterization and, therefore, this energy is purely geometric.

If the curve is closed or has fixed end points, a partial differential equation is obtained by calculus of variations that continuously deforms an initial curve  $\Gamma(t=0)$  in a way that optimally minimizes its total cost  $\mathcal{L}$ . This can be interpreted as a gradient descent on the infinite dimensional space of curves.

In the case of the functional (1), the PDE that deforms a given curve in order to minimize the energy as fast as possible in the  $L_2$  sense is

$$\frac{\partial \Gamma}{\partial t} = -(\nabla \psi \cdot \mathbf{N})\mathbf{N} + \psi \Gamma_{ss}, \quad (2)$$

where  $\mathbf{N}$  denotes the unit inward normal.

As is standard, this may be implemented using level set methods [73, 92].

### 2.2.2 Dynamic Programming

Mortensen *et al.* [66] have proposed the *live-wire segmentation* technique that also determines optimal curves for the same kind of functional. Their framework is based on dynamic programming and is applicable to curves with one end fixed in a given seed region  $S$ .

The underlying principle of dynamic programming is the *principle of optimality* verified by minimum-cost problems such as (1) (assuming an optimal curve exists). The principle is that any subpath  $p$  of an optimal path  $P$  is itself optimal (otherwise the  $P$  could be improved by following another subpath  $p'$  instead of  $p$ ). This leads to the definition of the *value function*  $\mathcal{L}^*$  which is the minimal cost to reach the seed region  $S$  from any point  $x$  of the domain.

$$\mathcal{L}^*(x) \triangleq \min\{ \mathcal{L}(\Gamma), \Gamma(0) = x, \Gamma(1) \in S \}$$

In problems such as (1), the value function satisfies the Eikonal equation  $|\nabla \mathcal{L}^*(x)| = \psi(x)$  with boundary condition  $\mathcal{L}^* = 0$  on  $S$ . This equation can be solved numerically using the fast marching algorithm [106, 92] or can be discretely approximated using Dijkstra's algorithm.

From any point in the domain, an optimal curve in the sense of (1) can then be determined by gradient descent on the scalar field  $\mathcal{L}^*$ .

### 2.3 Geodesic Active Contours in a Finsler Metric

In this section, we introduce the notion of direction-dependent active contours. This is essentially a version of active contours defined relative to a Finsler rather than a Riemannian metric. If one thinks of a Riemannian metric as being defined by a continuously varying family of inner products on the tangent bundle of a given manifold, a Finsler metric is given by a continuously varying family of Banach space norms. The strict convexity property given below is then an expression of the fact that these norms must satisfy the triangle inequality. More mathematical details about Finsler flows may be also be found in Appendix B.

For an excellent exposition of the Finsler property and comparisons to the Riemannian structure, we refer the interested reader to [96]. Finally, we should note that versions of curve shortening relative to the Finsler structure have been studied in [25, 2, 3, 70].

#### 2.3.1 Evolving space curves

In this section, we set up notations and define the notion of the *Finsler metric*.

Consider a family of evolving curves of the form  $\Gamma : [0, 1] \times [0, T) \rightarrow \mathbf{R}^n$ . For any curve  $\Gamma(x, t)$  we denote

$$\mathbf{T} = \frac{\Gamma_x}{|\Gamma_x|}, \quad \frac{\partial}{\partial s} = \frac{1}{|\Gamma_x|} \frac{\partial}{\partial x}, \quad ds = |\Gamma_x| dx.$$

The curvature vector of  $\Gamma$  is

$$\mathbf{K} = \Gamma_{ss} = \frac{\partial^2 \Gamma}{\partial s^2}.$$

We say that the curve *evolves normally* if

$$\mathbf{V} = \frac{\partial \Gamma}{\partial t} \perp \mathbf{T}$$

holds always. For such curve evolutions one has

$$\partial_t \mathbf{T} = \partial_s \mathbf{V}, \quad \left[ \frac{\partial}{\partial t}, \frac{\partial}{\partial s} \right] = (\mathbf{K} \cdot \mathbf{V}) \frac{\partial}{\partial s}, \quad \text{and} \quad \frac{\partial}{\partial t} ds = -(\mathbf{K} \cdot \mathbf{V}) ds. \quad (3)$$

For any given function

$$\psi : \mathbf{R}^n \times S^{n-1} \rightarrow \mathbf{R}^+,$$

we let

$$\mathcal{L}(\Gamma) = \int_0^L \psi(\Gamma, \mathbf{T}) ds = \int_{x=0}^1 \psi\left(\Gamma, \frac{\Gamma_x}{|\Gamma_x|}\right) |\Gamma_x| \, dx,$$

where  $L$  is the length of  $\Gamma$ . The infinitesimal length function  $\psi$  is only defined on unit vectors, but one can extend it naturally to all vectors by requiring it to be positively homogeneous of degree 1. We denote this extension by

$$F(p, v) = |v| \psi\left(x, \frac{v}{|v|}\right)$$

so that the anisotropic length of  $\Gamma$  is

$$\mathcal{L}(\Gamma(\cdot, t)) = \int_0^1 F(\Gamma, \Gamma_x) \, dx. \quad (4)$$

Because of the homogeneity of  $F$ , i.e.,

$$F(p, tv) = tF(p, v) \text{ for all } x, v \in \mathbf{R}^n \text{ and } t \geq 0,$$

the anisotropic length is invariant under orientation preserving reparametrizations of the curve [96]. However,  $\mathcal{L}(\Gamma)$  may change if one reverses the orientation of  $\Gamma$ .

The extended anisotropic length function  $F(p, v)$  is never a strictly convex function of  $v$ , because it is homogeneous of degree 1. If  $F(p, v)^2$  is strictly convex, then  $F$  defines a *Finsler metric* on  $\mathbf{R}^n$  [4, 96]. A necessary and sufficient condition for this to occur is that  $\nabla_\theta^2 F(p, \theta)$  be positive definite on the subspace  $\{v \in \mathbf{R}^n : v \perp \theta\}$ . We compute this second derivative at the particular vector  $\theta = (1, 0, \dots, 0)$  in terms of  $\psi$ . (See [18] for a proof.)

**LEMMA 1.** *If  $f : S^{n-1} \rightarrow \mathbf{R}$  is a  $C^2$  function, and if  $F(v) = |v|f(v/|v|)$ , then for any  $v \in S^{n-1}$  and any pair of tangent vectors  $X, Y \in T_v S^{n-1}$  one has*

$$\nabla_{X,Y}^2 F(v) = (X, Y)f(v) + \nabla_{X,Y}^2 f(v)$$

where  $\nabla^2 f$  is the second covariant derivative of  $f : S^{n-1} \rightarrow \mathbf{R}$ .

If  $v \neq 0$  is not necessarily a unit vector, then one has

$$\nabla_{X,Y}^2 F(v) = \frac{1}{|v|} \{ (X, Y) f(v) + \nabla_{X,Y}^2 f(v) \}.$$

It follows that  $\psi$  defines a Finsler metric if and only if the quadratic form defined by  $g_{ij}\psi + \nabla_i \nabla_j \psi$  is positive definite.

### 2.3.2 First variation

We can now compute the first variation of our anisotropic length functional, and derive the flow for the Finsler geodesic active contours. In this discussion, we assume that the curves are closed or that curves under consideration have fixed end-points.

Assuming the curve  $\Gamma$  evolves normally, one has

$$\begin{aligned} \frac{d}{dt} \mathcal{L}(\Gamma) &= \frac{d}{dt} \int \psi(\Gamma, \mathbf{T}) \, ds \\ &= \int \{ \mathbf{V} \cdot \psi_p(\Gamma, \mathbf{T}) + (\partial_t \mathbf{T}) \cdot \psi_v(\Gamma, \mathbf{T}) - \psi(\Gamma, \mathbf{T}) \mathbf{K} \cdot \mathbf{V} \} \, ds, \end{aligned}$$

where  $\psi_p$  and  $\psi_v$  denote derivatives with respect to the first and second variables in  $\psi(p, v)$ . The derivative with respect to  $v \in S^{n-1}$  is a covariant derivative. We use (3) to conclude

$$\begin{aligned} \frac{d}{dt} \mathcal{L}(\Gamma) &= \int \{ \mathbf{V} \cdot \psi_p(\Gamma, \mathbf{T}) + \mathbf{V}_s \cdot \psi_v(\Gamma, \mathbf{T}) - \psi(\Gamma, \mathbf{T}) \mathbf{K} \cdot \mathbf{V} \} \, ds \\ &= \int \{ \mathbf{V} \cdot \psi_v(\Gamma, \mathbf{T}) - \mathbf{V} \cdot \partial_s (\psi_v(\Gamma, \mathbf{T})) - \psi(\Gamma, \mathbf{T}) \mathbf{K} \cdot \mathbf{V} \} \, ds \\ &= - \int \mathbf{V} \cdot \{ \partial_s (\psi_v(\Gamma, \mathbf{T})) + \psi(\Gamma, \mathbf{T}) \mathbf{K} - \psi_p(\Gamma, \mathbf{T}) \} \, ds, \end{aligned}$$

so that you get steepest descent with

$$\mathbf{V} = [\partial_s (\psi_v(\Gamma, \Gamma_s)) - \psi_p(\Gamma, \Gamma_s)]^\perp + \psi(\Gamma, \Gamma_s) \Gamma_{ss}. \quad (5)$$

Here  $X^\perp$  denotes the component of  $X$  which is perpendicular to  $\Gamma_s = \mathbf{T}$ .

Note that  $\psi_v(\Gamma, v) \in T_v S^{n-1}$  is a vector perpendicular to  $v$  since it is the gradient of a function on  $S^{n-1}$  at the point  $v \in S^{n-1}$ . If you expand the derivative

$\partial_s(\psi_v(\Gamma, \Gamma_s))$  you will get two terms, one of which contains second derivatives of  $\Gamma$ , namely,  $\psi_{vv}(\Gamma, \Gamma_s) \cdot \Gamma_{ss}$ .

The steepest descent flow, then leads to the following quasilinear PDE

$$\mathbf{V} = [\Gamma_s \cdot \nabla_{vp} \psi(\Gamma, \Gamma_s) - \psi_p(\Gamma, \Gamma_s)]^\perp + [\psi(\Gamma, \Gamma_s) + \psi_{vv}(\Gamma, \Gamma_s)] \Gamma_{ss}. \quad (6)$$

Here  $\psi_{vv}(\Gamma, \mathbf{T})$  is the linear map on  $T_v S^{n-1}$  defined by the second covariant derivative of  $\psi(\Gamma, v)$ . Thus for any pair of vectors  $X, Y \in T_v S^{n-1}$  one has by definition

$$\nabla_{X,Y}^2 \psi(p, v) = (X, \psi_{vv} \cdot Y).$$

One sees that (6) is a parabolic equation exactly when  $\psi$  defines a Finsler metric. This equation defines our model for the *Finsler geodesic active contours*.

The above derivation works for closed curves. In the planar case, one may implement such a flow using level set techniques. We, however, are also interested in direction-dependent flows for curves in which we fix seed and target regions, and for this we will propose (in Section 2.4) the use of dynamic programming. This is essential for diffusion tensor imaging in which we want to discover white matter tracts starting from some point in the image.

Finally, in Appendix B below, we derive the first variation of the Finsler functional in terms of the homogeneous extension  $F$  which leads to another numerical scheme.

## **2.4 Direction-Dependent Dynamic Programming**

In this section, we show how dynamic programming can be used to determine optimal curves. The Finsler metric condition on the anisotropic factor  $\psi$  will be assumed throughout this discussion (so that optimal paths will indeed exist).

### 2.4.1 Optimal control and the principal of optimality

Consider the optimal control problem of determining a trajectory  $x : [0, 1] \rightarrow \mathbf{R}^n$  that is optimal with respect to the functional

$$J(x(\cdot), \mathbf{u}(\cdot)) = \int_0^1 L(x(t), \mathbf{u}(t)) \, dt.$$

We assume in the discussion below that  $L$  is homogeneous of degree 1 in the  $\mathbf{u}$  variable. The control  $\mathbf{u}(\cdot)$  is defined by:

$$\dot{x}(t) = \mathbf{u}(t).$$

For any given starting point  $x_0$ , define the value function as the minimum cost for reaching a seed region  $S \subset \mathbf{R}^n$  from  $x_0$ :

$$J^*(x_0) = \inf_{\mathbf{u}(\cdot), x(0)=x_0, x(1) \in S} J(x(\cdot), \mathbf{u}(\cdot)).$$

When an optimum exists, it may be found using Bellman's *principle of optimality* [22]. Basically, this states that if  $x^*(\cdot)$  is an optimal trajectory, then all subpaths are also optimal. This can be expressed by the following relation:

$$J^*(x_0) = \inf_{\mathbf{u}(\cdot), x(0)=x_0, x(1) \in S} \left\{ \int_0^r L(x(t), \mathbf{u}(t)) \, dt + J^*(x(r)) \right\}.$$

This means that if an optimal trajectory  $x^*(\cdot)$  is found such that  $x^*(0) = x_0$  and  $x^*(1) \in S$ , then for any  $r \in ]0, 1[$  the sub-trajectories  $x^*_{|[0,r]}$  and  $x^*_{|[r,1]}$  are also optimal. See [22] for a detailed proof.

In our case, using  $x_t = \mathbf{u}$  and  $x(0) = x_0$ , the following Hamilton-Jacobi-Bellman equation is obtained:

$$0 = \inf_{\mathbf{u}(0)} \{ L(x_0, \mathbf{u}(0)) + \nabla J^*(x_0) \cdot \mathbf{u}(0) \}. \quad (7)$$

In general the value function may not be differentiable. In that case the differential equation (7) holds in the sense of *viscosity theory*. See [95].

Under our above assumptions, this can be applied to the Finsler cost functional:

$$\begin{aligned}\mathcal{L}(\Gamma) &= \int_0^L \psi(\Gamma(s), \Gamma_s(s)) \, ds \\ &= \int_0^1 F(\Gamma, \Gamma_x/|\Gamma_x|) |\Gamma_x| \, dx = \int_0^1 F(\Gamma, \Gamma_x) \, dx,\end{aligned}\tag{8}$$

where  $s$  is arclength and  $L$  is length of the curve.

The resulting Hamilton-Jacobi-Bellman equation is

$$0 = \inf_{\Gamma_x(0)} \left\{ \psi\left(\Gamma(0), \frac{\Gamma_x(0)}{|\Gamma_x(0)|}\right) |\Gamma_x(0)| + \nabla \mathcal{L}^*(\Gamma(0)) \cdot \Gamma_x(0) \right\},$$

and finally,

$$\begin{cases} 0 = \inf_{\hat{\mathbf{d}} \in \mathbb{S}^{n-1}} \{ \psi(\mathbf{p}, \hat{\mathbf{d}}) + \nabla \mathcal{L}^*(\mathbf{p}) \cdot \hat{\mathbf{d}} \}, \\ \mathcal{L}^*(s) = 0 \text{ for } s \in S, \end{cases}\tag{9}$$

where anticipating our discussion in Section 2.5 for images, we denote the given voxel location (i.e. point in  $\mathbf{R}^n$ ) as  $\mathbf{p}$  and direction as  $\hat{\mathbf{d}}$ .

#### 2.4.2 Numerics

This equation can be solved numerically in a straightforward manner. Several numeric approaches may be used, such as those given in [93, 40, 39]. We use the Fast Sweeping approach proposed in [39]. From any point  $\mathbf{p}_0 \in \mathbf{R}^n$  an optimal path in the sense of (8) can then be determined by following locally the vector  $\hat{\mathbf{d}}^*$  for which the minimum is attained in (9).

---

**Algorithm 1** Sweeping algorithm to solve the Hamilton-Jacobi-Bellman equation (9); see [40]

---

**Require:** seed region  $S$ , direction-dependent local cost  $\psi$

- 1: Initialize  $\mathcal{L}^*(\cdot) \leftarrow +\infty$ , except at starting points  $s \in S$  where  $\mathcal{L}^*(s) \leftarrow 0$
  - 2: **repeat**
  - 3:   **sweep** through all voxels  $\mathbf{p}$ , in all possible grid directions
  - 4:    $\hat{\mathbf{d}}' \leftarrow \arg \min_{\hat{\mathbf{d}} \in \mathbb{S}^{n-1}} f_{\mathcal{L}^*, \psi}(\mathbf{p}, \hat{\mathbf{d}})$
  - 5:   **if**  $f_{\mathcal{L}^*, \psi}(\mathbf{p}, \hat{\mathbf{d}}') < \mathcal{L}^*(\mathbf{p})$  **then**  $\mathcal{L}^*(\mathbf{p}) \leftarrow f_{\mathcal{L}^*, \psi}(\mathbf{p}, \hat{\mathbf{d}}')$  and  $\hat{\mathbf{d}}^*(\mathbf{p}) \leftarrow \hat{\mathbf{d}}'$  **end if**
  - 6:   **end sweep**
  - 7: **until** convergence of  $\mathcal{L}^*$
-

The algorithm sweeps through all points  $\mathbf{p}$  in search of the least expensive direction. The cumulated cost to reach  $\mathbf{p}$  from direction  $\hat{\mathbf{d}}$  is  $f_{\mathcal{L}^*, \psi}(\mathbf{p}, \hat{\mathbf{d}}) \triangleq (\sum_{k=0}^{n-1} \alpha_k \mathcal{L}^*(\mathbf{p} + \boldsymbol{\delta}_k) + \psi(\mathbf{p}, \hat{\mathbf{d}})) / (\sum_{k=0}^{n-1} \alpha_k)$ , where the  $n$  neighbors  $\mathbf{p} + \boldsymbol{\delta}_0, \dots, \mathbf{p} + \boldsymbol{\delta}_{n-1}$  of  $\mathbf{p}$  in direction  $\hat{\mathbf{d}}$  are interpolated using the components of the vector  $\boldsymbol{\alpha} \triangleq [\boldsymbol{\delta}_0 \mid \dots \mid \boldsymbol{\delta}_{n-1}]^{-1} \hat{\mathbf{d}}$ . Thus in three dimensions, this would be  $n = 3$  neighbors among 26. If we take then, for example,  $\hat{\mathbf{d}} = (0.912, 0.228, 0.342)^t$ , one could choose the 3 neighbors  $\boldsymbol{\delta}_0 = (1, 0, 0)^t$ ,  $\boldsymbol{\delta}_1 = (1, 0, 1)^t$ ,  $\boldsymbol{\delta}_2 = (1, 1, 1)^t$ , and the corresponding weights would be  $\boldsymbol{\alpha} = (\alpha_0, \alpha_1, \alpha_2) = (0.228, 0.114, 0.570)$ . One interpretation is that the value for reaching  $\mathbf{p}$  from direction  $\hat{\mathbf{d}}$  will be influenced most by the value at  $\mathbf{p} + \boldsymbol{\delta}_2$ , which is the neighbor as much in direction  $\hat{\mathbf{d}}$  as the grid allows. Since in general it is not exactly in that direction, the final result will also be interpolated using the two other most aligned neighbors  $\mathbf{p} + \boldsymbol{\delta}_0$  and  $\mathbf{p} + \boldsymbol{\delta}_1$ .

One sees that if the continuous direction  $\hat{\mathbf{d}}$  is exactly defined by one of the neighboring voxels, i.e.,  $\hat{\mathbf{d}} = \boldsymbol{\delta}_k / \|\boldsymbol{\delta}_k\|$ , then  $f = \mathcal{L}^*(\mathbf{p} + \boldsymbol{\delta}_k) + \psi(\mathbf{p}, \hat{\mathbf{d}}) \|\boldsymbol{\delta}_k\|$ , which is the cost for reaching voxel  $\mathbf{p}$  from voxel  $\mathbf{p} + \boldsymbol{\delta}_k$ . This same quantity would be computed in Dijkstra's algorithm. Unlike Dijkstra's algorithm however, the search for the optimal direction is not restricted to discrete grid directions, and the minimization is performed continuously over the sphere  $S^{n-1}$ . In our implementation, the minimization is performed over 100 directions sampled uniformly on the sphere<sup>2</sup> and the coefficients  $\boldsymbol{\alpha}(\hat{\mathbf{d}})$  are pre-computed. Mathematical details and a convergence proof are available in [40].

Note that the number of iterations (where one iteration is defined as one set of all possible directional sweeps) required for convergence depends upon the number of turns in the curve. Each iteration, therefore, can flow information through one complete turn of the curve. In the Applications and Simulations of Section 2.5, we found all the curves in 3 iterations or less.

---

<sup>2</sup>For the algorithm to initialize properly, discrete grid directions have to be present.

## 2.5 Applications and Simulations

Having developed the theory behind Finsler active contours, we now illustrate these via several experiments. First, we demonstrate curve shortening with respect to certain anisotropic conformal factors as opposed to isotropic curve shortening. Second, we provide a synthetic example which demonstrates a particular case where Finsler active contours capture a corner in directional data. Third, these methods are applied to a pattern detection problem, specifically to detect roads and vessels in 2D imagery. Fourth, we show 3D results of these techniques applied to diffusion-weighted magnetic resonance imagery for white matter brain tractography.

### 2.5.1 Closed curves evolving according to the Finsler flow

In this section, in order to compare the proposed direction-dependent framework to the isotropic framework, we examine the evolution of a closed bean-shaped curve with respect to three separate conformal factors.

In order to isolate the effect of directional information, we study local costs that do not depend on position but only on the direction  $\mathbf{N} = [n_1 \ n_2]^t$  (we use the unit normal instead of the unit tangent in defining the conformal factors; for planar curves this is clearly equivalent):

1.  $\psi = 1$ ;
2.  $\psi = \max(\frac{1}{\sqrt{2}}|n_1 + n_2|, \frac{1}{\sqrt{2}}|n_2 - n_1|)^3/0.75$ ;
3.  $\psi = \max(|n_1|, |n_2|)^3/0.75$ .

The first cost is isotropic. In that case, the global cost of the curve is its Euclidean length and the minimizing flow is the Euclidean curvature flow [26, 29]. This flow shrinks any planar shape to a circular shaped point. This is illustrated on the first column of Figure 1. The second and third costs are defined using direction information. In particular, the second cost favors portions of the curve that are either

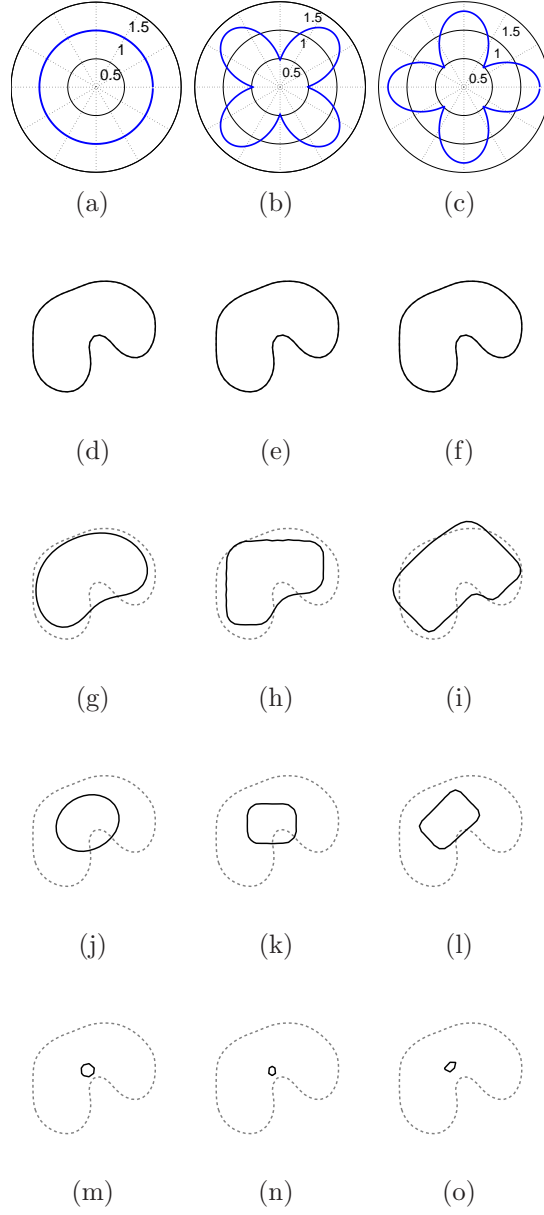


**Figure 1:** Synthetic 2D example. These three different local costs depend only on direction. They are represented as polar plots (first row). The corresponding deforming shapes are presented on the following rows (black). The initial curve (gray dashed) is bean-shaped. See text.

horizontal or vertical. The third costs does exactly the opposite and favors portions of the curve that are diagonal. The corresponding evolutions can be observed on the second and third columns of Figure 1. The influence of direction information is very visible in these figures.

### 2.5.2 Simulated Example

Finsler active contours extend the isotropic geodesic active contours by adding directionality to the distance functional. Therefore, in oriented domains where directionality is important, Finsler active contours capture important directional information unavailable to isotropic geodesic active contours.

Furthermore, Finsler active contours extend Riemannian active contours by minimizing with respect to the more general Finsler metric. It will be shown that, in some cases, minimization with respect to a Riemannian metric will yield a smoothed version of the result obtained via the Finsler metric.

In order to analyze these properties of Finsler active contours, we have devised a synthetic simulation. We constructed a simple 2D (64x64 pixel) image with an 'L' shaped corner as seen in Figure 2(a). The goal of this simulation is to find an open curve which extends from the top yellow marker to the bottom yellow marker and which follows the 'L' shape. We performed this simulation using the dynamic programming numerical scheme. The yellow markers are given as known inputs to the algorithm.

The synthetic directional data was created by randomly drawing samples from the uniform distribution on the interval  $[0,0.5]$  for evenly spaced directions on the unit circle. Then, we added the signal by giving directions of high diffusion slightly stronger values, as shown in Figure 2(c). This figure shows a zoomed-in view of the directional image for 9 pixels surrounding the corner. The red arrows correspond to the high diffusion directions (i.e. the signal), the green arrows correspond to a

diffusion process contrary to the signal flow, and the blue arrows are the randomly drawn background samples.

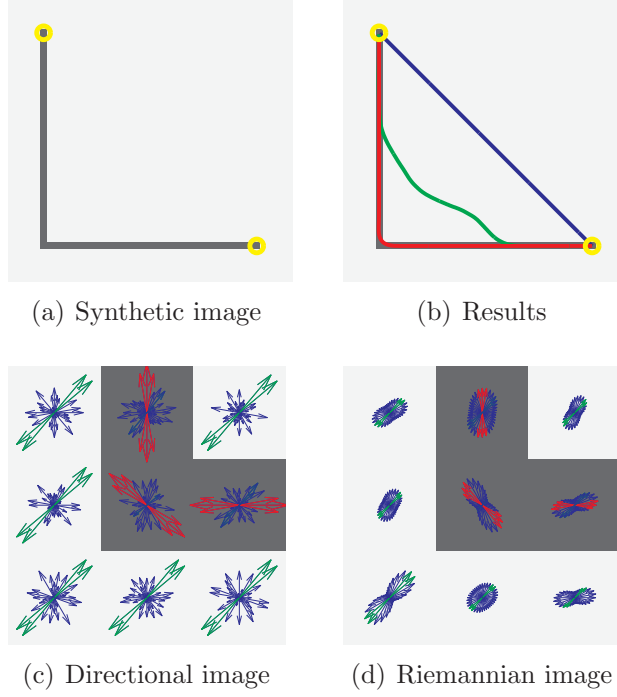


**Figure 2:** Simulated 2D example: (a) The synthetic baseline 'L' shaped corner, (b) Finsler results (red), Riemannian results (green), Isotropic results (blue), (c) A zoomed-in view showing the directional data of 9 pixels surrounding the corner, (d) A zoomed-in view showing the Riemannian image of 9 pixels surrounding the corner, created by applying the Stejskal-Tanner equation to the directional data

Using the Finsler active contour framework, we are able to capture the 'L' shaped corner accurately, as pictured in red in Figure 2(b). We will now compare this to two other methods.

First, we show that adding directional information is critical to capturing the corner. We proceed by comparing the Finsler active contour approach to the isotropic geodesic active contour approach implemented using the Fast Marching Method [73, 92]. At each point in the image, the strongest diffusion value (without respect for directionality) was chosen as the scalar to be used in the isotropic approach. Since, by construction, the strongest diffusion value at each point is the same (i.e. the

magnitude of red arrows is the same as the magnitude of green arrows), it is obvious that the optimal path for the isotropic geodesic active contour is a straight line connecting the yellow markers, as shown by the blue line in Figure 2(b). This example illustrates the need for directionality and the difficulties which arise from attempting to discard the directionality via a pointwise scalar function (in this case the maximum diffusion at each point).

Second, we compared the Finsler active contour approach to the Riemannian active contour approach. In this simulation, we created tensors from the directional data using the Stejskal-Tanner equation, as shown by the zoomed-in view of the corner in Figure 2(d). This figure shows a zoomed-in view of the Riemannian image for 9 pixels surrounding the corner. The resulting Riemannian optimal path is shown in green in Figure 2(b). This figure reveals the smoothing effect which the Riemannian metric tends to have on the result. This is due to the directional averaging which occurs in the construction of the tensors by imposing the elliptical diffusion profile on the data.

These simulations reveal that, for this particular case, the Finsler active contour is desirable due to the fact that it is capable of capturing a sharp corner in an oriented domain. In other cases, the scalar geodesic active contour or Riemannian active contour approaches may have attributes which render them more suited to the particular task.

### 2.5.3 Curve Detection in Imagery

Given a sample image  $I$  for which a portion of a curve  $\Gamma^*$  is given (for example, by a human expert), imagine sliding a small rectangular window along the curve in such a way that the center of the window is always on the curve and the long axis of the window is aligned with the tangent to the curve. Computing the average value of image intensities at each point inside the window as the window slides along the

curve, one obtains an average pattern of what the image looks like locally around the curve  $\Gamma^*$ . A location and direction-dependent pattern detector can then be defined by translating and rotating the average pattern and determining how well it matches the image.

This protocol was applied to a road detection task. Figure 3 shows the portion of the road that was used to learn the pattern detector. The dimension of the window along its long axis (i.e., in the direction of the road) was chosen to be four times the width of the road, and the dimension of the window along its short axis (i.e., normal to the road) was chosen to be two times the width of the road. The pattern detector was then obtained for any position and direction by translating and rotating the average window and computing the sum of the square of the difference between the intensity of the image and that of the average window. Curves that will be minimal for this metric will then be those for which the image locally matches the pattern of a road.

Curves were deformed using a straightforward particle-based approach. Figures 4 show two different initial curves converging to the same portion of the road. Figure 4 show the evolution of a self-intersecting initial curve. Finally, Figure 5 illustrates the use of dynamic programming. Note that for very low SNR, the dynamic programming fails.

The same experiments were performed on a medical image to track blood vessels. As before the metric was defined by an initial manual segmentation step. Figure 6 shows the result of the curve evolution approach. Figure 7 shows the result of the dynamic programming approach. In that case noise was artificially added.

#### **2.5.4 High angular diffusion MRI tractography**

Diffusion Tensor Magnetic Resonance Imaging (DT-MRI) measures the diffusion of water in biological tissue [5]. The utility of this method stems from the fact that



**Figure 3:** Road image and manually determined curve used for learning the pattern detector.

tissue structure locally affects the Brownian motion of water molecules and will be reflected in the DT-MRI diffusion measurements. In classical theory, diffusion follows a Gaussian process which can be described locally by a second order tensor.

A simple and effective method for tracking nerve fibers using DT-MRI is to follow the direction of maximum diffusion at each voxel [64, 16, 113, 6]. Although this method is wide-spread and used in various ways the fiber trajectory is based solely on local information which makes it very sensitive to noise. Moreover the major direction of diffusion can become ill-defined for example at fiber crossings.

As an application of our framework, tractography is set in a continuous minimum cost framework. This is different from [30, 13]. Indeed in these works, the authors do not propose variational (cost minimizing) techniques. Local costs are defined for every direction on the unit sphere based on high angular resolution diffusion imagery. Equivalently, this can be considered a minimum arrival time framework in which the speed of fictitious particles would be the inverse of the cost.

#### 2.5.4.1 Constructing the Direction-Dependent Cost

Most front propagation techniques for diffusion tensor tractography use some *ad hoc* function  $f$  of the quadratic form  $\hat{\mathbf{d}}^t D \hat{\mathbf{d}}$ , where  $D$  is the diffusion tensor. If the Gaussian

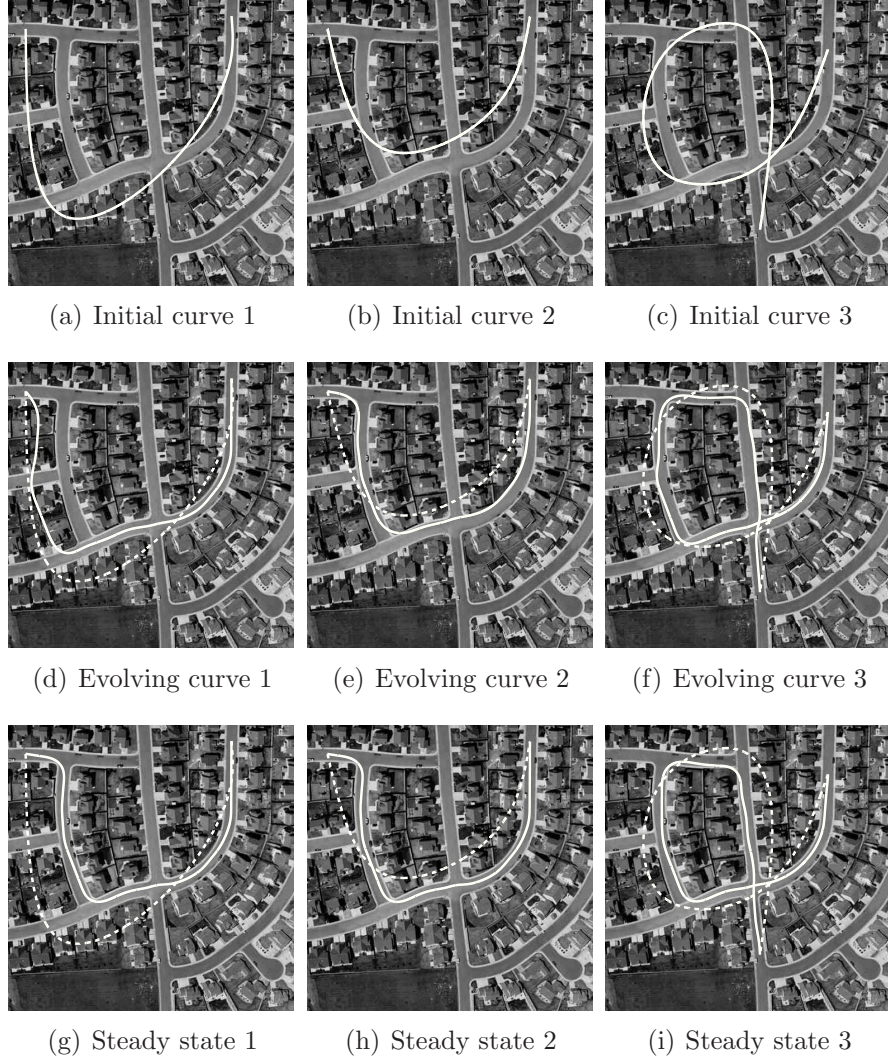


**Figure 4:** Particle-based Curve Evolution with Different Initializations

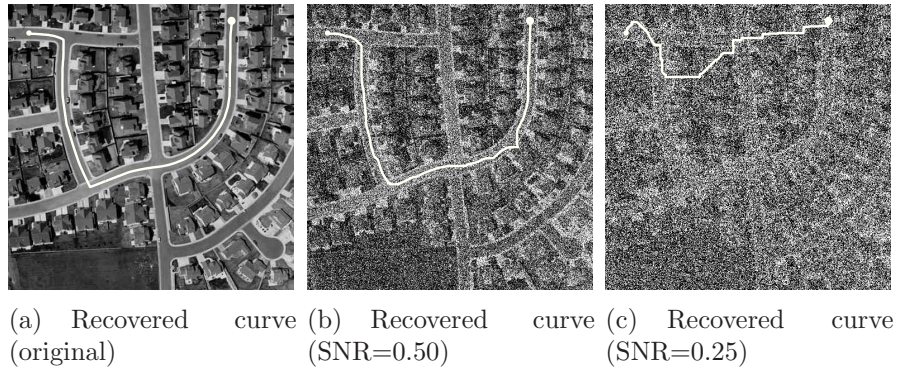


**Figure 5:** Results of road detection on noisy images using dynamic programming.

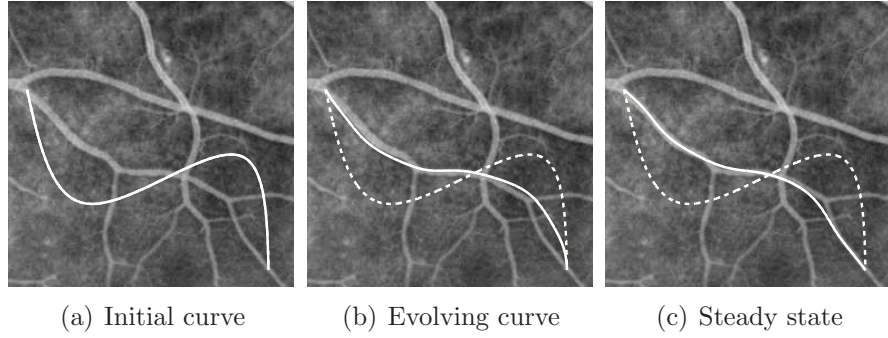


**Figure 6:** Curve evolution on a real image. The local cost is determined using a pattern detector.

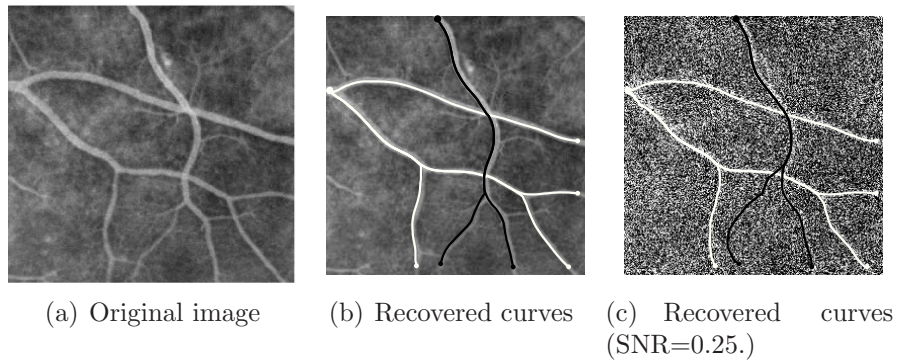


**Figure 7:** Vessel detection using dynamic programming. The procedure was run independently for two seed points (large discs) and several target points (small discs). On the right, noise was added. This changes the recovered curves as one of the branches at the bottom is no longer visible.

assumption holds, the diffusion weighted images follow

$$S(\mathbf{p}, \hat{\mathbf{d}}) \simeq S(\mathbf{p}, \mathbf{0}) \exp(-b \hat{\mathbf{d}}^t D(\mathbf{p}) \hat{\mathbf{d}}). \quad (10)$$

Tensor based techniques can formally be extended to high angular resolution diffusion datasets by setting (see [82] and references therein for details):

$$\psi(\mathbf{p}, \hat{\mathbf{d}}) \triangleq f\left(-\frac{1}{b} \log\left(\frac{S(\mathbf{p}, \hat{\mathbf{d}})}{S(\mathbf{p}, \mathbf{0})}\right)\right). \quad (11)$$

However, in the experiments below we employed the following metric:

$$\psi(\mathbf{p}, \hat{\mathbf{d}}) \triangleq \left( \frac{S(\mathbf{p}, \hat{\mathbf{d}})}{\int_{\hat{\mathbf{v}} \perp \hat{\mathbf{d}}} \frac{S(\mathbf{p}, \hat{\mathbf{v}})}{S(\mathbf{p}, \mathbf{0})} d\hat{\mathbf{v}}} \right)^3. \quad (12)$$

This quantity will be small if there is diffusion in direction  $\hat{\mathbf{d}}$  (numerator small) and limited diffusion in directions normal to  $\hat{\mathbf{d}}$  (denominator large). The main advantage of this formulation is that several data points are used to compute the denominator which improves the signal to noise ratio. We chose  $f(x) = x^3$  experimentally to accentuate the anisotropy of the data. Because experimentally only a few dozen directions are used for acquisition, interpolation was also performed.

It is very important to note that the anisotropic conformal factor  $\psi$  is constructed from the data, and for example in the DW-MRI case we have no proof that the corresponding  $F^2$  is always strictly convex. However, in Appendix A below we include for completeness a standard argument which shows that using a scheme such as fast-sweeping, one computes the optimum relative to the convexification of  $F^2$ . This type of convexification argument is well-known in the optimal control literature (see the classical text [117] for details). Thus we are computing in fact geodesic active contours relative to the Finsler metric defined by the convexification of the defining function.

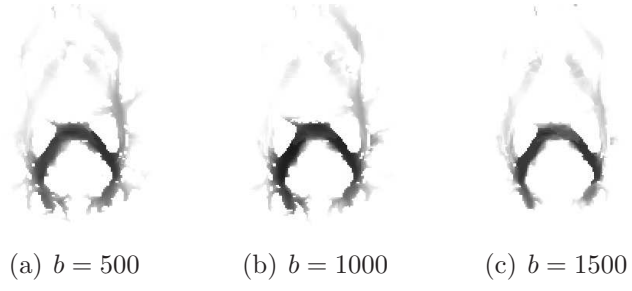


**Figure 8:** Cost per unit length of end points of optimal curves for different  $b$ -values is a validity index. Best results are achieved for the highest  $b$ -value.

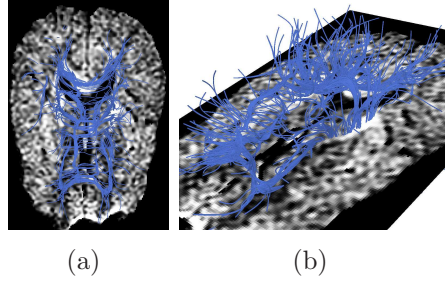


**Figure 9:** Fiber tracking from high angular resolution dataset ( $b=1500 \text{ s/mm}^2$ ).

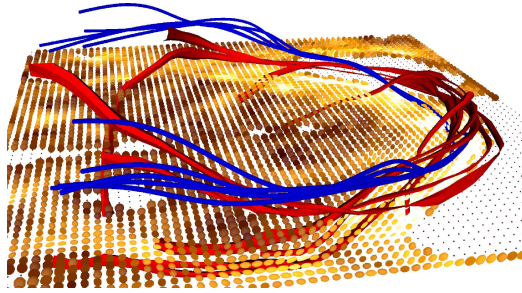


**Figure 10:** Proposed technique on high angular resolution data (blue) compared with streamline technique on tensor field (red) ( $b=1500 \text{ s/mm}^2$ ).

#### 2.5.4.2 Results

Here we show results obtained by applying the methodology described in the above sections to diffusion weighted data sets acquired using a single-shot diffusion-weighted EPI sequence, with 31 different gradient directions with b-values (see equation (10)) of 500, 1000, and  $1500s/mm^2$ , on a 1.5 Tesla GE Echospeed system. The data was acquired with different b-values to enable comparisons of the results. Traditional eigenvector based tractography is normally carried out in data with b-values in the range of  $700 - 1000s/mm^2$ . Higher b-values give data with higher angular contrast, but at the expense of more noise.

Cost per unit length, which can be interpreted as a validity index for the putative tracts was determined for all b-values as shown in Figure 8.

All curves are optimal given their starting point. The cost per unit length is a measure of the likelihood that a tract from the seed region passes through a given point in the domain. The best contrast (corresponding to the most coherent set of “super-optimal” tracts for a given seed point posterior of the corpus callosum) was obtained at the highest b-value available. This could indicate that the algorithm was able to take advantage of the higher angular contrast in spite of the lower SNR. Tract results for several user defined seed points are presented in Figure 9.

Finally, the proposed technique was compared to a streamline technique (see [64, 16, 113, 6]) which requires the computed tensor field as shown in Figure 10.

While validation is a very challenging task due to the lack of ground truth, it can be noted that both algorithms give similar results even though their inputs are different. The tracts of the proposed technique tend to be more coherent as any noise in the data might set the streamline off course whereas the proposed technique is more global.

### 2.5.5 A Note on Timings

Here we present a note on the timings for each of the experiments. All of the experiments were performed on a common PC. We used a Dell Optiplex GX270 with an Intel Pentium 4 single core chip and 2GB of memory. Each of the experiments above was conducted using Matlab code with C mex functions for the Fast Sweeping implementation. And, while this code was sufficiently fast for our purposes, we are in the process of porting the code to the freely available Insight Toolkit (ITK) [33].

All of the particle based approaches, on 2D roads and vessels, converged quickly and in negligible time. Also, all of the Fast Sweeping approaches converged in 3 iterations or less (where one iteration consists of all of the possible directional sweeps through the image), see 2.4.2 for more discussion on Fast Sweeping convergence. For example, it took 0.13 seconds for the experiment in Section 2.5.2 to converge on a 64x64 grid, and it took 20 seconds for the experiment in Section 2.5.3 to converge on a 787x787 grid. Also, with simple masking of irrelevant voxels, the time to converge for the 3D DWMRI experiment in Section 2.5.4 was under 5 minutes. The time to compute a path from a target point back to the seed point is negligible compared to the time required to run the Fast Sweeping portion of the algorithm.

## 2.6 Conclusions

In this chapter, we proposed a natural approach for adding directionality to the conformal active contour technique. The cost of a curve is defined as the length of the curve weighted by some position and direction-dependent local costs based on image information. This allows for the asymmetric processing of information based on direction. The local costs can be defined from a direction-dependent pattern detector, which can be obtained after a learning step.

The techniques described in the chapter are very general and could be used to extract information from many different types of imagery. They have been applied

mostly to medical imaging datasets and, in particular, to images of the brain. In fact, it was the problem of extracting white matter tracts that initially motivated this line of research. In the medical area, it could be also be applied to the extraction of blood vessels from various imaging modalities such as magnetic resonance or computed tomography.

Finally, we have only described the Finsler framework in the case of curves. One can derive and study a similar flow for surfaces. This will be the topic of our future research in studying directional-based segmentation methods.

## CHAPTER III

### FINSLER TRACTOGRAPHY

In this chapter, we present a novel approach for the segmentation of white matter tracts based on Finsler active contours [57]. This technique provides an optimal measure of connectivity, explicitly segments the connecting fiber bundle, and is equipped with a metric which is able to utilize the directional information of high angular resolution data. We demonstrate the effectiveness of the algorithm for segmenting the cingulum bundle.

#### *3.1 Introduction*

Since the advent of diffusion weighted magnetic resonance imaging (DW-MRI), a great amount of research has been devoted to finding and characterizing neural connections between brain structures. Image resolution is typically high enough that white matter tracts, or bundles of densely packed axons, pass through several voxels [65]. In this chapter, we present a novel approach for the segmentation of white matter tracts based on Finsler active contours [59]. Furthermore, we show results of the algorithm for segmenting the cingulum bundle (CB) <sup>1</sup>.

Early tractography methods were based on streamlines which employed local decision-making based on the principal eigenvector of diffusion tensors [64, 99, 6, 16]. Recently, tractography advances have been made which provide full brain optimal connectivity maps from predefined seed regions. These methods are more robust to noise and depending upon the underlying metric, may be able to more fully use the complete DW-MRI data. These approaches can be subdivided into stochastic and

---

<sup>1</sup>Data provided by the Brigham and Women's Hospital, Psychiatry Neuroimaging Laboratory, Boston, MA

energy-minimization approaches.

In these techniques, tracts are propagated from a starting point until the tracts reach some termination criterion. Due to the local decision-making process, these methods have been shown to perform poorly in noise and often stop prematurely, as we depict later in Fig. 11(b) for the case of the cingulum bundle. These techniques do not provide a measure of connectivity for the resulting tracts. Furthermore, several of these methods do not use the full tensor, reducing the data to the principal eigenvectors, and subsequently are unable to handle fiber crossings, branchings, “kissings”, etc.

Stochastic approaches produce probability maps of connectivity between a seed region and the rest of the brain. Parker *et al.* developed PICO, a probabilistic index for standard streamline techniques [76]. Perrin *et al.* presented probabilistic techniques for untangling fiber crossings using q-ball fields [78]. In other work, Friman *et al.* proposed a method for probabilistically growing fibers in a large number of random directions and inferring connectivity from the resulting percentages of connections between seed and target regions [24]. While providing a measure of connectivity between brain regions, these stochastic approaches do not provide an explicit segmentation of the fiber bundle itself.

Energy-minimization techniques have also been developed. Parker *et al.* proposed fast marching tractography which minimizes an energy based on both the position and direction of the normal to a propagating front [77]. O'Donnell *et al.* cast the tractography problem in a geometric framework finding geodesics on a Riemannian manifold based on diffusion tensors [74]. Similarly, Prados *et al.* and Lenglet *et al.* demonstrated a Riemannian based technique, GCM (Geodesic Connectivity Mapping), for computing geodesics using a variant of fast marching methods adapted for directional flows [85, 51]. Jackowski *et al.* also find Riemannian geodesics using Fast Sweeping methods as given by Kao *et al.* [34, 39, 40]. In cases of high angular

diffusion data, these Riemannian based approaches do not take advantage of the full directional resolution due to the loss of information incurred by the construction of diffusion tensors.

In this chapter, we present a technique which provides an optimal measure of connectivity, explicitly segments the connecting fiber bundle, and is based on the richer Finsler metric. Rather than following the traditional approach of finding a large number of fibers (which individually have questionable meaning), clustering them, and then performing statistical analyses on the clusters, we present an alternative approach. We first find the optimal connection, which we term the *anchor tract*, on the Finsler manifold between the seed and target regions. Then, we initialize an expanding surface level set evolution on the anchor tract which grows until it stops at a local minima on the edge of the fiber bundle. Finally, since the fiber bundle extraction does not rely upon standard statistical measures, such as fractional anisotropy (FA), for the segmentation, we are free to use these measures to statistically compare fiber bundles in clinical studies.

In Section 3.2, we motivate our interest in segmenting the cingulum bundle. In Section 3.3, we describe the algorithm for extracting the anchor tracts. Then, in Section 3.4, we present our surface evolution algorithm for extracting the full cingulum bundle. Finally, in Section 3.5, we show results for extracting the anchor tracts and the corresponding cingulum bundle.

### ***3.2 The Cingulum Bundle***

The cingulum bundle is a 5-7 mm in diameter fiber bundle that interconnects all parts of the limbic system. It originates within the white matter of the temporal pole, and runs posterior and superior into the parietal lobe, then turns, forming a "ring-like belt" around the corpus callosum, into the frontal lobe, terminating anterior and inferior to the genu of the corpus callosum in the orbital-frontal cortex [90].

Moreover, the cingulum bundle consists of long, association fibers that directly connect temporal and frontal lobes, as well as shorter fibers radiating into their own gyri. The cingulum bundle also includes most afferent and efferent cortical connections of cingulate cortex, including those of prefrontal, parietal and temporal areas, and the thalamostriate bundle. In addition, lesion studies document a variety of neurobehavioral deficits resulting from a lesion located in this area, including akinetic mutism, apathy, transient motor aphasia, emotional disturbances, attentional deficits, motor activation, and memory deficits. Because of its involvement in executive control and emotional processing, the cingulum bundle has been investigated in several clinical populations, including depression and schizophrenia. Previous studies, using DW-MRI, in schizophrenia, demonstrated decrease of FA in anterior part of the cingulum bundle [47, 112], at the same time pointing to the technical limitations restricting these investigations from following the entire fiber tract.

### ***3.3 Anchor Tracts on a Finsler Manifold***

In this section, we present our algorithm for extracting the optimal path, or *anchor tract*, between two regions in the brain. In this formulation, the optimal path is defined with respect to a Finsler metric. In the case of data acquired with only 6 gradient directions, this reduces to a Riemannian metric because there are 6 independent elements of the diffusion tensor. However, in the case of high angular data, the Finsler metric is more flexible than the Riemannian metric as it is not restricted to an ellipsoidal diffusion profile which results from the Gaussian diffusion assumption.

In order to find the anchor tract, we construct a dynamic programming based approach which uses a Fast Sweeping method, see [82, 39, 40] for algorithmic details. Also, see the work by Jackowski *et al.* for a formulation of this algorithm based on the Riemannian metric [34]. For the sake of completeness, we include a brief overview of the algorithm.

For any given starting point  $\mathbf{p}_0$ , define the value function as the minimum cost for reaching a seed region  $S \subset \mathbf{R}^n$  from  $\mathbf{p}_0$ . The resulting Hamilton-Jacobi-Bellman equation is

$$\begin{cases} 0 = \inf_{\hat{\mathbf{d}} \in S^{n-1}} \{ \psi(\mathbf{p}, \hat{\mathbf{d}}) + \nabla \mathcal{L}^*(\mathbf{p}) \cdot \hat{\mathbf{d}} \}, \\ \mathcal{L}^*(\mathbf{s}) = 0 \text{ for } \mathbf{s} \in S, \end{cases} \quad (13)$$

where  $\psi$  is the local cost at each point,  $\mathbf{p}$ , and for each direction,  $\hat{\mathbf{d}}$ , and  $\mathcal{L}^*$  is the optimal Finsler length. Numerically, this equation may be solved via Fast Sweeping as shown in Algorithm 2.

---

**Algorithm 2** Sweeping algorithm for the HJB equation (13)

---

**Require:** seed region  $S$ , direction-dependent local cost  $\psi$

- 1: Initialize  $\mathcal{L}^*(\cdot) \leftarrow +\infty$ , except at starting points  $s \in S$  where  $\mathcal{L}^*(s) \leftarrow 0$
  - 2: **repeat**
  - 3:   **sweep** through all voxels  $\mathbf{p}$ , in all possible grid directions
  - 4:     $\hat{\mathbf{d}}' \leftarrow \arg \min_{\hat{\mathbf{d}} \in S^{n-1}} f_{\mathcal{L}^*, \psi}(\mathbf{p}, \hat{\mathbf{d}})$
  - 5:    **if**  $f_{\mathcal{L}^*, \psi}(\mathbf{p}, \hat{\mathbf{d}}') < \mathcal{L}^*(\mathbf{p})$  **then**  $\mathcal{L}^*(\mathbf{p}) \leftarrow f_{\mathcal{L}^*, \psi}(\mathbf{p}, \hat{\mathbf{d}}')$  and  $\hat{\mathbf{d}}^*(\mathbf{p}) \leftarrow \hat{\mathbf{d}}'$  **end if**
  - 6:   **end sweep**
  - 7: **until** convergence of  $\mathcal{L}^*$
- 

The Fast Sweeping algorithm results in optimal connectivity maps and characteristic vectors at every point in the domain. The anchor tract is then determined by following the characteristic vectors from the target region back to the seed region, not by gradient descent as is standard in direction-independent schemes [52].

There are many numerical schemes which may be used to solve the Hamilton-Jacobi-Bellman equation given above. The number of sweeping iterations required by the Fast Sweeping algorithm depends upon the number of turns in the optimal path. Since neural tracts tend to have few total turns, the Fast Sweeping algorithm is efficient for extracting tracts. We also note that the connections of graph cuts and such directional metrics have been described in [12, 46, 11]. Of particular note, in [46] the explicit connection between Finsler distances and the flux methods of [110] is considered in some detail.

### 3.4 Level Set Fiber Bundle Segmentation

In this section, we discuss the level set surface evolution which we have used to extract the volumetric cingulum bundle. This level set surface is initialized on the anchor tract described in Section 3.3. By using the calculus of variations, the minimizing flow for a directional cost  $\psi(\mathbf{p}, \hat{\mathbf{d}})$  is obtained as,

$$\Sigma_t = -\{\nabla_{\mathbf{p}}\psi \cdot N + Tr(\nabla_{\hat{\mathbf{d}}\hat{\mathbf{d}}}\psi) + (n-1)\psi H\}N, \quad (14)$$

where  $\Sigma$  is the evolving hypersurface,  $N$  is the unit normal to the hypersurface, and  $H$  denotes the mean curvature. A derivation of this flow can be found in [79]. The expression for the evolution of the level set function 'u' is obtained as,

$$u_t = \{\nabla_{\mathbf{p}}\psi \cdot \nabla u\} + \{Tr(\nabla_{\hat{\mathbf{d}}\hat{\mathbf{d}}}\psi) + (n-1)\psi H\} \|\nabla u\|. \quad (15)$$

We use the sparse field method of Whitaker *et al.* to efficiently implement this level set surface evolution [114]. We also use the angular interpolation algorithm presented by Tao *et al.* [103].

In order to find the edge of the cingulum bundle, we construct a cost,  $\psi$ , which aligns the tangent plane of the hypersurface with edges in the directions of diffusion of the image volume. To produce a measure of these diffusion edges, we compute the positional gradient of each diffusion direction. We then construct  $\psi$  as a function of these positional gradients.

Mathematically the form of the cost function that we desire to extremize can be written as follows.

$$\psi(\mathbf{p}, \hat{\mathbf{d}}) = \psi(\mathbf{p}, N(\mathbf{p})) = f(\nabla_{\mathbf{p}}\phi(\mathbf{p}, d_1) \cdot N, \nabla_{\mathbf{p}}\phi(\mathbf{p}, d_2) \cdot N \cdots \nabla_{\mathbf{p}}\phi(\mathbf{p}, \hat{\mathbf{d}}_{n_s}) \cdot N) \quad (16)$$

where  $d_1$  through  $d_{n_s}$  denote the  $n_s$  diffusion directions,  $\phi$  denotes the DWI data,  $N(\mathbf{p})$  denotes the normal to the hypersurface at position  $\mathbf{p}$ , and  $f$  is a linear function of the arguments.

There are many possible choices for the function  $\psi$ . In this chapter, we choose  $\psi$  to be the following:

$$\psi = \left\{ \frac{1}{n_s} \cdot \sum_{i=0}^{n_s} \frac{\nabla_{\mathbf{p}} \phi(\mathbf{p}, d_i) \cdot N(\mathbf{p})}{\| \nabla_{\mathbf{p}} \psi(\mathbf{p}, d_i) \|} \right\} - 1. \quad (17)$$

This cost ranges from  $[-1, 0]$  and is maximized (at 0) when the normal to the hypersphere is aligned with the mean gradient direction.

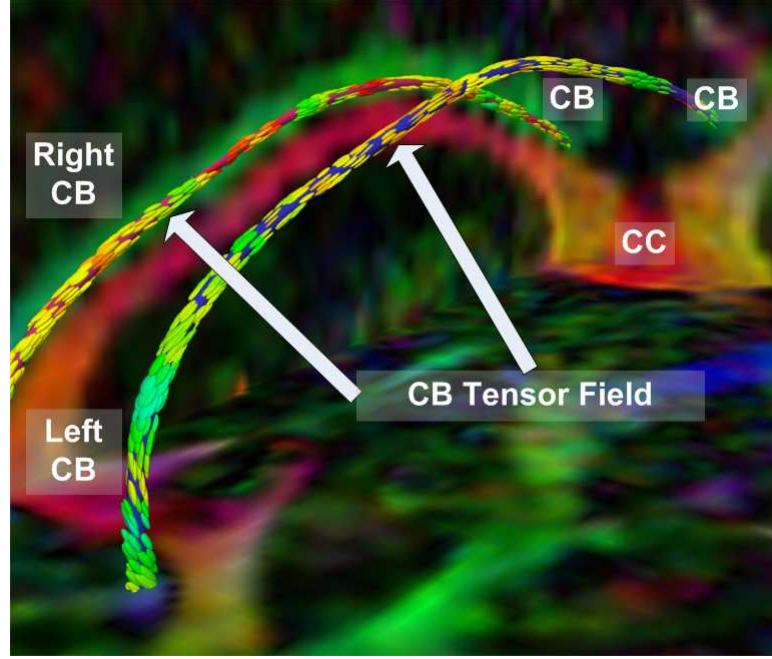
### 3.5 *Experiments & Results*

In this section, we present segmentation results for anchor tracts of the right and left cingulum bundles of 12 schizophrenic and 12 normal patients. Further, we present a first implementation of the level set surface flow introduced in Section 3.4. Scans were acquired on a 3 Tesla GE system (General Electric Medical Systems, Milwaukee, WI). We acquired 51 directions with  $b = 700 \frac{s}{mm^2}$ , 8 baseline scans with  $b = 0 \frac{s}{mm^2}$ . The following scan parameters were used: TR 17000 ms, TE 78 ms, FOV 24 cm, 144 x 144 encoding steps, 1.7 mm slice thickness. We acquired 81 axial-oblique slices parallel to the AC-PC line covering the whole brain.

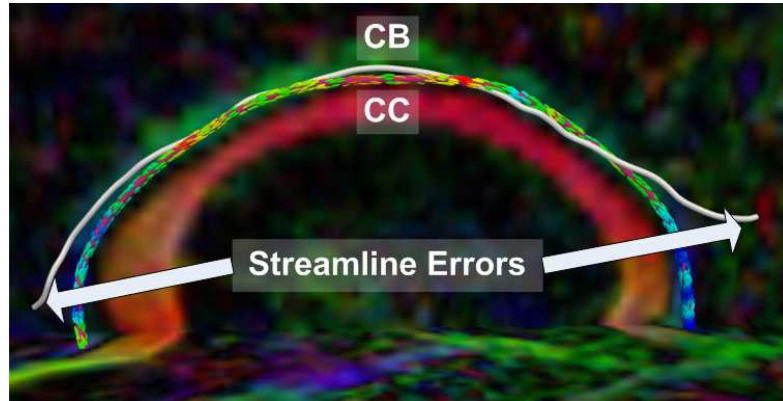
Manually selected endpoints were provided by experts for each case. Masking is necessary to ensure that the tract does not take shortcuts through cerebral spinal fluid (CSF). We used a simple thresholding on the trace of the tensors to mask out CSF regions. Furthermore, we applied a threshold on strong left-right diffusion to mask out the corpus callosum which runs inferior to the cingulum bundle.

First, we show results of extracting the cingulum bundle anchor tract. In each figure, the tracts are superimposed upon the diffusion data which has been colored by direction (e.g. green signifies high anterior-posterior diffusion). The tensors, shown for convenience, are colored by FA. In Fig. 11, we depict the advantage of this algorithm in segmenting the cingulum bundle. The cingulum bundle curves around the ventricles on both the anterior and posterior ends. In Fig. 11(a), we show how the anchor tracts follow the smoothly varying tensor field around the bend of the

ventricles. In Fig. 11(b), we share an example of a streamline based approach (freely available in the 3D Slicer tool) which fails in the same bend around the ventricles. This is the area where large tracts are joining the main bundle from both medial and lateral parts of the parietal lobes. Using the full directional data, our method is able to resolve the cingulum bundle in the presence of the merging fibers. In Fig. 12, we show anterior and posterior zoomed-out views of the anchor tracts.



(a)



(b)

**Figure 11:** Cingulum Bundle Anchor Tracts from: (a) detailed view of a normal control case, (b) streamline example on a schizophrenic case.

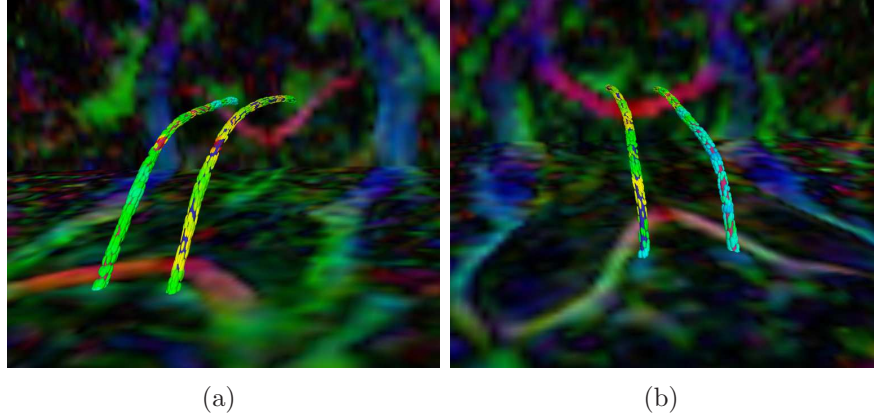


**Figure 12:** Cingulum Bundle Anchor Tracts: (a) anterior and (b) posterior views of a normal control case.

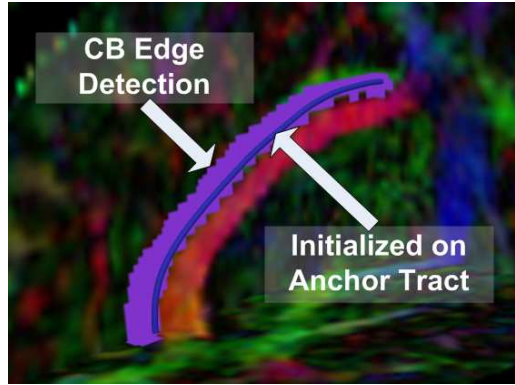


**Figure 13:** Cingulum bundle level set segmentation result on a schizophrenic case.

Next, we show the result of an edge-based surface level set evolution on a portion of the cingulum bundle. We present here a proof of concept implementation of the theory from Section 3.4. In our experiment, the level set flow converged to the edge of the bundle as depicted in the image.

### ***3.6 Conclusions & Future Work***

In this work, we have introduced a novel approach for the segmentation of white matter tracts. We have shown an application of the method for the segmentation of the cingulum bundle. Given manually selected endpoints, the algorithm automatically extracts the cingulum bundle.

We have shown how the method was able to find centerlines, or *anchor tracts* of the cingulum bundle on 24 cases. We have also shown a first implementation of the edge-based level set surface extraction. In the future, we will run the edge-based level set segmentation on all 24 cases. We will also explore the use of other cost functions, especially region-based costs, for the level set segmentation. Finally, we will be able to compute statistics across the resulting segmented cingulum bundles for the population of schizophrenics and normal controls.

## CHAPTER IV

### DW-MRI VOLUMETRIC SEGMENTATION

In this chapter, we present an approach for the volumetric segmentation of neural fiber bundles from DW-MRI data [58]. Through a local constraining of standard region-based segmentation methods, a key problem of defining characteristic statistics on curving fiber bundles is avoided.

#### *4.1 Introduction*

Region-based approaches to image segmentation constitute a key methodology for numerous applications. In these approaches, the objective is to find the segmentation which optimally separates features exterior to a closed curve or surface from features contained in the interior. These approaches have been shown to accurately segment datasets with low signal to noise ratio, frequently outperforming edge-based techniques.

For example, in the work by Chan and Vese, a flow is proposed which optimally separates the first moments of the intensity distributions [15]. In more recent work, Rathi *et al.* demonstrate a method based on the Bhattacharyya distance for separating entire distributions [87]. In both of these cases, features from the entire interior of the curve are compared against features from the entire exterior.

In this present work, we propose a region-based algorithm for the segmentation of neural fiber bundles from diffusion weighted magnetic resonance imagery (DW-MRI). Specifically, we describe why classical approaches (i.e. those which compare features across the full interior with features from the full exterior) may not be well-suited for DW-MRI fiber bundle segmentation. Then, we explain how one can leverage the results of optimal or geodesic path algorithms to locally constrain region-based

approaches in such a manner which will both retain the beneficial attributes of region-based methods while also handling the challenges posed by DW-MRI data. Starting from an optimal path (or anchor tract), a fiber bundle is segmented using a Bayesian framework. The priors are based on anatomical knowledge of the bundle being segmented, for instance, a simple nonlinear anatomically derived function of the distance to the anchor tract works well for the cingulum bundle. The likelihoods are based on local measures of tensor compatibility (local uniformity), adapting a Chan and Vese approach to active contours without edges. The Bayesian formulation is cast as an energy minimization problem which is solved using a greedy flood fill motivated algorithm.

We now briefly describe the remainder of this chapter. First, in Section 4.2, we provide a literature review and background of tractography and fiber bundle segmentation algorithms. Second, in Section 4.3, we motivate our interest in applying this algorithm to the segmentation of the cingulum bundle. Third, in Section 4.4, we describe the algorithm for locally constraining the region-based method. Fourth, in Section 4.5, we provide initial results on the segmentation of the cingulum bundle using a simplistic implementation. Finally, in Section 4.7, we provide an extensive explanation of how these ideas and results may be adapted for use in a variety of implementations and algorithms.

## ***4.2 Background***

Since the advent of diffusion weighted magnetic resonance imaging, a great deal of research has been devoted to finding and characterizing neural connections between brain structures. Image resolution is typically high enough so that major white matter tracts, or bundles of densely packed axons, are several voxels in cross-sectional diameter [65]. The goal of tractography algorithms is to segment these fiber bundles from the DW-MRI datasets.

Early tractography methods were based on streamlines which employed local decision-making based on the principal eigenvector of diffusion tensors [64, 99, 6, 16]<sup>1</sup>.

In these techniques, tracts are propagated from a starting point until the tracts reach some termination criterion. Due to the local decision-making process, these methods have been shown to perform poorly in noise and often stop prematurely. These techniques do not provide a measure of connectivity for the resulting tracts. Furthermore, several of these methods do not use the full tensor, reducing the data to the principal eigenvectors, and subsequently are unable to handle fiber crossings, branchings, “kissings,” etc.

Despite the shortcomings of this approach, due to its ease-of-use, streamlining has quickly become the most popular method for fiber segmentation. To infer fiber bundles from streamline tractography results, several groups have successfully worked on methods for fiber *clustering*. The goal of clustering is to capture group behavior of a population of streamlines and to use this group behavior to drive fiber bundle segmentation. The end result of clustering algorithms has been shown to accurately capture many neural fiber bundles, see for example [71, 62].

Recently, another line of work has emerged which seeks to avoid the use of the problematic streamlines. Tractography advances have been made which provide full brain optimal connectivity maps from predefined seed regions. These methods are more robust to noise and depending upon the underlying metric, may be able to more fully use the complete DW-MRI data. These approaches can be subdivided into stochastic and energy-minimization approaches.

Stochastic approaches produce probability maps of connectivity between a seed region and the rest of the brain. Parker *et al.* developed PICO, a probabilistic index for

---

<sup>1</sup>The diffusion tensor is one of the simplest diffusion models. It is estimated from a set of diffusion weighted images, each probing the water diffusion in a different spatial direction. In the three-dimensional case the diffusion tensor is a  $3 \times 3$  symmetric, positive definite tensor. For details see [7].

standard streamline techniques [76]. Perrin *et al.* presented probabilistic techniques for untangling fiber crossings using q-ball fields [78]. In other work, Friman *et al.* proposed a method for probabilistically growing fibers in a large number of random directions and inferring connectivity from the resulting percentages of connections between seed and target regions [24]. While providing a measure of connectivity between brain regions, these stochastic approaches do not provide an explicit segmentation of the fiber bundle itself and often do not explicitly provide the optimal connection between regions of the brain.

Energy-minimization techniques have also been developed. Parker *et al.* proposed fast marching tractography which minimizes an energy based on both the position and direction of the normal to a propagating front [77]. O'Donnell *et al.* cast the tractography problem in a geometric framework finding geodesics on a Riemannian manifold based on diffusion tensors [74]. Similarly, Prados *et al.* and Lenglet *et al.* demonstrated a Riemannian based technique, GCM (Geodesic Connectivity Mapping), for computing geodesics using a variant of fast marching methods adapted for directional flows [85, 51]. Jackowski *et al.* find Riemannian geodesics using Fast Sweeping methods as given by Kao *et al.* [34, 39, 40]. Pichon *et al.* and Melonakos *et al.* use the more general Finsler metric to find optimal connections [79, 82, 59, 57]. Finally, Fletcher *et al.* propose a new Hamilton-Jacobi-Bellman numeric solver on the graphics processing unit to find Riemannian geodesics in near real-time speeds [23]. In each of these cases, an optimal path is found which represents the best connection between the two regions under the given metric.

### ***4.3 The Cingulum Bundle***

In this section, we motivate the problem of segmenting the cingulum bundle. The cingulum bundle is a 5-7 mm in diameter fiber bundle that interconnects all parts of the limbic system. It originates within the white matter of the temporal pole, and

runs posterior and superior into the parietal lobe, then turns, forming a "ring-like belt" around the corpus callosum, into the frontal lobe, terminating anterior and inferior to the genu of the corpus callosum in the orbital-frontal cortex [90]. Moreover, the cingulum bundle consists of long, association fibers that directly connect temporal and frontal lobes, as well as shorter fibers radiating into their own gyri. The cingulum bundle also includes most afferent and efferent cortical connections of cingulate cortex, including those of prefrontal, parietal and temporal areas, and the thalamostriatae bundle. In addition, lesion studies document a variety of neurobehavioral deficits resulting from a lesion located in this area, including akinetic mutism, apathy, transient motor aphasia, emotional disturbances, attentional deficits, motor activation, and memory deficits. Because of its involvement in executive control and emotional processing, the cingulum bundle has been investigated in several clinical populations, including depression and schizophrenia. Previous studies, using diffusion tensor imagery, in schizophrenia, demonstrated decrease of fractional anisotropy in the anterior part of the cingulum bundle [47, 112], at the same time pointing to the technical limitations restricting these investigations from following the entire fiber tract.

#### ***4.4 The Algorithm***

In this section, we present our method for applying local constraints to region-based flows, using the optimal paths generated by any of the optimal path approaches mentioned in Section 4.2.

First, in Subsection 4.4.1, we motivate the need for the local constraints. Then, in Subsection 4.4.2, we describe prior work in volumetric fiber bundle segmentation and point out where our approach can offer improvements to these algorithms. Finally, in Subsection 4.4.3, we explain how the local constraints may be cast in a Bayesian framework leveraging the optimal connections, or *anchor tracts*, to achieve the desired

result.

#### 4.4.1 Motivation for Local Constraints

An implicit assumption of classical (i.e., those which compare features across the full interior with features from the full exterior) region-based approaches is that the entire interior of the contour contains fairly homogeneous features, such as mean intensity. Under this assumption, these algorithms proceed by evolving the closed curve or surface to minimize an energy defined over these features.

However, if there are no homogeneous features across the entire interior or exterior of the object of interest, it becomes difficult to define a region-based approach which will accurately segment the image. For instance, in the case of the cingulum bundle which curves around the ventricles, the tensors across the fiber bundle vary in both anisotropy and orientation across the length of the bundle, as shown in Figure 14. In this sagittal view, we see that it is difficult to define a feature on the space of tensors which uniquely separates the entire interior of the cingulum bundle from the exterior. However, we also notice that the tensor shape and anisotropy vary smoothly across the bundle. Hence, locally across the fiber one can define tensor features which are distinguishable from the exterior.

#### 4.4.2 Prior Work

Surface evolution approaches have been described for fiber bundle segmentation. Rousson *et al.* [88] use a multi-variate Gaussian distribution of the tensor components in a geodesic active region model to drive a surface evolution towards the segmentation of fiber bundles. The method is applied to the segmentation of the corpus callosum, but is unable to fully capture its curved character as discussed by the authors. In a follow-up paper [50] a similar segmentation framework in combination with a geodesic distance between tensors is shown to yield superior segmentation results, in particular, when segmenting curved fiber bundles. Jonasson *et al.* propose two different ways

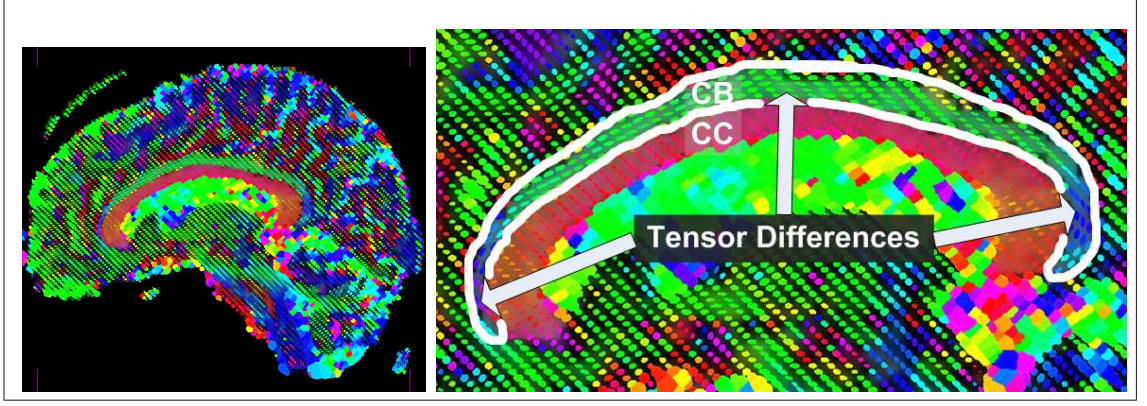


**Figure 14:** Example of the need for local constraints on region-based segmentation algorithms which attempt to segment the cingulum bundle. Notice that tensor anisotropy and orientation vary across the length of the cingulum bundle.

to address the segmentation of curved fiber bundles in a surface evolution setting: (i) a local approach [37], where the surface evolution speed is influenced by the similarity of a tensor in comparison to its interior neighbors, and (ii) a region-based approach, where the similarity measure is based on the notion of a most representative tensor within the segmented region [38]. In the latter case, capturing highly curved fiber bundles will be problematic. In both cases the segmentation algorithm is combined with a surface regularization to prevent leaking. The approach proposed in this chapter is related to Jonasson’s work [37] in as much as it uses local tensor similarities to drive the segmentation, however, no surface evolution is used and a tensor similarity measure is combined with prior information as given by an initially computed anchor tract (also preventing large-scale leaking). The extension of the approach proposed in this chapter (see Section 4.7) can be seen as complementary to the method by Lenglet *et al.* [50]. Instead of disentangling tensor shape and orientation through an appropriate tensor distance (and statistic) the anchor tract may be used to warp the space initially, thus effectively removing large orientation differences<sup>2</sup>. Further, due to the absence of a surface evolution, our approach is computationally very efficient.

<sup>2</sup>Our approach may also be combined with the method proposed in [50].

#### 4.4.3 Bayesian Framework

In this section, we describe how the algorithm can be formulated in a Bayesian framework. We follow the approach by Mumford [68] and cast the Bayesian estimation problem into an energy minimization. The probability of observing the classification  $C$ , consisting of points belonging to the fiber and points belonging to the background given the tensor information  $T$  is (using Bayes' formula):

$$p(C|T) = \frac{p(T|C)p(C)}{p(T)} \sim p(T|C)p(C), \quad (18)$$

where  $C$  is an element of the set of all possible assignments of voxels to the fiber and the background respectively,  $p(T|C)$  is the likelihood of observing  $T$  given the classification  $C$  and  $p(C)$  is the prior. By taking the logarithm on both sides and noting that  $p(T)$  is independent of the classification  $C$ , Equation (18) can be written as an energy minimization problem [68]

$$\begin{aligned} E(C) &= -\log(p(C, T)) \\ &= -\log(p(T|C)) - \log(p(C)) \\ &= E_d(T, C) + E_p(C), \end{aligned} \quad (19)$$

where  $E_d(T, C)$  denotes the data energy and  $E_p(C)$  the prior (or regularization) energy. Instead of solving the Bayesian estimation problem (18) directly we may thus instead minimize the energy (19). Which leaves us with defining these energies. We use a flood-fill algorithm approach that solves the energy minimization problem (19) for an individual point only considering its local neighborhood  $N$ . In what follows we first describe the continuous setting, to make connections with existing approaches, and then describe the discrete implementation in the context of the proposed Bayesian flood-fill algorithm. Given the local neighborhood  $N$  of a point  $\mathbf{x}$  we want to decompose it into a subregion belonging to the fiber and a subregion belonging to the background. The goal of our algorithm is to make each of these two subregions

individually as uniform as possible, while at the same time using anatomically meaningful prior information. The prior information is encoded based on the distance of the pre-computed anchor tract, which is the lowest cost path connecting two maximally spaced-out, pre-defined regions of interest of the fiber bundle of interest (in our case the cingulum bundle). Specifically, we choose  $p(C)$  as

$$p(\mathbf{x}) = s_G(d(\mathbf{x})), \quad (20)$$

where  $d(\mathbf{x})$  is the distance of point  $\mathbf{x}$  from the anchor tract and

$$s_G(r) = G_\sigma * \begin{cases} 1 & \text{for } |r| > \mu_{min} \\ \frac{1}{2} & \text{for } \mu_{min} \leq |r| \leq \mu_{max} \\ 0 & \text{otherwise,} \end{cases}$$

where  $G_\sigma$  is a Gaussian with standard deviation  $\sigma$  and  $*$  is the convolution operator;  $\mu_{min}$  and  $\mu_{max}$  are set to the range of expected radius values. Note, that the prior could also be replaced by a probabilistic atlas. Equation (20) describes an initial zone of high fiber confidence close to the anchor tract, a transitioning region (where  $p(C) = 1/2$ ) where the prior information will not be used<sup>3</sup>, and an anatomically implausible region, where the prior probability decreases to zero. The prior energy is then defined as

$$E_p(C) = \frac{1}{|N|} \left( \int_{N_f} 1 - p(\mathbf{x}) \, d\Omega + \int_{N_b} p(\mathbf{x}) \, d\Omega \right), \quad (21)$$

where  $N_f$  is the region belonging to the fiber  $N_b$  is the region belonging to the background and  $|\cdot|$  denotes cardinality, i.e.,  $|N|$  is the volume of the neighborhood. Given a measure of uniformity  $D : \mathcal{T} \times \mathcal{S}_N \mapsto \mathbb{R}_0^+$  mapping from the space of tensors  $\mathcal{T}$  and the space of neighborhood sets of tensors  $\mathcal{S}_N \ni T(N) := \{T(\mathbf{x}) \in \mathcal{T} | \mathbf{x} \in N\}$  to a

---

<sup>3</sup>If  $p(C) = 1/2$ , the prior energy (21) is independent of assigning the candidate flood-fill point to the fiber or the background.

non-negative real value, we write the data energy as

$$E_d(T, C) = \frac{1}{|N|} \left( \int_{N_f} D(T(\mathbf{x}), T(N_f)) d\Omega + \int_{N_b} D(T(\mathbf{x}), T(N_b)) d\Omega \right),$$

where  $T(\mathbf{x})$  denotes a tensor at position  $\mathbf{x}$  and  $T(N)$  denotes the set of tensors in the region  $N$ . This is an energy similar to the one proposed by Chan and Vese [15] for the segmentation of intensity images<sup>4</sup>. Note, however, that instead of using this energy globally to perform tensor segmentation, we are proposing to use this energy in a local neighborhood to make a local decision for a flood-fill algorithm, thus avoiding global tensor orientation issues for strongly curving fiber bundles. To minimize this energy in the discrete flood-fill setting, we simply compute the difference of the energies when adding the voxel in question to either the fiber (resulting in energy  $E^f$ ) or to the background (resulting in energy  $E^b$ ). The difference of these energies  $\Delta E = E^b - E^f$  corresponds to a discretized gradient. Since our goal is to minimize the overall energy, a voxel  $\mathbf{x}$  will be added to the set of fiber voxels if  $\Delta E > 0$ . All integrals in Equations (21) and (4.4.3) become sums in the discretization. Many uniformity measures are possible (see for example [38, 37, 1] for some ideas on how-to compare tensors), we constructed a simple one based on fractional anisotropy and the major diffusion direction:

$$D(T(\mathbf{x}), T(N)) = \frac{1}{2} \left( D_{FA}(T(\mathbf{x}), T(N)) + D_{e_1}(T(\mathbf{x}), T(N)) \right),$$

where

$$D_{FA}(T(\mathbf{x}), T(N)) = |FA(T(\mathbf{x})) - \overline{FA(T(N))}|$$

measures the uniformity in fractional anisotropy and

$$D_{e_1}(T(\mathbf{x}), T(N)) = 1 - \sqrt{FA(T(\mathbf{x})) \overline{FA(T(N))}} \times e_1(T(\mathbf{x}))^T \frac{\overline{\lambda_1(T(N)) e_1(T(N))}}{\|\overline{\lambda_1(T(N)) e_1(T(N))}\|}$$

measures the uniformity in direction. Fractional anisotropy (FA) is defined as [7]

$$FA = \sqrt{\frac{3}{2} \frac{\sqrt{(\lambda_1 - \lambda_2)^2 + (\lambda_1 - \lambda_3)^2 + (\lambda_2 - \lambda_3)^2}}{\sqrt{\lambda_1^2 + \lambda_2^2 + \lambda_3^2}}}$$

---

<sup>4</sup>To favor “smooth” discrete boundaries, a local boundary length term can be added.

where  $e_1(T)$  denotes the major unit eigenvector of the tensor  $T$ ,  $\lambda_i(T)$  its eigenvalues (with  $\lambda_1 \geq \lambda_2 \geq \lambda_3 \geq 0$ ), and the overhead bar signifies the mean<sup>5</sup>.  $D_{e_1}$  is scaled by fractional anisotropy to discard tensors that are close to being isotropic, since in these cases eigenvector computations become numerically problematic. The continuous approach could alternatively be implemented using fast marching or level sets. In this work, we use a very simple flood-fill approach which propagates away from the anchor tract. Certainly other methods would offer a more continuous and numerically accurate approach. However, our simple flood-fill implementation is sufficient as a proof-of-concept.

The algorithm proceeds in the following steps:

- (i) Declare all voxels on the anchor tract as fiber voxels.
- (ii) Consider all 6-connected neighbors to the fiber voxels that are not fiber voxels themselves as candidate voxels.
- (iii) Decide whether a candidate voxel should belong to the fiber based on the simple local energy minimization described above (where the neighborhoods  $N_f$  and  $N_b$  are given by the voxels in the current neighborhood  $N$  that already belong to the fiber or are so far classified as background respectively). If a candidate voxel should be part of the fiber according to the local energy minimization, add it as a fiber voxel.
- (iv) Repeat from step (ii) until no more new fiber voxels are found.

Using the Bayesian framework, the outward propagating front stops once the Bayesian detection threshold is reached, i.e., once all boundary voxels are in locally minimal energy configurations.

---

<sup>5</sup>FA may be computed directly from the tensor components without computing the tensor eigenvalues first [7].

## 4.5 Experiments

In this section, we show results of the algorithm applied to DW-MRI datasets of 51 sampling directions. We used the Finsler tractography method proposed by Melonakos *et al.* to compute the anchor tracts or optimal paths between two input seed regions [57]. The seed regions were manually segmented, one under the anterior tip of the ventricles and the other under the posterior tip of the ventricles.

Using precomputed anchor tracts, we were able to construct our priors using the function shown in Figure 15, as previously described (mean radius  $\bar{r} = 3$  mm,  $\mu_{min} = \frac{1}{2}\bar{r} = 1.5$  mm,  $\mu_{max} = \frac{3}{2}\bar{r} = 4.5$  mm,  $\sigma = \frac{1}{8}\bar{r} = \frac{3}{8}$ ). Applying this function to a distance map from the anchor tract, the prior image is as shown on the left side of Figure 16. The white colored area is where the uniform priors are centered on the mean value of the cingulum bundle radius, which we take to be 3 mm as described in Section 4.3. In the middle of Figure 16, we show the likelihood energy gradient computed from the evolution (where positive values are likely to belong to the bundle and negative values are not likely to belong to the bundle). Notice how the likelihood energy function captures an appropriate boundary across a majority of the cingulum fiber bundle. The orientation dependent terms had the strongest influence on the inferior edge against the corpus callosum. The anisotropy dependent terms had the strongest influence on the superior edge. On the right side of Figure 16, we show the posterior energy gradient, which results from the combination of likelihood energy and prior energy terms.

In Figure 17, we show a 3D model view of the resulting segmentation. Then, in Figure 18, we show three separate time steps in the flood-fill evolution. The first column is at 1 iteration, the second column is at 3 iterations, and the final column is at 18 iterations-where all three methods had converged. The top row shows the evolution using only the priors. Notice how the result is a smooth tube exactly matching the prior that is too wide for this individual and ends up overlapping proximal anatomy,

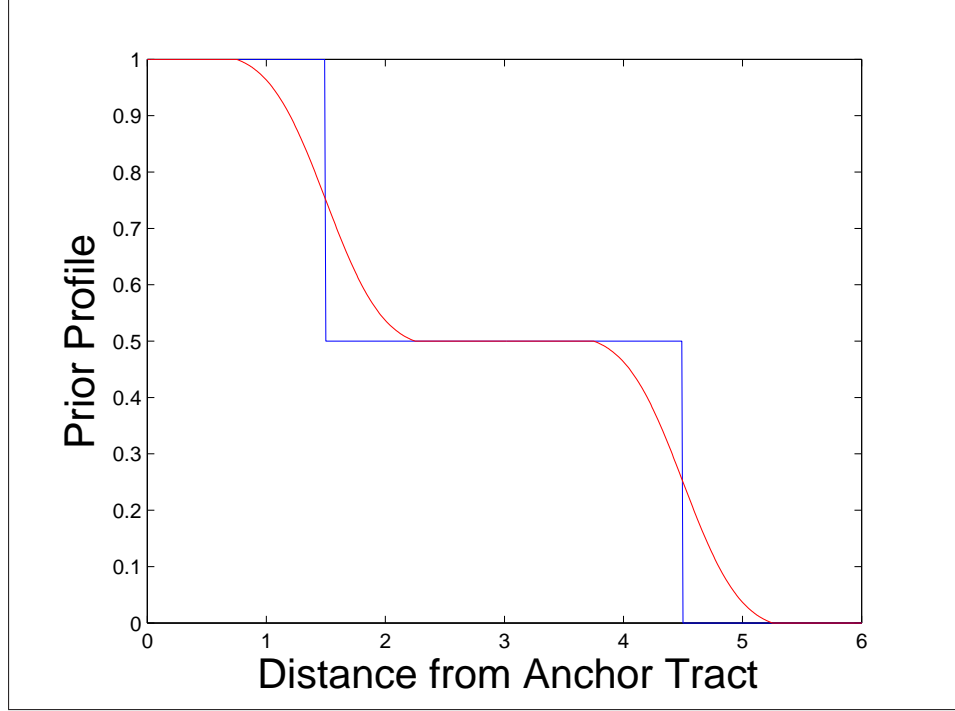


**Figure 15:** The prior profile: Blue is the initial step function, Red is the actual profile after smoothing. Note the region of uniform priors (0.5), centered around the clinically defined mean fiber radius.

such as the corpus callosum. The middle row shows the evolution using only the likelihoods. While this result appropriately captures the majority of the bundle, it is subject to a few leaks as shown. The bottom shows the evolution using the Bayesian combination of the likelihoods and priors. This result shows an appropriate combination of the likelihood boundary stopping and the prior leakage constraints.

We also note that the few parameters used in this method can be chosen given anatomical information about the mean radius of the fiber bundle. The prior energy function is only dependent upon this parameter, as mentioned previously. Also, the neighborhood size is chosen to be large enough so that at least 20% of the neighborhoods on the first iteration include voxels exterior to the fiber bundle. In this case, we chose a neighborhood radius of 7 mm. No other parameters were needed in this computation.

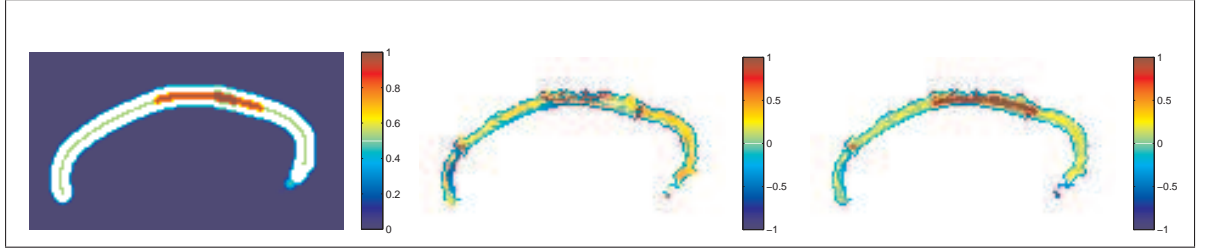


**Figure 16:** The prior energy (left), likelihood energy (middle), and posterior energy (right).

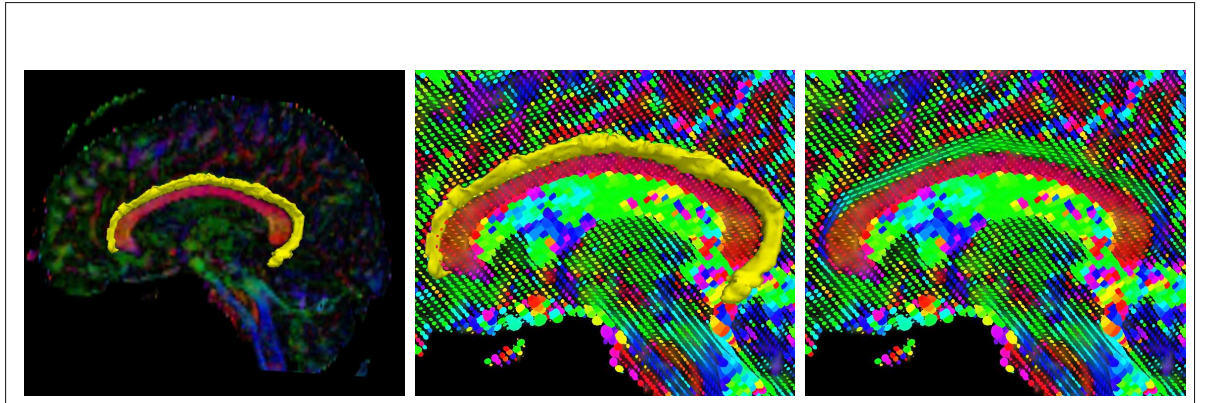


**Figure 17:** A 3D view of the result.

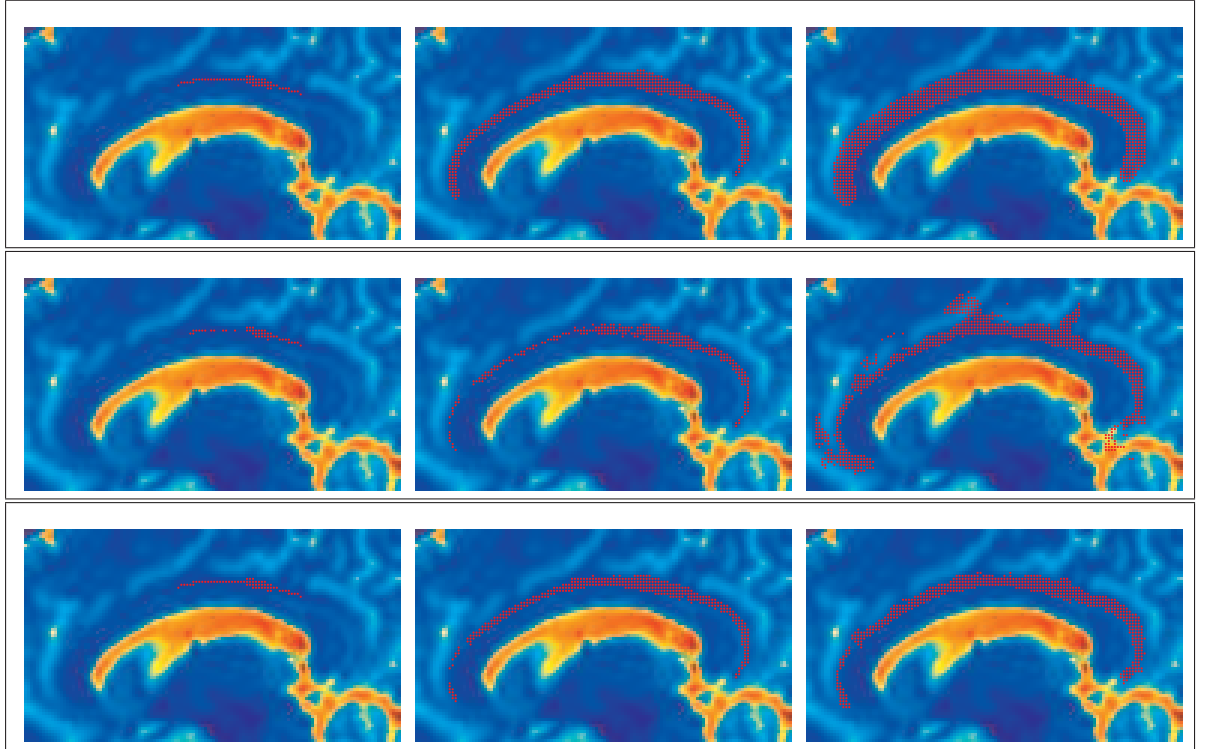


**Figure 18:** Front evolution time steps: Top Row is the evolution with only the priors. Middle Row is the evolution with only the likelihoods. Bottom Row is the evolution from the Bayesian inclusion of both the likelihoods and priors.

## 4.6 Tensor Warping

In this section, an alternative method is presented for volumetric segmentation based on a warping of the tensor field about a representative fiber tract [69]. This section proposes a new segmentation method for near-tubular fiber bundles. It is based on reorientation of diffusion measurements resulting in more uniform data distributions inside the fiber bundle of interest. Segmentation is performed by an efficient convex approximation of the probabilistic Chan-Vese energy using region-based directional statistics. The approach compares favorably to streamline approaches for bundle segmentation.

### 4.6.1 Motivation and Algorithm

Figure 19 illustrates diffusion tensors changing direction along a fiber bundle and the same set of diffusion tensors when realigned relative to a representative fiber tract. This realignment process is at the core of the approach proposed in this paper. Realignment simplifies the original problem by making it spatially stationary. Segmentation methods for vector-valued images can then be employed for fiber bundle segmentation. Note that standard streamline tractography usually incorporates a weak, implicit form of spatial realignment by disallowing orientation changes considered too drastic.

The proposed approach is:

- 1) Find a representative fiber tract (e.g., by streamlining, by an optimal path approach, or through atlas warping of a predefined representative fiber tract).
- 2) For every candidate point in the image volume, find the *closest* point on the representative fiber tract.
- 3) Regard the candidate point as part of the fiber bundle if its diffusion information is *similar* to the diffusion information at the closest point.

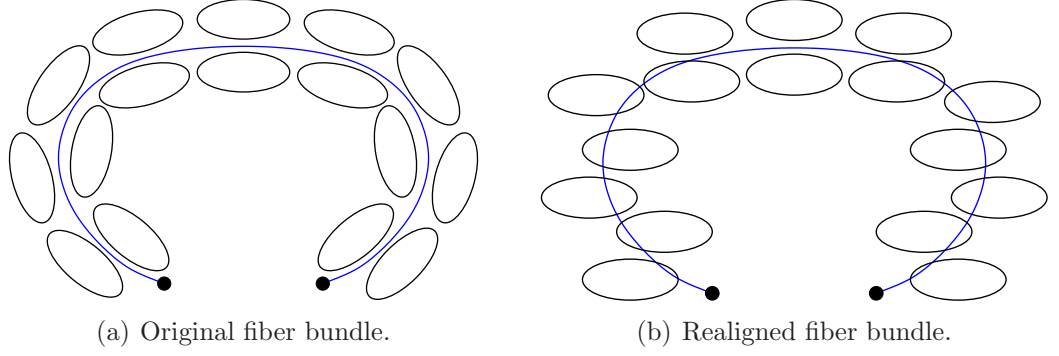


**Figure 19:** Tensor reorientation concept. The spatially varying tensor orientation can largely be removed by reorientation with respect to a representative fiber tract (blue).

- 4) Create a *spatially consistent* segmentation based on the similarities of 3).

#### 4.6.2 Results

This subsection gives results for the tensor warping segmentation approach. Synthetic examples are discussed in Section 4.6.2.1. Section 4.6.2.2 presents results for a real DW-MRI of the brain and compares them to segmentation results obtained through streamline tractography based on the major eigenvectors of the diffusion tensors and Runge-Kutta numerical integration.

##### 4.6.2.1 Synthetic example

A synthetic tensor example was generated. Tensors are assumed of uniform shape with eigenvalues  $(1.5, 0.5, 0.5)e-3$  oriented along a circular path to model a fiber bundle. Tensors oriented orthogonally to the circular path model the outside. Diffusion weighted images were generated using the Stejskal Tanner equation  $S_k = S_0 e^{-b \mathbf{g}_k^T T \mathbf{g}_k}$ , where  $S_k$  denotes the diffusion weighted image acquired by applying a gradient direction  $\mathbf{g}_k$  with b-value  $b$ , and  $T$  the diffusion tensor. Parameters were  $S_0 = 1000$ ,  $b = 1000$  with 46 gradient directions distributed on the unit sphere using an electric repulsion model and enforcing icosahedral symmetry. Rician noise of  $\sigma = 70$  was introduced to the baseline image  $S_0$  (non-diffusion weighted) and the diffusion weighted

images  $S_k$ . Figure 20 shows the original data and the resulting segmentation on the top row (with the streamline indicating the computed representative tract) and the reoriented data with associated segmentation on the bottom row. For this synthetic example, reorientation results in an almost perfectly uniform tensor distribution on the inside and the outside of the simulated fiber bundle. Consequently, while the proposed approach fails at segmenting the original data, it segments the reoriented data well. Note, that the failure to segment the original data is not merely a result of the segmentation method employed. Any segmentation relying purely on region-based statistics will either have to include some of the background in its bundle segmentation or will severely under-segment the bundle itself, since background and foreground are not clearly separable based on global statistics. While including edge-based terms may improve the segmentation of the original data, regional terms will be of limited use and will locally counteract the edge influence requiring a delicate balance between region-based and edge-based energies to faithfully segment the simulated fiber bundle.

#### 4.6.2.2 *Real example*

The real example was computed for the cingulum bundle using a 3T DW-MRI up-sampled to isotropic resolution ( $0.93 \text{ mm}^3$ ) with 8 baseline images and 51 gradient directions distributed on the sphere by electric repulsion ( $b=586$ ). The representative tract was computed using streamline tractography.

Figure 21 shows color by orientation representations for a sagittal slice through the brain with the cingulum bundle (mainly in green) before and after reorientation. The reoriented image shows a consistently green cingulum bundle, whereas in the original image the cingulum bundle is colored blue when wrapping posteriorly around the corpus callosum, indicating a change of orientation from anterior-posterior to superior-inferior. This result demonstrates the beneficial effect of reorientation on the real data set (effectively removing large-scale geometry effects), which allows for fiber

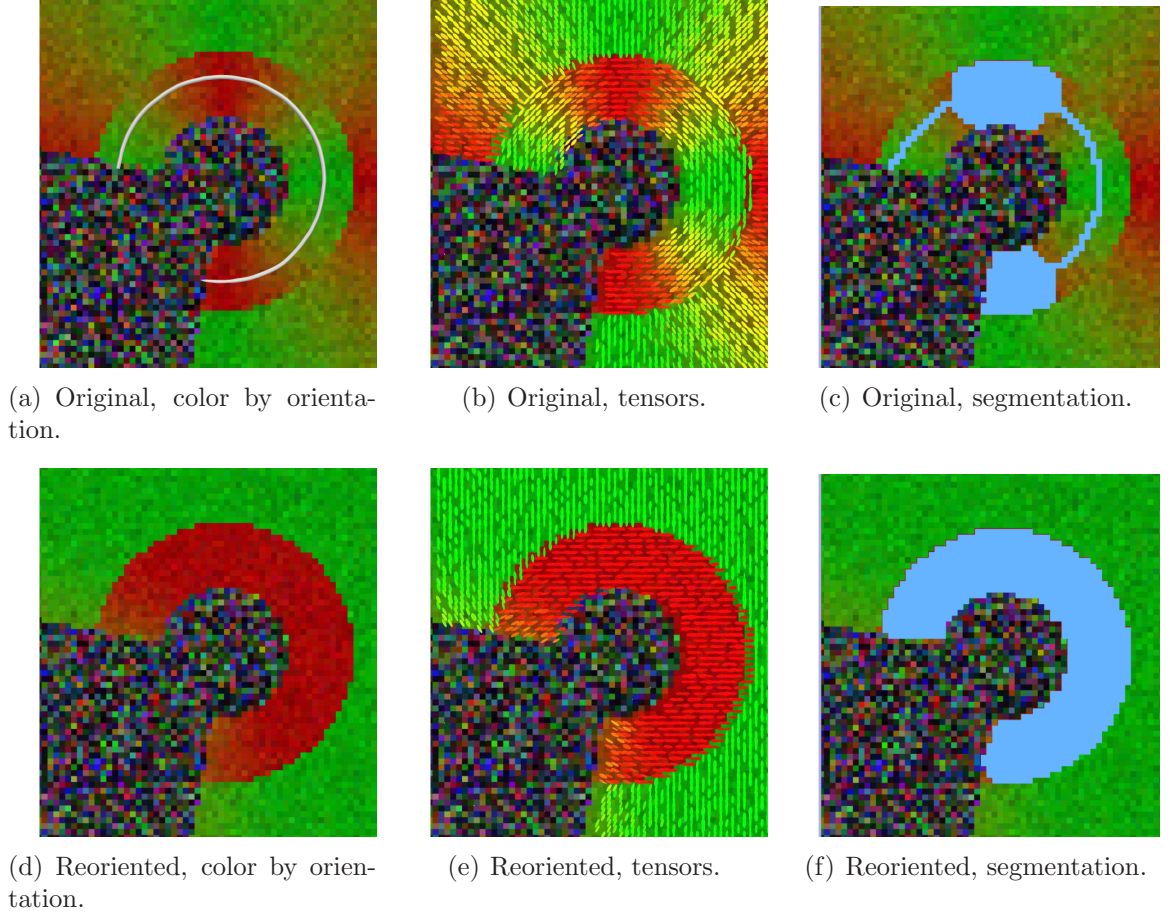


**Figure 20:** Segmentation of a synthetic example. Reorienting diffusion information based on the representative streamline (top left) result in almost uniform tensor distributions interior and exterior to the fiber bundle. While segmentation for the original data is difficult and leads to unsatisfactory results, segmentation of the reoriented data is much easier leading to a faithful segmentation with the proposed approach.

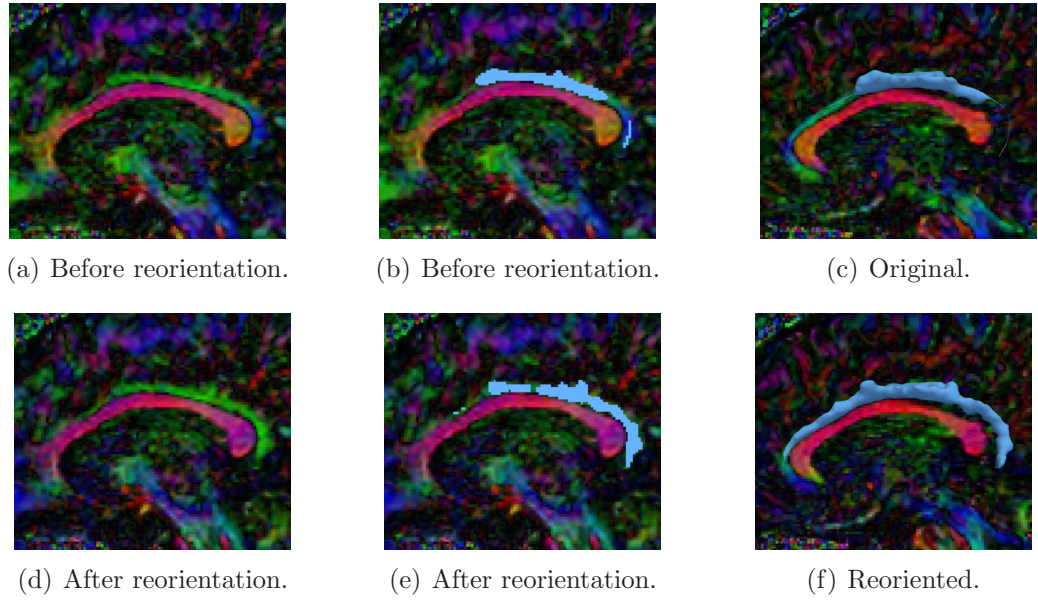


**Figure 21:** Sagittal slice of the cingulum bundle, before and after tensor reorientation. The cingulum bundle appears more uniform in direction (green) after reorientation. Reorientation greatly improves the segmentation result of the proposed approach.

bundle segmentation with a global statistical model. Example segmentation results of the proposed approach are shown for the reoriented and the original data. The surface models generated from the computed segmentations show that the segmentation for the reoriented data approximates the cingulum bundle more faithfully.

Finally, to demonstrate the strength of the reorientation approach, Figure 22 gives an example for the cingulum bundle segmentation at a posterior slice of the cingulum bundle where the cingulum bundle wraps around the corpus callosum. While in the reoriented case the segmentation is successful and the direction of the cingulum bundle is uniform (green), the segmentation on the original data fails in this part of the fiber bundle.

To compare the proposed methods to alternative segmentation approaches, the cingulum bundle was segmented using a region of interest based approach (the same regions of interest used to generate the representative fiber tract for reorientation). Two small axial regions of interest were defined for the cingulum bundle (superiorly to

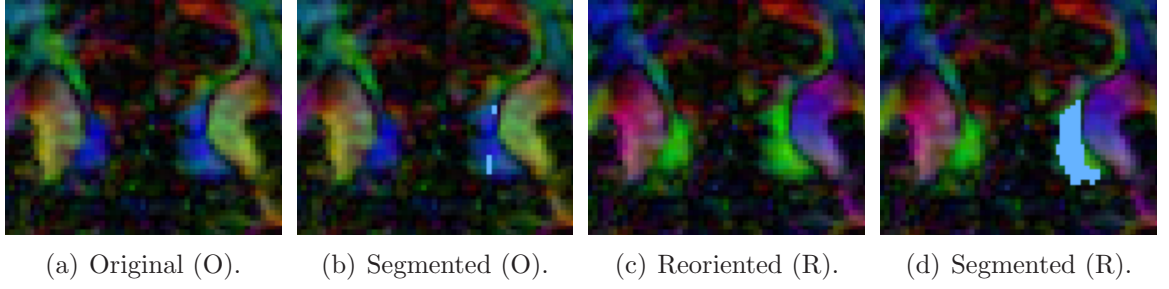


**Figure 22:** Effect of reorientation on orientation and segmentation, depicted for a posterior coronal slice. Reorientation results in a consistent orientation of the cingulum bundle changing from blue to green, indicating a directional change from inferior-superior to posterior-anterior. While segmentation using the proposed approach fails for the original data it succeeds after reorientation.

the corpus callosum). Streamline tractography with voxelization, full brain streamline tractography with voxelization, as well as segmentation on the original and reoriented data using the proposed approach was performed. Figure 23 illustrates segmentation results for these methods for coronal slices in the superior part of the cingulum bundle (where the cingulum bundle is *not* strongly curved). As expected streamline tractography and full brain streamline tractography mainly capture the interior of the fiber bundle, with full brain tractography performing qualitatively better than standard region of interest based streamline tractography (streamlines were seeded one per voxel in the regions of interest). The proposed segmentation approach captures the cingulum bundle well for the reoriented and for the original data, showing the utility of segmenting in orientation space. However, the reoriented segmentation results are better where the cingulum bundle curves strongly, as shown in Figure 22.

## 4.7 Conclusions

This chapter proposed a novel segmentation method for diffusion tensor images. The approach is based on a Bayesian region growing, where the prior depends on the distance to a pre-computed anchor tract. The anchor tract is given by the optimal path in a Finsler metric (though any other robust method giving a representative fiber

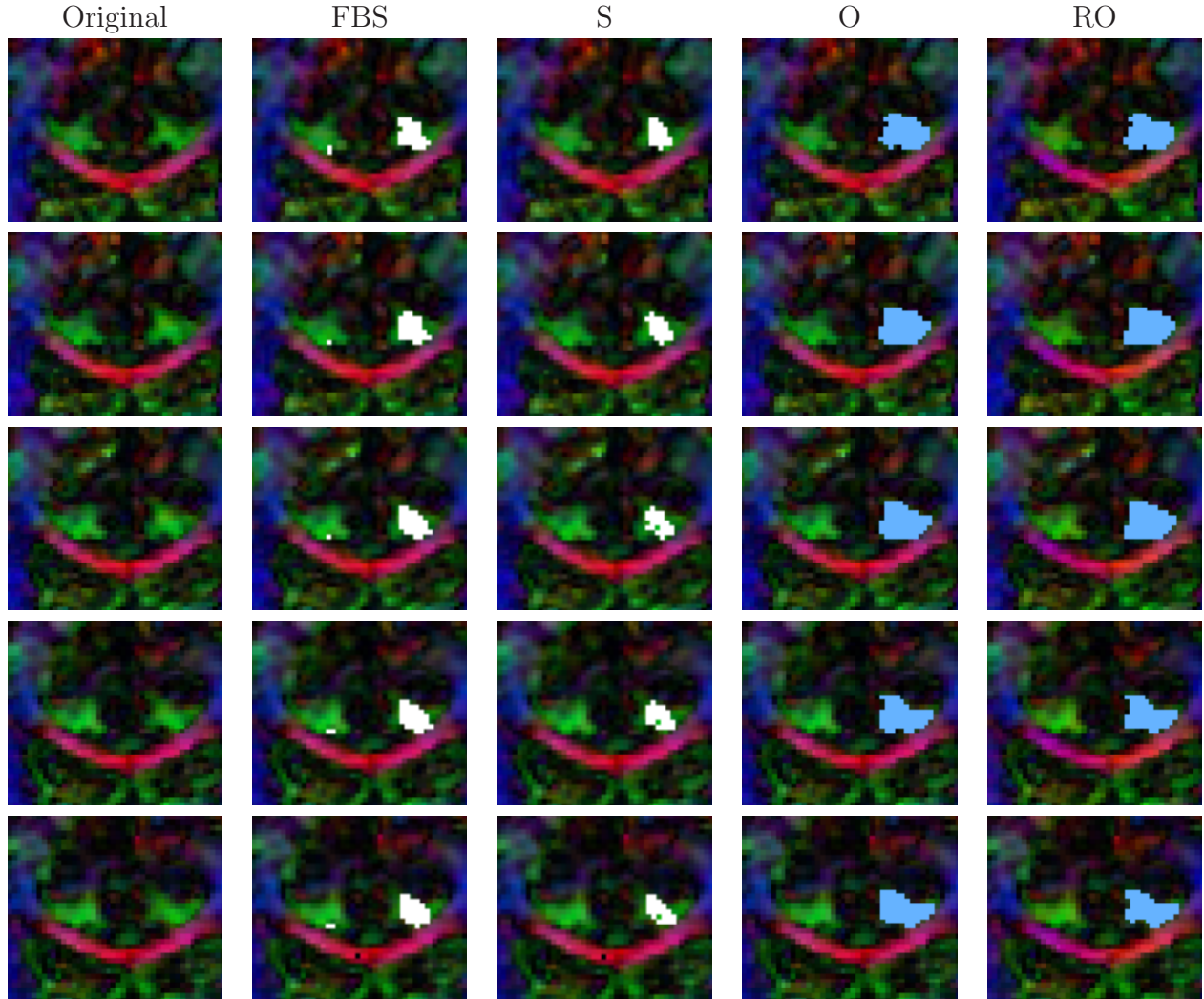


**Figure 23:** Superior coronal slices: Original data; results for streamline (S) and full brain streamline (FBS) tractography, for the proposed segmentation on original data (O) and on reoriented data (RO). Only the proposed approach segments up to the perceived bundle boundary in orientation space.

path could be used), utilizing the full diffusion profile. The likelihood is determined based on the consistency of a candidate voxel with its neighbors that are already part of the segmentation. (i.e. the likelihood is dynamically updated as the region is growing.) The Bayesian combination of likelihood and prior allows for a balanced combination of local consistency and distance from the optimal path, which also inhibits segmentation leakage. The approach is computationally efficient.

Region-based segmentation algorithms have been highly successful in segmenting uniform (in a given measure) regions. In this work, we showed how translating this global region-based approach to diffusion weighted imaging for the segmentation of fiber bundles is accomplished. In particular, many fiber bundles in the brain curve strongly (e.g. the cingulum bundle, the arcuate fasciculus, the corpus callosum) and benefit from the approaches described in this work.

## CHAPTER V

### BRAIN MRI TISSUE CLASSIFICATION

In this chapter, we present an approach for the segmentation of brain MRI tissue into gray matter, white matter, and cerebral spinal fluid [55]. In particular, the white matter segmentation may be used as a mask for the guidance and constraint of the geodesic tractography segmentation algorithms presented in the previous chapters.

#### *5.1 Introduction*

Bayesian classification methods have been extensively used in a variety of image processing applications, including medical image analysis. The basic procedure is to combine data-driven knowledge in the likelihood terms with clinical knowledge in the prior terms to classify an image into a pre-determined number of classes. There is an extensive body of work which examines classification in this context using brain atlases and other spatial and shape priors on the medical image data [84, 108, 41]. Frequently, however, algorithms are required to perform in the absence of sufficient prior clinical knowledge and researchers revert to maximum-likelihood estimation which assumes uniform priors on the data.

In Figure 24, a categorization is portrayed which depicts a grouping of classification strategies which operate in the absence of clinical prior information. On the left, we show our algorithm which makes use of the prior terms by casting the classification problem in a slice-by-slice iterative framework. In the middle, we show our algorithm with uniform priors in a volumetric non-iterative framework. On the right, we group all other 3D classification algorithms which use uniform priors.

In this chapter, we explore the use of minimal prior information. Simply stated, we wish to make use of the prior terms by incorporating useful information which

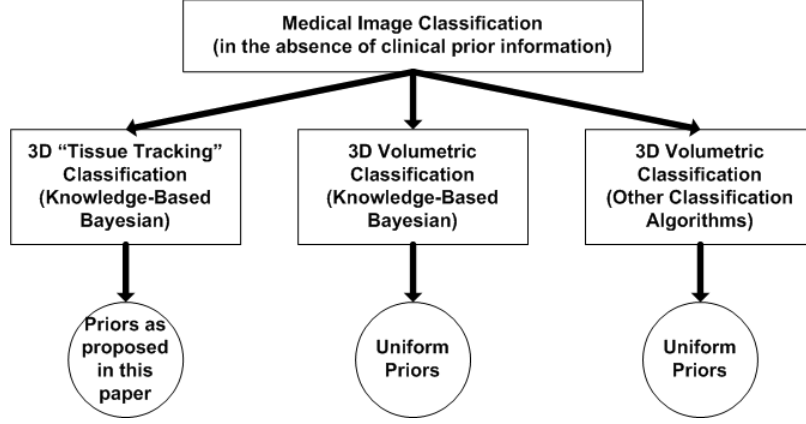


**Figure 24:** Medical Image Classification Strategies

can be entirely derived from the image header and data itself. The prior information we propose to use includes a combination of expectation-maximization weights and neighboring posterior probabilities. This will be described in greater detail in Section 5.2.3.

Before introducing our tissue tracking algorithm, we will discuss other Bayesian classification algorithms in Section 5.2.1 and 5.2.2. Second, in Section 5.2.3, we will outline our tissue tracking algorithm. Third, in Section 5.3, we will outline our experiments on 20 brain MRI data-sets. And, finally, in Section 5.4, we will present our results.

## 5.2 Bayesian Classification Algorithms

In the first two subsections, we present previous work on Bayesian classification algorithms. First, we present work by Haker *et al.* [31] which outlines the general structure of Bayesian classification for tracking applications. Next, we present similar work by other groups which has been adapted for volumetric medical image segmentation. Then, in the last subsection, we present our work which casts the medical image segmentation into a tracking framework.

### 5.2.1 2D Tracking Algorithms

Several groups have previously proposed Bayesian classification algorithms. Most relevant to our work is the work by Haker *et al.* on the tracking of objects in 2D time-lapsed sequences of Synthetic Aperture Radar (SAR) data [31].

At each time step in the tracking framework, the algorithm classifies the given 2D image slice into  $N$  classes. The segmentation proceeds as follows:

First, the image data is used to generate likelihood probabilities,  $p(V|C)$ , for a class  $C$  and an intensity value  $V$ . Typically, a normal distribution is assumed on the data and the parameters of the distribution are estimated from the 2D slice.

Next, prior probabilities are constructed. In [31], it is suggested that good results can be achieved by setting the priors of the current slice to the posteriors of the previous slice. This has a smoothing effect across time and tends to help push through noise which may occur on slices in time.

In the last step of the algorithm, the likelihood and prior probabilities are used to compute the posterior probabilities,  $p(C|V)$ , via Bayes' Rule. Following the application of Bayes' Rule, each of the  $N$  components of the posteriors are independently spatially smoothed using the anisotropic smoother of Olver *et al.* [72]. Teo *et al.* showed that such a smoothing of the posteriors results in a more effective noise removal than a smoothing of the original data [104].

Finally, the segmentation is completed by assuming that each pixel belongs to the class of maximum probability. It is well known that this "Maximum a posteriori test" minimizes the probability of segmentation error.<sup>1</sup> Using this decision rule, a final segmentation or label-map is constructed from the smoothed posterior probabilities.

---

<sup>1</sup>It is possible for one to assign various subjective costs for different types of segmentation errors and to then generalize this MAP test to minimize the average Bayes risk; however, we do not wish to penalize any type of error in particular, so the MAP test seems appropriate.

### 5.2.2 Volumetric Medical Image Classification

Previously, Teo *et al.* [105] presented results of volumetric Bayesian segmentation on brain MRI scans. Their Bayesian segmentation algorithm was used to detect the white/gray matter boundary. Their algorithm is very similar to the algorithm stated above in Section 5.2.1. However, instead of iterating through the slices, they simply classified the entire volume in one shot. Therefore, they assumed homogeneous priors. Like the algorithm above, they also smoothed the posteriors and applied a MAP decision rule to achieve segmentation.

After applying the Bayesian classification algorithm, Teo *et al.* perform a surface growing morphology operation to grow gray matter uniformly across the white matter surface to a predetermined thickness. They explain the due partial volume effects it is difficult to achieve accurate gray matter segmentations in MRI using this technique.

In other related work, Yang *et al.* [115] developed a Bayesian segmentation algorithm for the segmentation of coronary arteries. In this case, homogeneous priors are also employed. Furthermore, this algorithm works in conjunction with an active contour model to achieve the final result.

### 5.2.3 Tissue Tracking

In this subsection, we present the details of our *tissue tracking* algorithm. Specifically, we show how expectation-maximization weights and posterior probabilities may be combined to make intuitive use of the Bayesian priors. Afterwards, we show results of our algorithm on 20 brain MRI data-sets along with validation against expert manual segmentations.

We proceed in a similar fashion as previously introduced in Section 5.2.1. However, since the data is not time-lapsed, we view the scan axis as the axis of tracking. In Figure 25, we present the basic idea. This algorithm works by iteratively sweeping through the image volume and classifying the volume slice-by-slice. The resulting



**Figure 25:** Tissue Tracking General Structure

classification is 3D due to the fact that information is passed between slices through the iterative process.

As in the other algorithms, this algorithm depends upon the user choosing the number,  $N$ , of predetermined classes into which the imagery is to be classified. As before, at each step of the iteration through the data-set, our algorithm classifies the given 2D image slice into  $N$  classes. The segmentation proceeds as follows, refer to Figure 26 for an overview:

First, the image data is used to generate likelihood probabilities,  $p(V|C)$ , for a class  $C$  and an intensity value  $V$ . We assume that the intensities in a given image represent samples from a Gaussian mixture model comprised of  $N$  clusters. The parameters for each Gaussian component of the mixture model can be estimated via the expectation-maximization (EM) algorithm. We use the EM algorithm presented by Bilmes *et al.* [10] to estimate the means and variances along with the component weights which provide a measure of the prior probability for each given class.

Next, we construct the prior probabilities,  $p(C)$ . In many applications, it is difficult to construct meaningful priors by bringing non-data-driven information into the segmentation framework, and thus uniform priors are often employed. We suggest

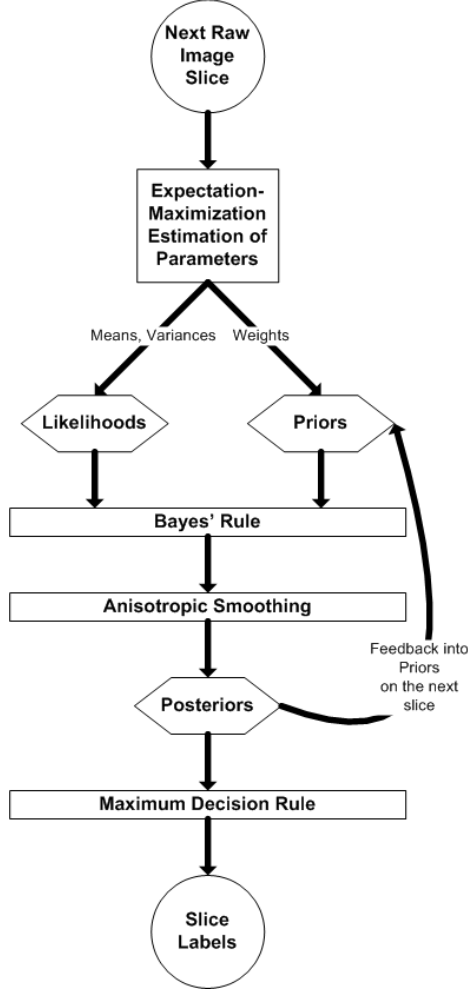


**Figure 26:** Tissue Tracking Algorithm

that there are meaningful data-driven priors one may use in these situations. For instance, in [31] the authors reported success using the previous posteriors as the current priors when classifying a time sequence of SAR images. Our method provides a convenient way for one to combine the posteriors from previous medical image slices, call these  $p_{POST}(C)$ , with the expectation-maximization weights computed from the data, denoted by  $p_{EM}(C)$ , on the current slice to form the prior probabilities on the current slice.

We begin with an intuitive explanation. For a very small slice spacing, we expect a high degree of correlation from one slice to the next and thus would likely benefit

from using the posteriors of the previous slice to guide the choice of priors for the next slice. On the other hand, for a large slice spacing, it is undesirable to use information from previous slices to guide the segmentation of the next slice. In this case, we could set our priors according to the weights derived from the expectation-maximization algorithm. Hence, we use slice spacing, call this  $Z$ , to set the contributions of  $p_{POST}(C)$  and  $p_{EM}(C)$  as follows:

$$p(C) = e^{-Z/\lambda} p_{POST}(C) + (1 - e^{-Z/\lambda}) p_{EM}(C) \quad (22)$$

where  $\lambda$  is a free parameter which allows the user to tune the weights appropriately.

As before, in the last step of the algorithm, the posterior probabilities are smoothed and the MAP decision rule is applied to achieve the final segmentation.

### 5.3 *Experiment*

We have applied this algorithm to 20 normal brain MRI data-sets. We used publicly available data-sets from the Internet Brain Segmentation Repository (IBSR) offered by the Massachusetts General Hospital, Center for Morphometric Analysis [54, 86]. The IBSR data-sets are T1-weighted, 3D coronal brain scans after having been positionally normalized. Manual expert segmentations for these data-sets are publicly available and represent the ground truth used in this work.

Also documented on the IBSR website are the details for a comparison of 6 separate classification algorithms on these 20 datasets. They use an overlap metric for validation known as the Tanimoto coefficient [19] which will be discussed further in Section 5.4. Using the Tanimoto coefficient, Rajapakse *et al.* compared the results of 6 separate algorithms (each operating in the absence of clinical prior information) on the classification of these 20 datasets into gray matter, white matter, and CSF. These 6 algorithms include the following: Adaptive MAP, Biased MAP, Fuzzy C-Means, MAP, Maximum-Likelihood, and Tree-Structure K-Means.

These 20 coronal brain scans are convenient for comparison because they span the spectrum of quality of imagery. The worst cases have low contrast and relatively large intensity gradients. The best cases are more recently acquired and result in better overlap scores.

Our code was written using the Insight Toolkit (ITK) [33]. ITK is quickly becoming the imaging software of choice for researchers in the medical imaging community and all of the functionality needed for this algorithm exists in the latest release of ITK (version 3.0.0). In addition to ITK, we relied heavily upon various tools to perform our experiment, such as 3D Slicer [27] and FreeSurfer [91].

The IBSR data is anisotropic (1mm x 1mm x 3mm), so we set the parameter  $Z = 3$ . We experimented with a variety of settings for the parameter  $\lambda$  and found that the best results were achieved by setting  $\lambda = 3$ . This corresponds to using 36.7% of the neighboring posterior and 63.3% of the EM weights for our prior.

## 5.4 Results

Here we compare the results of our algorithm on the 20 IBSR datasets with the 6 algorithms discussed above in Section 5.3. We validate the results of our algorithm against the expert manual segmentations using the Tanimoto coefficient. The Tanimoto coefficient is defined by  $1 - (n_1 + n_2 - 2n_{12}) / (n_1 + n_2 - n_{12})$  in which  $n_1$  is the number of voxels of a particular class (e.g. the number of voxel of gray matter) in manual result and  $n_2$  is number of voxels of that same class for the algorithm result.  $n_{12}$  represents the number of voxels contained in the intersection of the particular class from manual result and the algorithm result. The metric ranges from 0 to 1 while 1 signifies identical results and 0 indicates poor results. While other popular validation methods exist, such as the DICE measure [118], the Tanimoto metric represents a good measure of overlap and is convenient for comparing against the IBSR results.

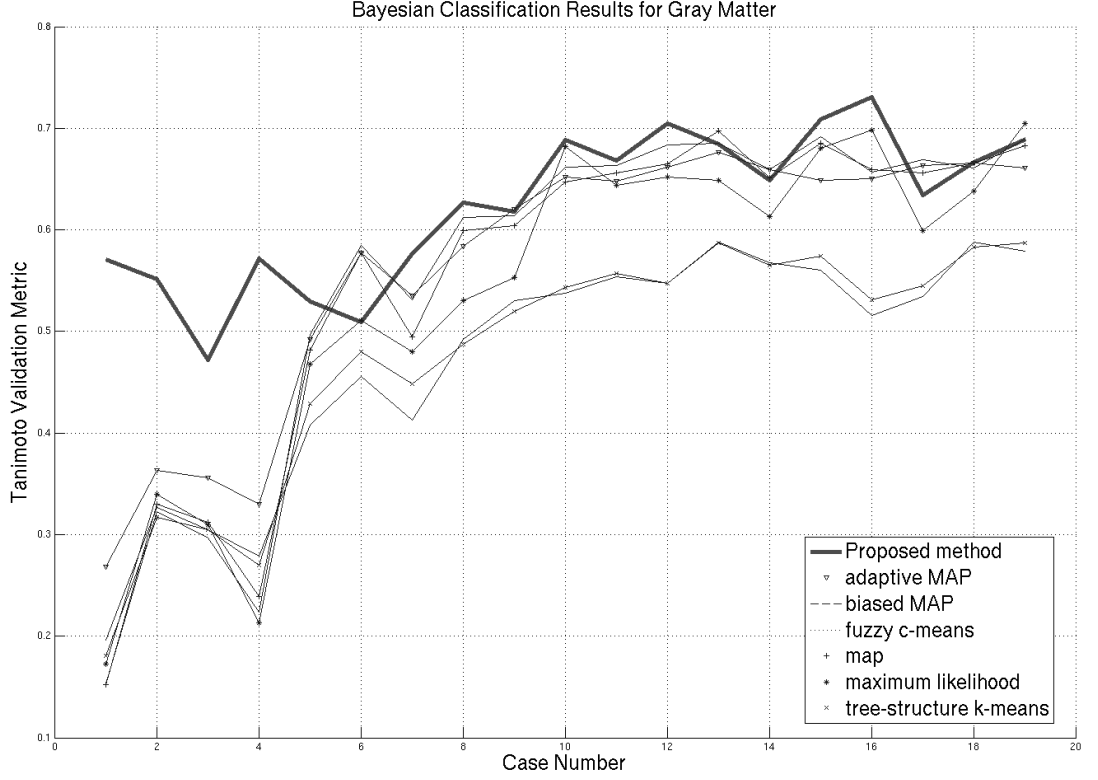


**Figure 27:** Overlap of Gray Voxels for Each Brain Scan

The results of our methods as compared to the 6 other algorithms is shown in Figure 27 for gray matter voxels and in Figure 28 for white matter voxels. As can be seen, our algorithm performs better than the competing algorithms, especially for low quality imagery (note that the cases are ordered from poor quality on the left to high quality on the right).

On average, the tissue tracking algorithm achieves a Tanimoto coefficient of 0.6236 for gray matter compared to 0.5609 for the 3D volumetric version and to 0.5254 for the other methods shown in the plot. Likewise, the tissue tracking algorithm achieves a Tanimoto coefficient of 0.6578 for white matter compared to 0.6039 for the 3D volumetric version and to 0.5580 for the other methods shown in the plot.

In Figures 29, 30, and 31, we show snapshots of our results on various data-sets and slices. In the left column, we show the original grayscale slice. In the middle

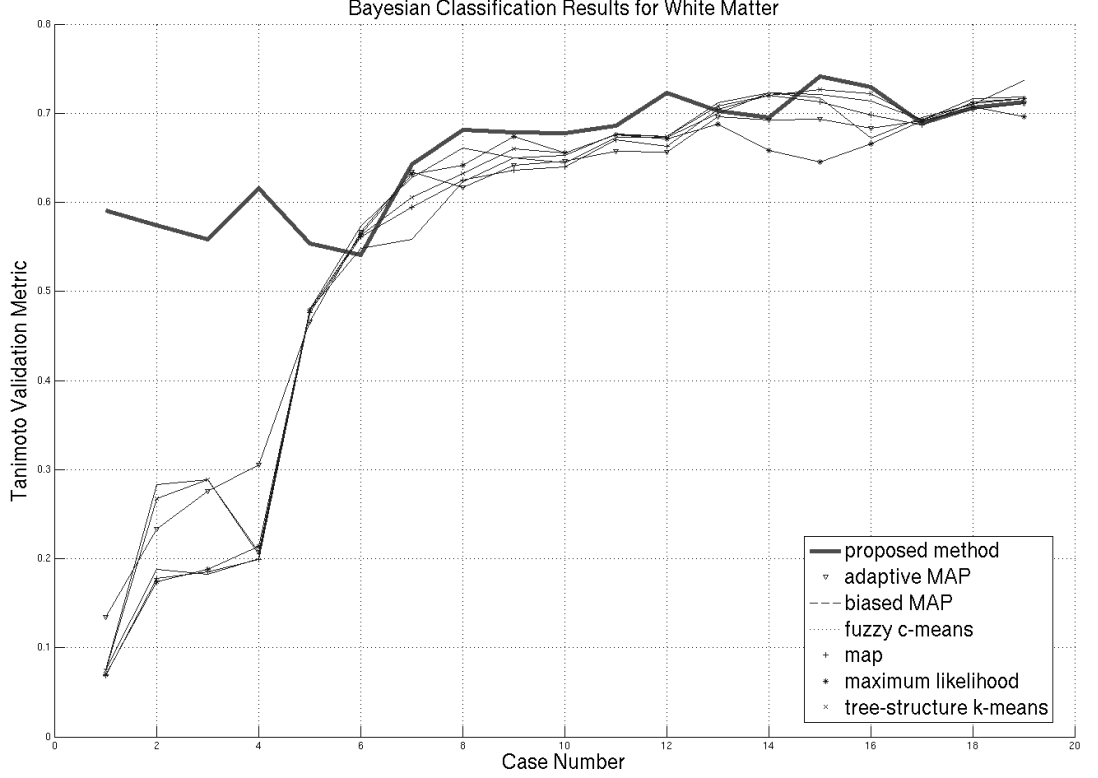


**Figure 28:** Overlap of White Voxels for Each Brain Scan

column, we show the results of our classification algorithm. In the right column, we show the expert manual segmentation results. Note that cases 5-8 and 4-8 were poor quality cases while case 11-3 was a high quality case.

## 5.5 Conclusion

We have presented an algorithm for the Bayesian segmentation of imagery by casting the problem in a tracking framework and using priors derived from the data. Using slice thickness, we have proposed a combination of expectation-maximization weighting and previous posterior updating to construct meaningful priors. The application of this algorithm to brain MRI scans has shown positive results.

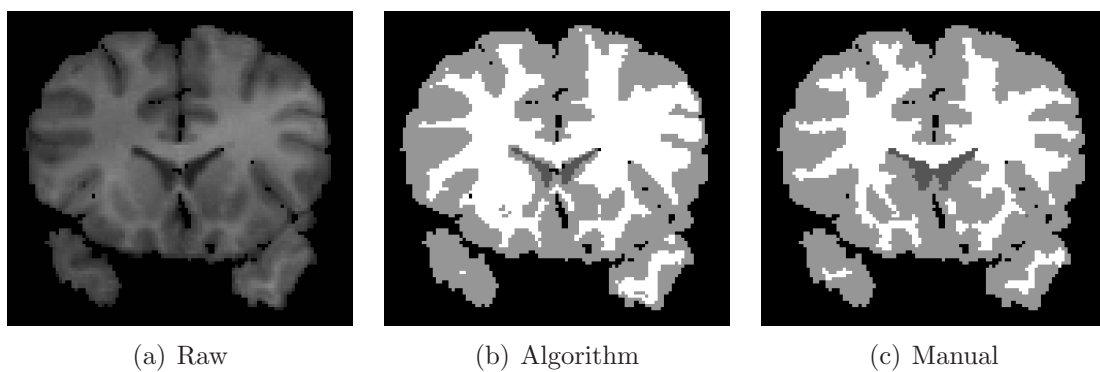


**Figure 29:** Case 5-8, Slice 36

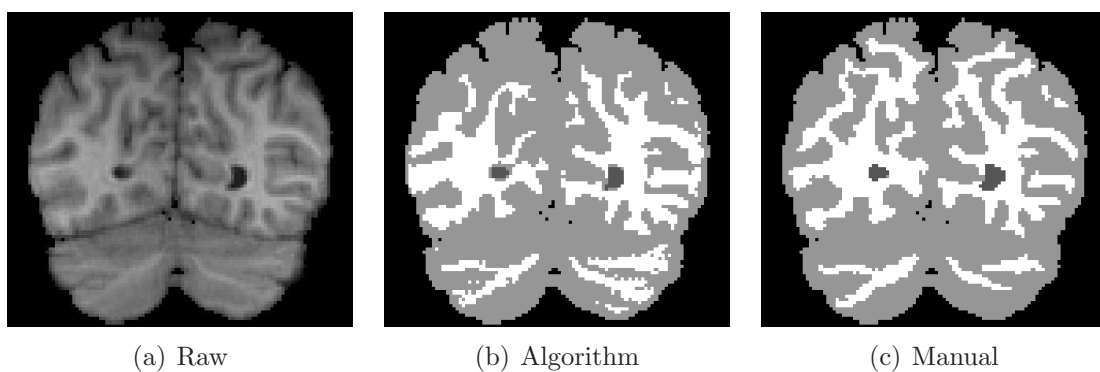


**Figure 30:** Case 4-8, Slice 12

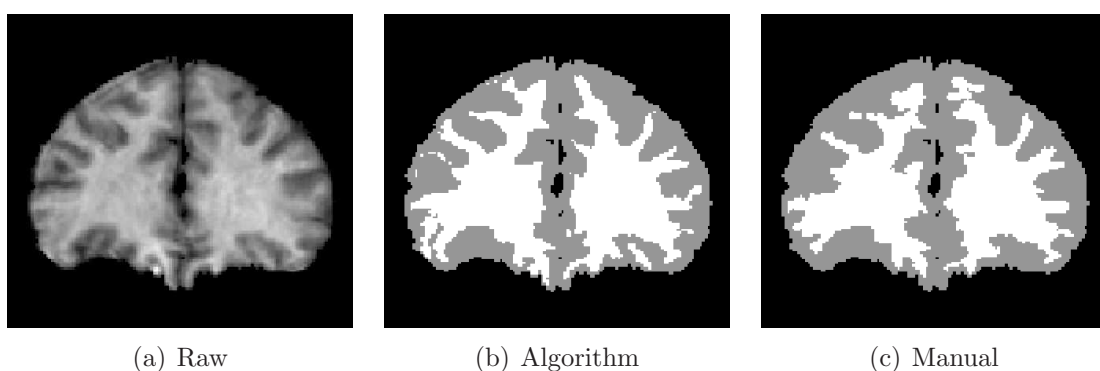


**Figure 31:** Case 11-2, Slice 44

## CHAPTER VI

### BAYESIAN METHODS IN COLON CAD

In this chapter, we present a bayesian probabilistic model for haustral curvatures with applications to colon CAD [56].

#### **6.1 Introduction**

With over half a million obits, colorectal cancer was ranked as the fourth leading cause of cancer death worldwide in 2002 [20], and it is currently ranked as the second leading cause of cancer-related deaths in the United States [35]. Most colorectal cancers arise from benign colonic polyps, and their early detection can significantly increase survival rates [21]. Optical colonoscopy is part of the standard screening protocol for the detection of polyps in the colon [94], but the discomfort and long duration of this procedure has negative impact on patient compliance [32].

Virtual colonoscopy (VC) or computed tomography colonography (CTC) has shown promise as a less invasive method for detecting polyps, with performance at least as good as that of optical colonoscopy [83]. Once computed tomography (CT) imaging and advanced visualization tools were introduced, the natural second step is the use of computer-aided detection (CAD) systems for automating the search for colonic polyps, and a number of CAD techniques have been developed in recent years. Early examples include the work of Yoshida *et al* [116], in which principal curvatures were used to compute a shape index indicative of the roundness of polyps. Curvatures were also used by Vos *et al* [111] and by Summers *et al* [102, 100]. More recently, modeling through spherical harmonics [45], surface normal overlap [75] and other curvature-based methods have been developed [9, 109]. The use of small to moderate [28, 36, 109] and of large [107] feature sets followed by a more sophisticated

classification mechanism have also been explored.

In the list above, curvature and curvature-based measures are the features most commonly used for classification. In particular, [102, 116, 111, 101, 9, 109] built explicit models with different degrees of complexity for the ranges of curvatures observed in colonic polyps, folds, and, occasionally, the haustra (or colon wall) itself. However, whereas folds and polyps are modeled through highly sophisticated schemes, the haustra is either altogether omitted [111, 9, 109] or simply mentioned as a region of low curvature [102, 116]. This chapter introduces a novel model for the haustra. We use the same assumptions as [102, 116] regarding the shape of the haustra, but we augment the model with a component driven by recent results in the theory of Gaussian random fields [60]. This allows for an accurate estimation of the probability distribution of curvatures of isosurfaces of the haustra, which can be naturally fed into any curvature-based CAD system aimed at detecting colonic polyps. Results with real data show the usefulness of the proposed model as applied to colon CAD.

## 6.2 *Shape from Principal Curvatures*

Let the *volume image*  $I$  (henceforth referred to simply as image) be defined as a twice-differentiable mapping from  $\mathcal{V} \subset \mathbb{R}^3$  into  $\mathbb{R}$ . For any given  $c$ , we define an *isosurface*  $M_c \subset \mathcal{V}$  at the *isovalue*  $c$  as the set of points  $\mathbf{x}$  satisfying  $I(\mathbf{x}) = c$  and  $\nabla I(\mathbf{x}) \neq \mathbf{0}$ . The principal curvatures of  $M_c$  at a point  $\mathbf{x}$  are given by the eigenvalues of the matrix  $\tilde{\mathbf{H}} = \mathbf{N}^T \mathbf{H} \mathbf{N} / \|\nabla I\|$  [97, pg. 138], where  $\nabla I$  is the gradient of  $I$ ,  $\mathbf{H}$  is the Hessian of  $I$ , and columns of  $\mathbf{N}$  form an orthonormal basis for the null space of  $\nabla I$ . This computation can be carried out as the concatenation of a linear and a nonlinear step. As shown in Fig. 32, the linear step comprises the computation of the gradient and the Hessian of the image input image. The nonlinear step involves the matrix multiplications of  $\mathbf{H}$  and  $\mathbf{N}$ , the computation of and division by the scalar  $\|\nabla I\|$ , and the actual computation of the eigenvalues of the resulting  $2 \times 2$  matrix.

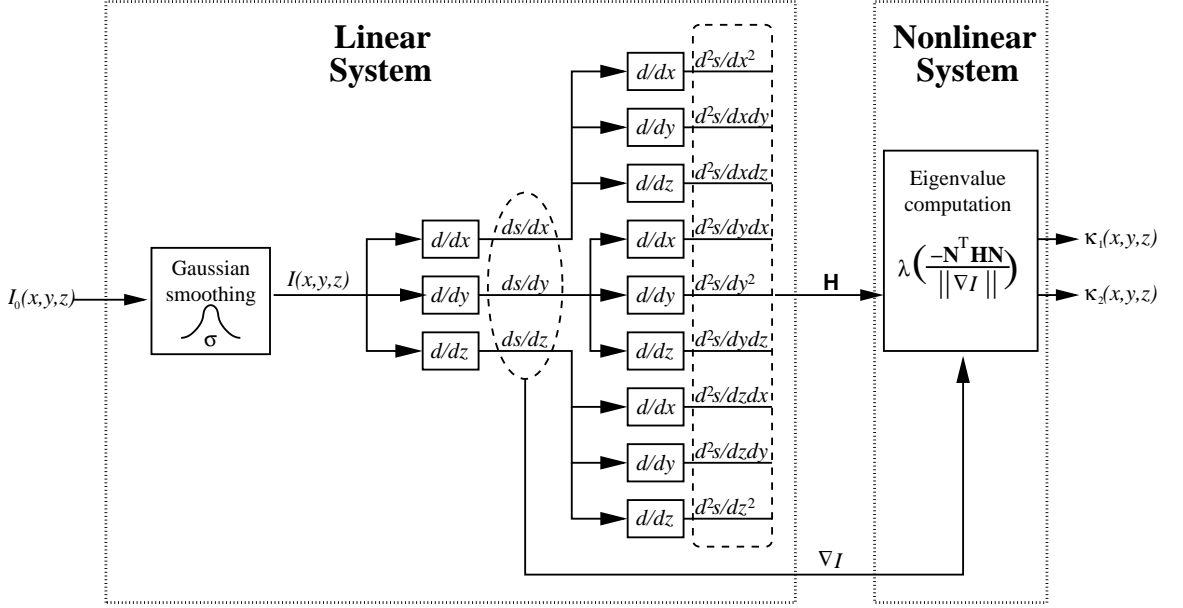


Figure 32: The Curvature Computation System

### 6.2.1 The Geometric Model

In [98], the haustra of the colon is defined as: “the sacculations of the colon, caused by the teniae, or longitudinal bands, which are slightly shorter than the gut so that the latter is thrown into tucks or pouches”. These sacculations are the curved segments of the colon wall. The morphological models in Langer *et al.* [48] justify the adoption by [102, 116] of a low curvature surface representation for the haustra. However, such a model, by itself, is not enough to specify the distribution of curvatures that one expects at the colon wall. In order to achieve this, we consider a volume image  $I_0(\mathbf{x})$  representing any particular low curvature geometric model of the haustra. Now let  $h_0(\mathbf{x})$  be a corruption of  $I_0(\mathbf{x})$  by additive white noise  $\eta_0(\mathbf{x})$ . Following the pipeline described in Fig. 32 with  $h_0(\mathbf{x})$  as the input image, we obtain a smoothed volume  $h(\mathbf{x}) = I(\mathbf{x}) + \eta(\mathbf{x})$ , where  $I(\mathbf{x})$  and  $\eta(\mathbf{x})$  are smooth versions of  $I_0(\mathbf{x})$  and  $\eta_0(\mathbf{x})$ . In particular,  $\eta(\mathbf{x})$  is still Gaussian noise, but no longer white. Assuming that the variance of the input (zero-mean) white noise is  $\sigma_\eta^2$ , the autocorrelation function  $R(\mathbf{x})$  of the filtered noise will be  $R(\mathbf{x}) = \sigma_\eta^2 \exp(-\mathbf{x}^T \mathbf{\Sigma} \mathbf{x}/4)$  [17], where  $\mathbf{\Sigma}$  is the covariance

matrix of the smoothing kernel. For an isotropic kernel, we have  $\Sigma = \sigma^2 \mathbb{I}$ .

Denoting the function that maps a matrix  $\mathbf{A}$  to its eigenvalues by  $\lambda(\mathbf{A})$ , the nonlinear step of the curvature computation yields

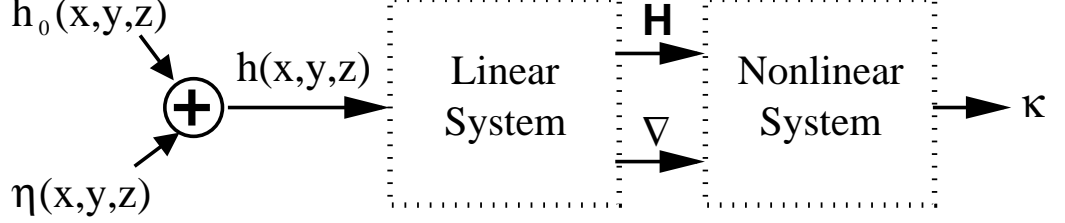


**Figure 33:** *The Haustra Model*

$$\kappa = \lambda\left(\frac{-\mathbf{N}^T \mathbf{H}_h \mathbf{N}}{\|\nabla h\|}\right) = \lambda\left(\frac{-\mathbf{N}^T (\mathbf{H}_I + \mathbf{H}_\eta) \mathbf{N}}{\|\nabla I + \nabla \eta\|}\right), \quad (23)$$

where  $\kappa = (\kappa_1, \kappa_2)$  are the principal curvatures of  $h(\mathbf{x})$  at the point  $\mathbf{x}$ .

### 6.2.2 Distribution of Curvatures

The stochastic differential equation in (23) can be simplified by making reasonable assumptions about the shape and appearance of the haustra as observed in CT images. First, the matrix  $\mathbf{N}^T \mathbf{H}_I \mathbf{N}$  must have, on average, a small Frobenius norm compared to that of  $\mathbf{N}^T \mathbf{H}_\eta \mathbf{N}$ . To demonstrate this, observe that, per the discussion in section 6.2.1, the magnitude of the eigenvalues of  $\mathbf{N}^T \mathbf{H}_I \mathbf{N}$  is small, reflecting the low curvature of the haustra. Since  $\mathbf{N}^T \mathbf{H}_I \mathbf{N}$  is a symmetric matrix, its singular values must also be small. This last observation indicates that a Taylor expansion of (23) around  $\mathbf{N}^T \mathbf{H}_I \mathbf{N} = \mathbf{0}$  yields a good approximation for  $\kappa$ , i.e.,

$$\kappa \approx \lambda\left(\frac{-\mathbf{N}^T (\mathbf{H}_\eta) \mathbf{N}}{\|\nabla I + \nabla \eta\|}\right) + \text{vec}(\mathbf{N}^T \mathbf{H}_I \mathbf{N})^T \frac{\partial \kappa}{\partial \text{vec}(\mathbf{N}^T \mathbf{H}_I \mathbf{N})^T} \Big|_{\mathbf{H}_I=0} \quad (24)$$

$$\approx \lambda\left(\frac{-\mathbf{N}^T (\mathbf{H}_\eta) \mathbf{N}}{\|\nabla I + \nabla \eta\|}\right) + \lambda\left(\frac{-\mathbf{N}^T \mathbf{H}_I \mathbf{N}}{\|\nabla I + \nabla \eta\|}\right), \quad (25)$$

where  $\text{vec}(\mathbf{A})$  indicates the vector built out the matrix  $\mathbf{A}$  by stacking its columns. Indicating the Kronecker product by  $\otimes$  and the  $i$ -th eigenvalue of the (symmetric) matrix  $\mathbf{A}$  by  $\lambda_i$ , the equality of (24) and (25) can be verified by using the relations

$\text{vec}(ABC) = (C^T \otimes A) \text{vec}(B)$  and  $\partial \lambda_i(\mathbf{A}) / \partial \text{vec}(\mathbf{A})^T = \mathbf{v}_i \otimes \mathbf{v}_i$ , where  $\mathbf{v}_i$  is the eigenvector associated to  $\lambda_i$  [53].

We further simplify (23) by assuming that the magnitude of  $\nabla I$  is, on average, large compared to that of  $\nabla \eta$ . This assumption simply reflects the fact that the haustra corresponds to a sharp interface between air and soft tissue. Hence, (23) becomes,

$$\boldsymbol{\kappa} \approx \frac{\boldsymbol{\lambda}(\mathbf{N}^T \mathbf{H}_\eta \mathbf{N})}{\|\nabla I\|} + \boldsymbol{\kappa}_0, \quad (26)$$

where  $\boldsymbol{\kappa}_0 = \boldsymbol{\lambda}\left(\frac{-\mathbf{N}^T \mathbf{H}_I \mathbf{N}}{\|\nabla I + \nabla \eta\|}\right)$ . Note that  $\boldsymbol{\kappa}$  is a random variable, and, from (26), we can see that its probability density  $p(\boldsymbol{\kappa})$  is given by

$$p(\boldsymbol{\kappa}) = p_{\boldsymbol{\lambda}_\eta}((\boldsymbol{\kappa} - \boldsymbol{\kappa}_0)\|\nabla I\|)\|\nabla I\|^2, \quad (27)$$

where  $p_{\boldsymbol{\lambda}_\eta}$  is the probability density of the random variable  $\boldsymbol{\lambda}_\eta = \boldsymbol{\lambda}(\mathbf{N}^T \mathbf{H}_\eta \mathbf{N})$ .

In order to derive  $p(\boldsymbol{\kappa})$  we adapt recent results in the theory of Gaussian random fields [60], which establish that  $\boldsymbol{\lambda}_\eta$  is distributed according to a linear combination of Gaussian and chi-distributed independent random variables. More precisely, for an isotropic smoothing kernel with covariance matrix  $\boldsymbol{\Sigma} = \sigma^2 \mathbb{I}$ ,  $\boldsymbol{\lambda}_\eta \sim \alpha' [N(0, 2) \mp \mathcal{X}(2)]$ , with  $\alpha' = \sigma_\eta / (2\sigma^2)$ , resulting in

$$\begin{aligned} p_{\boldsymbol{\lambda}_\eta}(\boldsymbol{\lambda}) &= \frac{1}{2\alpha'^2} p_{N(0,2)}((\lambda_2 + \lambda_1)/(2\alpha')) p_{\mathcal{X}(2)}((\lambda_2 - \lambda_1)/(2\alpha')) \\ &= \frac{1}{8\sqrt{2\pi}\alpha'^3} (\lambda_2 - \lambda_1) e^{-\frac{5\lambda_1^2 - 6\lambda_2\lambda_1 + 5\lambda_2^2}{32\alpha'^2}} \end{aligned} \quad (28)$$

Assuming a simple spherical model of radius  $R$  for the input image  $I$ , we have  $\boldsymbol{\kappa}_0 = (-1/R, -1/R)$ . Therefore, the final probability distribution of the haustral curvatures is given by

$$p(\boldsymbol{\kappa}) = \frac{1}{8\sqrt{2\pi}\alpha^3} (\kappa_2 - \kappa_1) e^{-\frac{(5\kappa_1^2 - 6\kappa_2\kappa_1 + 5\kappa_2^2)R^2 + 4(\kappa_1 + \kappa_2)R + 4}{32R^2\alpha^2}}, \quad (29)$$

with  $\alpha = \sigma_\eta / (2\sigma^2 \|\nabla I\|)$ .

### 6.3 Experiments and Results

As a first step to demonstrate the usefulness of the proposed model we captured principal curvature data from random samples of pedunculated, sessile and flat polyps, haustral folds, and haustra. In Fig. 34, we display this scatter data over the decision boundaries generated from our haustra model (yellow) and models for pedunculated (red), sessile and flat polyp (green), and haustral fold (blue), described in [9]. The overlaid yellow scatter data points provide visual validation for the haustra model decision boundary, as shown in Fig. 34(a). In Fig. 34(b), we show the decision boundaries obtained by considering only two model categories: for (polyps) and against (haustra and folds).

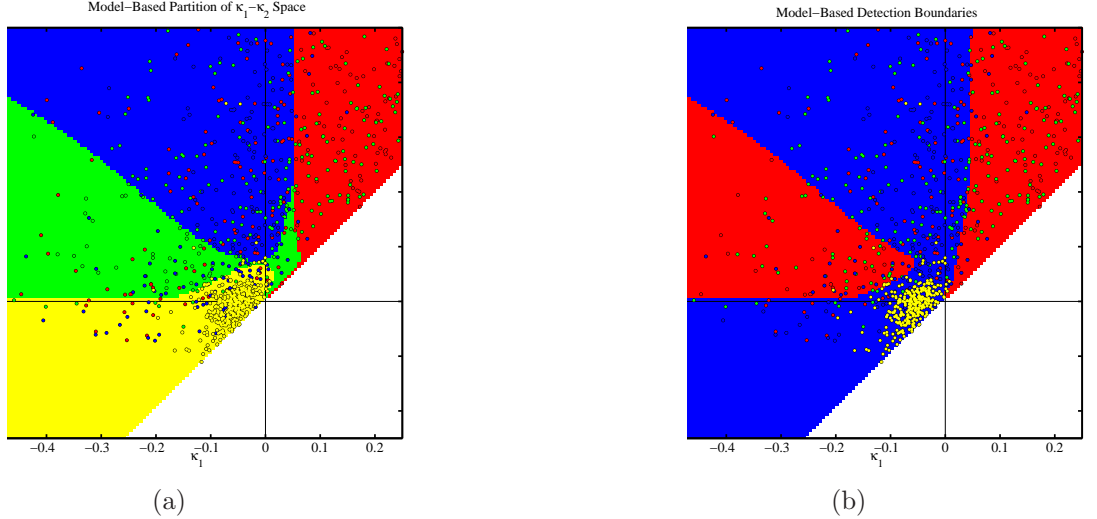


**Figure 34: Partitioning of  $\kappa_1$ - $\kappa_2$  space with overlying scatter plot data:** (a) Model-based partitioning of  $\kappa_1$ - $\kappa_2$  space, red = pedunculated polyps, green = sessile and flat polyps, blue = haustral folds, yellow = haustra, (b) Binary partitioning of  $\kappa_1$ - $\kappa_2$  space, red = polyp responses, blue = non-polyp responses

In Fig. 35, we provide another depiction of the benefit derived from the addition of the haustra model to the colon CAD system. Figure 35(d) shows an image region centered at an actual polyp. Figure 35(a) shows the result of a Bayesian competition [42] between the combined polyp model (pedunculated, sessile and flat) against the fold model, without inclusion of the haustra model in the same region. The strongest

responses (magenta) are indeed in the polyp, but there are weaker responses (blue) scattered all around the colon wall. Even though most of those can be discarded through thresholding, such a “clean-up” algorithm can remove true positive detections. Figure 35(b) shows the same region as in Fig. 35(a), but now with the haustra model included. The haustra model clearly plays a significant role in reducing the polyp responses on the haustra without affecting the response at the polyp itself. In effect, the haustra model eliminates many potential false positives. In Fig. 35(c) we see the haustra responses alone, obtained by competing the haustra against all the other models, and the reason for the differences between Fig. 35(a) and Fig. 35(b) become clear.

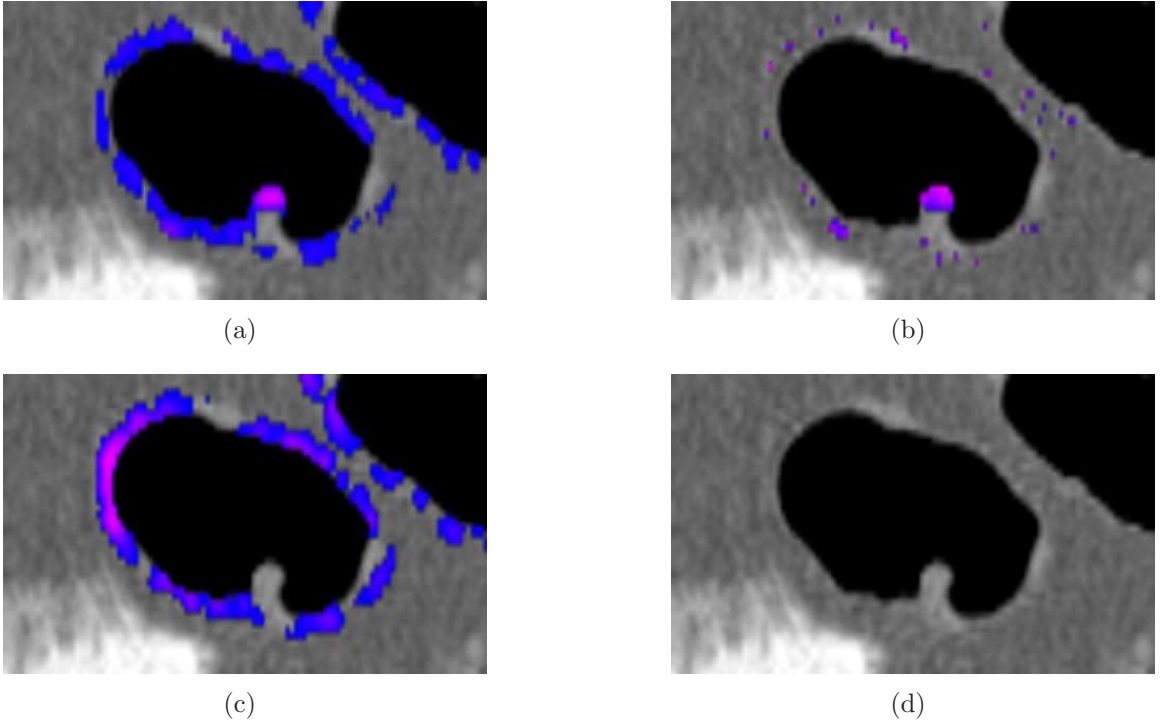


**Figure 35: Visual Haustra Results:** (a) *polyp responses without the haustra model in a window centered at an actual polyp*, (b) *polyp responses with the haustra model*, (c) *haustra responses alone*, and (d) *Raw image data*

Finally, we show the application of our model to a the colon CAD system described in [9]. The test data consisted of a subset of 36 CT volumes from the WRAMC

dataset, from which 23 polyps with diameter above 6 mm were marked by expert radiologists and confirmed by optical colonoscopy.<sup>1</sup> The protocol for patient preparation consisted of oral administration of 90 ml of sodium phosphate and 10 mg of bisacodyl, with a clear-liquid diet that included 500 ml of barium for stool tagging and 120 ml of diatrizoate meglumine and diatrizoate sodium for fluid tagging [83]. The complete WRAMC dataset comprises many more images, but unfortunately ground truth is provided as a distance from the rectum along the colon centerline only, and the precise image location of polyps in this dataset must still be carried out by an expert.

It is important to note that this dataset is significantly more challenging to CAD than the “fully prepped” data commonly used throughout the literature (e.g., all of the CAD work mentioned in the introduction with the exception of the work of Summers *et al*, such as in [101]). However, if the use of CTC demands full cleansing of the colon, patient compliance may still be an issue, since the strongest factor affecting acceptance of colonoscopy is the extent of bowel preparation [32]. Minimally invasive protocols such as the one applied to the collection of the WRAMC data mitigate this problem [49], but pose new difficulties for the interpretation of the images [21]. In Fig. 36, we present a free-response receiver operating characteristic (FROC) curve demonstrating the performance of a lung CAD system that makes use of the proposed haustra model. A sensitivity of 83% is achieved at a cost of 6.2 false positive detections per case, and running time is in the order of 10 min for a  $512 \times 512 \times 700$ -voxel CT volume with a research prototype implemented with ITK.

## 6.4 Conclusions and Future Work

In this work, we have introduced a novel probabilistic model for the curvature of isosurfaces of the haustra. An expression of the probability density function of such

---

<sup>1</sup>This data has been provided courtesy of Dr. Richard Choi, Virtual Colonoscopy Center, Walter Reed Army Medical Center.

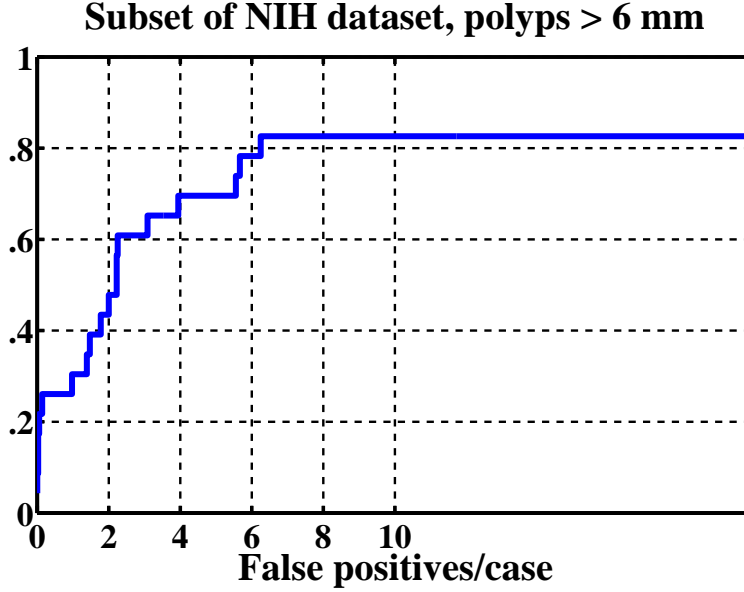


**Figure 36:** *FROC curve for the performance of a colon CAD system using the proposed haustra model. A sensitivity of 83% is achieved at a cost of 6.25 false positive detections per case.*

curvatures was provided by considering Gaussian random perturbation to a geometric abstraction of the colon wall. The model augments the set of models developed in [9] for applications in colon CAD, and was demonstrated in a specific colon CAD application.

In the current formulation the radius  $R$  of the haustra is a fixed parameter representative of the expected radius of the insufflated colon. However, we could account for colonic haustra variations in size and shape by marginalizing over the parameter  $R$ . The prior for this marginalization will depend upon either training data or prior clinical knowledge of insufflated haustra radii. In [61] we have shown how to compute the probability distribution of curvatures for a class of ellipsoidal surfaces, suggesting a mechanism to achieve such generalization.

An interesting debate is presented in [67], which, although in the context of lung CAD, is relevant to this work. From that discussion it is clear that many radiologists see CAD not necessarily as a tool to improve upon the performance of the best radiologists, but as a means to standardize or regularize results of radiologists with

varying degrees of experience. To validate such expectation, however, it is necessary to have data read by multiple radiologists, which is not the case with the WRAMC data set.

## CHAPTER VII

### CONCLUSION

In this dissertation , we presented our approach for geodesic tractography segmentation, a two component approach for the analysis of imagery in oriented domains, with emphasis on the application to DW-MRI. This work is currently being integrated into Slicer3, a part of the NA-MIC toolkit (see <http://www.na-mic.org>). In Figure 37, we show our initial work in integrating this framework.

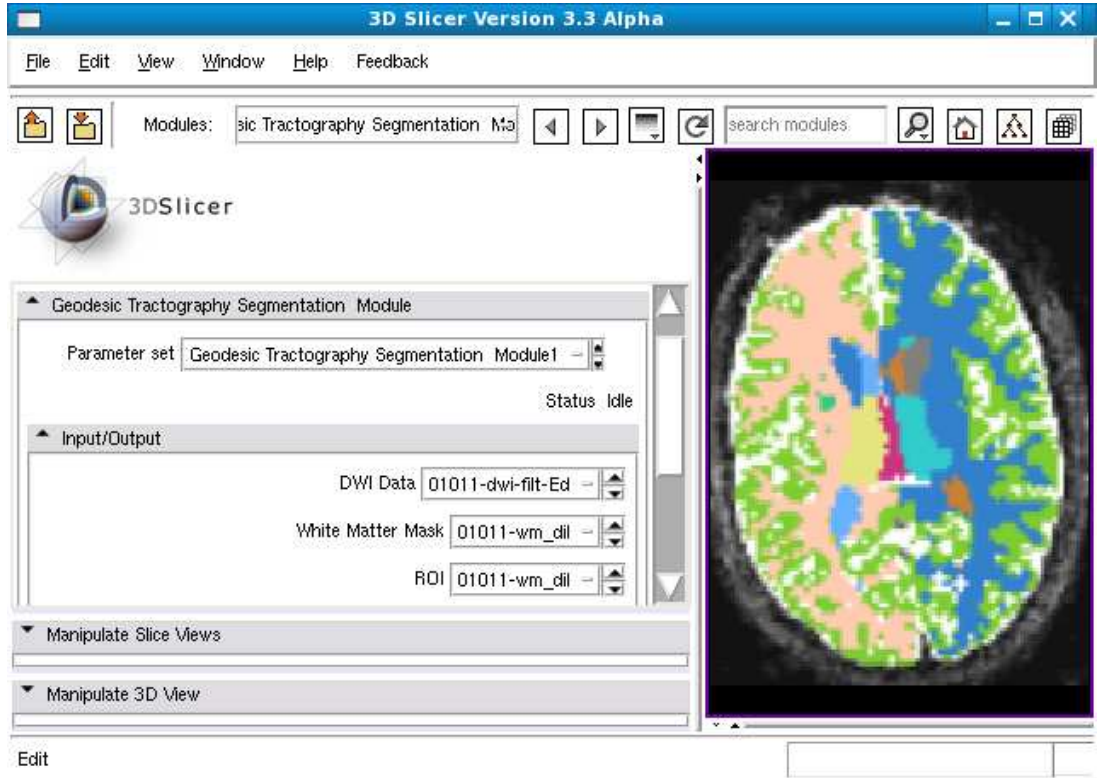


**Figure 37:** Slicer3 Integration. The Geodesic Tractography Segmentation module. Currently under development.

This Slicer3 module is an ideal way for the work in this thesis to be disseminated. We encouraged the interested reader to explore concepts in this thesis by using this

Slicer3 module. This tool in conjunction with other tools is helpful in processing DW-MRI images. It provides an easy-to-use extraction of optimal paths between two regions of interest along with a volumetric segmentation of the associated fiber bundles. Using these features, further population studies may be conducted to compare various metrics across many patients, leading to greater clinical understanding.

## APPENDIX A

### FINSLER FOR NON-CONVEX FUNCTIONS

As we noted above, there may be problems in the non-convex case for our directional segmentation scheme. Nevertheless as we will indicate in this appendix the fast-sweeping type numerical approach will automatically capture an approximation for the convexification of the functional (in the sense to be made precise below.) We abstract the situation to be studied as follows.

Let  $\psi : S^{n-1} \rightarrow \mathbf{R}$  be a function and suppose one defines the *cost of a curve*  $\Gamma$  to be

$$C(\Gamma) = \int_{\Gamma} \psi(\mathbf{T}) \, ds.$$

Define  $F : \mathbf{R}^n \rightarrow \mathbf{R}$  to be the homogeneous extension of degree one of  $\psi$ , so

$$F(v) = |v| \, \psi\left(\frac{v}{|v|}\right).$$

This function need not be convex. We define its convex hull to be

$$\tilde{F}(v) = \sup\{a \cdot v + b : a \in \mathbf{R}^n, b \in \mathbf{R}, \forall_x a \cdot x + b \leq F(x)\}. \quad (30)$$

Furthermore we define

$$E = \{v \in \mathbf{R}^n : F(v) = \tilde{F}(v)\}.$$

This is the set of *extreme points*.

The cost  $C(\Gamma)$  of any parameterized curve  $\Gamma : [0, 1] \rightarrow \mathbf{R}^n$  is given by

$$C(\Gamma) = \int_0^1 F(\Gamma'(\xi)) \, d\xi \quad (31)$$

One can also define the *relaxed cost* as

$$\tilde{C}(\Gamma) = \int_0^1 \tilde{F}(\Gamma'(\xi)) \, d\xi. \quad (32)$$

Clearly one always has

$$\tilde{C}(\Gamma) \leq C(\Gamma) \quad (33)$$

since  $\tilde{F}(v) \leq F(v)$  for all  $v \in \mathbf{R}^n$ .

For any given set  $\Sigma \subset \mathbf{R}^n$  and point  $p \in \mathbf{R}^n \setminus \Sigma$  one defines the cost to get to  $\Sigma$  from  $p$  as

$$C_*(p) = \inf \{ C(\Gamma) : \Gamma(0) = p, \Gamma(1) \in \Sigma \} \quad (34)$$

Here the infimum is taken over all curves from  $p$  to some point in  $\Sigma$ .

One can also define

$$\tilde{C}_*(p) = \inf \{ \tilde{C}(\Gamma) : \Gamma(0) = p, \Gamma(1) \in \Sigma \}, \quad (35)$$

where the infimum is again taken over all curves from  $p$  to some point in  $\Sigma$ .

**LEMMA 2.** *For any curve  $\Gamma : [0, 1] \rightarrow \mathbf{R}^n$  and any  $\varepsilon > 0$  there exists a piecewise linear curve  $\tilde{\Gamma} : [0, 1] \rightarrow \mathbf{R}^n$  with the same endpoints for which one has*

$$C(\tilde{\Gamma}) = \tilde{C}(\tilde{\Gamma}) \leq \tilde{C}(\Gamma) + \varepsilon.$$

This lemma says that any curve from  $p$  to  $\Sigma$  can be replaced by a curve with the same endpoints whose velocities are extreme points for  $F$  (i.e.  $\tilde{F}(\Gamma'(\xi)) = F(\Gamma'(\xi))$  for all  $\xi$ ), without increasing the cost by more than  $\varepsilon$ .

An immediate consequence of the lemma is:

**LEMMA 3.**  $\tilde{C}_*(p) = C_*(p)$ .

It follows that any (correct) method which computes  $C_*$  by propagating the front  $\partial\Sigma$  outwards with velocities given by  $F$  will actually compute  $\tilde{C}_*$ .

*Proof of Lemma 2.* First, it is clear that one can approximate the given curve  $\Gamma$  by a piecewise linear (PL) curve  $\Gamma_1$  for which  $\tilde{F}(\Gamma'_1(\xi)) \leq \tilde{F}(\Gamma'(\xi)) + \varepsilon$  holds for  $0 \leq \xi \leq 1$ . Thus  $\tilde{C}(\Gamma_1) \leq \tilde{C}(\Gamma) + \varepsilon$ .

Next, the PL curve  $\Gamma_1$  is linear (i.e.  $\Gamma'_1(\xi)$  is constant) on each interval  $(\xi_{i-1}, \xi_i)$  from some partition  $0 = \xi_0 < \xi_1 < \dots < \xi_n = 1$ . Let  $v_i$  be the constant value of  $\Gamma'_1$  on  $(\xi_{i-1}, \xi_i)$ . If  $v_i \notin E$  (recall that  $E$  is the set of extreme points), then  $v_i$  is a convex combination of certain  $\tilde{v}_i^1, \dots, \tilde{v}_i^n \in E$ , i.e.,

$$v_i = \alpha_1 \tilde{v}_i^1 + \dots + \alpha_n \tilde{v}_i^n, \quad \alpha_i \geq 0, \quad \sum \alpha_i = 1, \quad (36)$$

while

$$\tilde{F}(v_i) = \alpha_1 \tilde{F}(\tilde{v}_i^1) + \dots + \alpha_n \tilde{F}(\tilde{v}_i^n). \quad (37)$$

Now define a PL curve  $\Gamma_2$  which has

$$\Gamma'_2(\xi) = v_i^k \text{ for } \xi \in (\xi_i^{j-1}, \xi_i^j) \quad (38)$$

where  $\xi_i^j = \xi_{i-1} + \alpha_j(\xi_i - \xi_{i-1})$ . Thus we replace the segments of  $\Gamma_1$  whose velocity are not in the extreme set  $E$  of the function by PL zigzag curves with the same begin and end points whose velocities are in  $E$ .

With this definition one has

$$\Gamma_2(\xi_i) - \Gamma_2(\xi_{i-1}) = \Gamma_1(\xi_i) - \Gamma_1(\xi_{i-1})$$

Hence, if one sets  $\Gamma_2(0) = \Gamma_1(0) = p$ , then one ends up with  $\Gamma_2(1) = \Gamma_1(1) \in \Sigma$ .

Using (37) one can easily see that  $\tilde{C}(\Gamma_2) = \tilde{C}(\Gamma_1)$ . Since  $\Gamma'_2(\xi) \in E$  for all  $\xi$  one also has  $C(\Gamma_2) = \tilde{C}(\Gamma_2)$ . Hence  $\Gamma_2$  is a curve from  $p$  to  $\Sigma$  with  $C(\Gamma_2) \leq \tilde{C}(\Gamma) + \varepsilon$ .  $\square$

## APPENDIX B

### FINSLER FLOW IN TERMS OF $F$

In this appendix, we describe the Finsler flow in terms of the homogeneous extension  $F$  and derive some of its properties.

#### B.0.1 First variation using $F$

Instead of writing  $L(\Gamma)$  in terms of  $\psi$ , we can also write  $L(\Gamma)$  as in (4). The first variation is then given by the usual Euler-Lagrange equation

$$\frac{d}{dt}L(\Gamma) = \int_0^1 \{F_p - (F_v)_x\} \cdot \Gamma_t \, dx. \quad (39)$$

If one looks for a normal evolution equation (i.e.  $\Gamma_t \perp \Gamma_x$ ) then one is led to an equation of the form

$$\beta \Gamma_t = \{(F_v)_x - F_p\}^\perp$$

for some positive scalar  $\beta$ . If one additionally wants the equation to be invariant under reparametrization, then the only possible choice for  $\beta$  is  $\beta = G(\Gamma, \Gamma_x)$  in which  $G(p, v)$  is positively homogeneous of degree one in  $v \in \mathbf{R}^n$ . A possible choice would be  $G(\Gamma, \Gamma_x) = |\Gamma_x|$ , which leads us to the evolution equation

$$\Gamma_t = \frac{1}{|\Gamma_x|} \{(F_v)_x - F_p\}^\perp. \quad (40)$$

This equation is equivalent with (5).

One could also choose  $G(p, v) = F(p, v)$  which would result in

$$\Gamma_t = \frac{1}{F(\Gamma, \Gamma_x)} \{(F_v)_x - F_p\}^\perp.$$

### B.0.2 Some identities involving $F$

Since  $F(p, tv) = tF(p, v)$  for all  $t \geq 0$  one has

$$F_v(p, tv) = F_v(p, v) \quad (\forall t > 0) \quad (41)$$

$$F_v(p, v) \cdot v = 0 \quad (42)$$

For the second derivative  $F_{vv}(p, v)$ , which we regard as a symmetric linear transformation on  $\mathbf{R}^n$ , this implies that

$$F_{vv}(p, v) \cdot v = 0, \quad (43)$$

and hence,

$$F_{vv}(p, v) \cdot w \perp v \quad (\forall w \in \mathbf{R}^n). \quad (44)$$

We may also regard  $F_{vp}(p, v)$  as a linear transformation on  $\mathbf{R}^n$ , and in this case we have

$$\{v \cdot F_{vp}(p, v) - F_p(p, v)\} \perp v. \quad (45)$$

Indeed, in tensor notation this amounts to

$$v_i F_{p_i v_j}(p, v) v_j = F_{p_i}(p, v) v_i$$

which one obtains by differentiating the Euler identity

$$F_{v_i}(p, v) v_i = F(p, v)$$

with respect to  $p$  in the direction of  $v$ .

### B.0.3 Steepest descent with $F$

We continue with equation (40)

$$|\Gamma_x| \Gamma_t = \{F_{vv}(\Gamma, \Gamma_x) \Gamma_{xx} + \Gamma_x \cdot F_{pv}(\Gamma, \Gamma_x) - F_p(\Gamma, \Gamma_x)\}^\perp.$$

By (44) the combined terms on the right are already perpendicular to  $\Gamma_x$ . We therefore find that (40) is equivalent with

$$\Gamma_t = \frac{1}{|\Gamma_x|} \{F_{vv}(\Gamma, \Gamma_x) \cdot \Gamma_{xx} + \Gamma_x \cdot F_{pv}(\Gamma, \Gamma_x) - F_p(\Gamma, \Gamma_x)\} \quad (46)$$

More generally, one gets the equation

$$\Gamma_t = \frac{1}{G(\Gamma, \Gamma_x)} \{F_{vv}(\Gamma, \Gamma_x) \cdot \Gamma_{xx} + \Gamma_x \cdot F_{pv}(\Gamma, \Gamma_x) - F_p(\Gamma, \Gamma_x)\} \quad (47)$$

No matter which  $G$  one chooses, this equation fails to be parabolic since  $F_{vv}$  always has a zero eigenvalue, namely  $F_{vv}(p, v)v = 0$ .

#### B.0.4 Parabolic equation

The right hand side in (47) is invariant under reparametrizations, i.e. if  $\Gamma(x, t) = \gamma(y(x, t), t)$ , then  $\gamma$  satisfies

$$\gamma_t = \frac{1}{G(\gamma, \gamma_y)} F_{vv}(\gamma, \gamma_y) \gamma_{yy} + y_t \gamma_y.$$

Choose the parametrization so that

$$y_t(x, t) = [\alpha[\gamma](\gamma_y \cdot \gamma_{yy}) \gamma_y]_{y=y(x, t)}$$

for some scalar  $\alpha > 0$  which can depend on  $\Gamma$  and  $\Gamma_y$ .

The resulting equation for  $\gamma$  is then

$$\gamma_t = \left\{ \frac{F_{vv}(\gamma, \gamma_y)}{G(\gamma, \gamma_y)} + \alpha \gamma_y \otimes \gamma_y \right\} \cdot \gamma_{yy} + \frac{B(\gamma, \gamma_y)}{G(\gamma, \gamma_y)} \quad (48)$$

where by definition

$$B(p, v) = v \cdot F_{pv}(p, v) - F_p(p, v).$$

As long as one chooses  $\alpha(\gamma, \gamma_y) > 0$ , and as long as  $F_{vv}$  is positive definite on  $\{v\}^\perp$ , this equation is strictly parabolic. A particular choice for  $G$  and  $\alpha$  would be

$$G = |\gamma_y|, \quad \alpha = |\gamma_y|^{-2},$$

which leads to

$$\Gamma_t = \{F_{vv}(\gamma, \mathbf{T}) + \mathbf{T} \otimes \mathbf{T}\} \cdot \frac{\gamma_{yy}}{|\gamma_y|^2} + B(\gamma, \mathbf{T}) \quad (49)$$

where  $\mathbf{T} = \gamma_y/|\gamma_y|$  is the unit tangent vector.

### B.0.5 Numerical scheme

We should note that using the above a simple approach can be employed to equation (49). For completeness, we sketch this here.

We set

$$\gamma(j\Delta x, k\Delta t) = \gamma_j^k,$$

and discretize (49) as follows

$$\frac{\gamma_j^{k+1} - \gamma_j^k}{\Delta t} = A_j^k \{ \gamma_{j+1}^{k+1} - 2\gamma_j^{k+1} + \gamma_{j-1}^{k+1} \} + B_j^k \quad (50)$$

in which the  $n \times n$  matrices  $A_j^k$  are defined by

$$A_j^k = 4 \frac{F_{vv}(\gamma_j^k, \mathbf{T}_j^k) + \mathbf{T}_j^k \otimes \mathbf{T}_j^k}{|\gamma_{j+1}^k - \gamma_{j-1}^k|^2}$$

and one could define the unit tangents  $\mathbf{T}_j^k$  by

$$\mathbf{T}_j^k = \frac{\gamma_{j+1}^k - \gamma_{j-1}^k}{|\gamma_{j+1}^k - \gamma_{j-1}^k|}.$$

The vectors  $B_j^k$  could be discretized by

$$B_j^k = \mathbf{T}_j^k \cdot F_{pv}(\gamma_j^k, \mathbf{T}_j^k) - F_p(\gamma_j^k, \mathbf{T}_j^k).$$

The system of equations (50) is tridiagonal vector valued system of equations. If one puts the components of each vector  $\gamma_j^k$  in one long vector, then (50) can be written as a finite band system of equations, which can be solved very efficiently ( $O(n)$  operations per time step).

## REFERENCES

- [1] ALEXANDER, D., GEE, J., and BAJCSY, R., “Similarity measures for matching diffusion tensor images,” in *Proceedings of the British Machine Vision Conference (BMVC)*, 1999.
- [2] ANGENENT, S. and GURTIN, M., “Anisotropic motion of a phase interface. well-posedness of the initial value problem and qualitative properties of the interface,” *J. Reine Angew. Math.*, vol. 446, pp. 1–47, 1994.
- [3] ANGENENT, S., “Parabolic equations for curves on surfaces. II. Intersections, blow-up and generalized solutions,” *Ann. of Math. (2)*, vol. 133, no. 1, pp. 171–215, 1991.
- [4] BAO, D., CHERN, S.-S., and SHEN, Z., *Introduction to Riemann-Finsler Geometry*. Springer, 2000.
- [5] BASSER, P., MATTIELLO, J., and LEBIHAN, D., “MR diffusion tensor spectroscopy and imaging,” *Biophys. J.*, vol. 66, pp. 259–267, 1994.
- [6] BASSER, P., PAJEVIC, S., PIERPAOLI, C., DUDA, J., and ALDROUBI, A., “In vivo fiber tractography using DT-MRI data,” *Magnetic Resonance in Medicine*, vol. 44, no. 4, pp. 625–632, 2000.
- [7] BASSER, P. and PIERPAOLI, C., “Microstructural and physiological features of tissues elucidated by quantitative-diffusion-tensor MRI,” *J Magn Reson B*, vol. 111, no. 3, pp. 209–219, 1996.
- [8] BELLETTINI, G., *A Sampler of Riemann-Finsler Geometry*, ch. Anisotropic and crystalline mean curvature flow, pp. 49–82. Cambridge University Press, 2004.
- [9] BHOTIKA, R., MENDONÇA, P. R. S., SIROHEY, S. A., TURNER, W. D., LEE, Y.-L., MCCOY, J. M., BROWN, R. E. B., and MILLER, J. V., “Part-based local shape models for colon polyp detection,” in *Medical Image Computing and Computer-Assisted Intervention*, (Copenhagen, Denmark), pp. 479–486, Oct. 2006.
- [10] BILMES, J., “A Gentle Tutorial of the EM Algorithm and its Application to Parameter Estimation for Gaussian Mixture and Hidden Markov Models,” *manuscript, International Computer Science Institute*, 1998.
- [11] BOYKOV, Y. and KOLMORGOROV, V., “Computing geodesics and minimal surfaces via graph cuts,” in *Proceedings IEEE International Conference Computer Vision*, pp. 26–33, 2003.

- [12] BOYKOV, Y., KOLMORGOROV, V., CREMERS, D., and DELONG, A., “An integral solution to surface evolution pdes via geo-cuts,” in *Proceedings IEEE European Conference Computer Vision*, pp. 409–422, 2006.
- [13] CAMPBELL, J. S., *Diffusion Imaging of White Matter Fibre Tracts*. PhD thesis, McGill University, 2004.
- [14] CASELLES, V., KIMMEL, R., and SAPIRO, G., “Geodesic active contours,” *International Journal of Computer Vision*, vol. 22, no. 11, pp. 61–79, 1997.
- [15] CHAN, T. and VESE, L., “Active contours without edges,” *Image Processing, IEEE Transactions on*, vol. 10, no. 2, pp. 266–277, 2001.
- [16] CONTURO, T., LORI, N., CULL, T., AKBUDAK, E., SNYDER, A., SHIMONY, J., MCKINSTRY, R., BURTON, H., and RAICHLE, M., “Tracking neuronal fiber pathways in the living human brain,” *Proc Natl Acad Sci US A*, vol. 96, no. 18, pp. 10422–10427, 1999.
- [17] COUCH II, L. W., *Digital and Analog Communication Systems*. New York, USA: Macmillan Publishing Company, 3rd ed., 1990.
- [18] DOCARMO, M., *Riemannian Geometry*. Springer-Verlag, 2003.
- [19] DUDA, R., HART, P., and OTHERS, *Pattern Classification and Scene Analysis*. Wiley New York, 1973.
- [20] FERLAY, J., BRAY, F., PISANI, P., and PARKIN., D. M., “GLOBOCAN 2002: Cancer incidence, mortality and prevalence worldwide,” tech. rep., IARC CancerBase No. 5. version 2.0, IARCPress, Lyon, France, 2004. <http://www-dep.iarc.fr/>.
- [21] FERRUCCI, J. T., “Colon cancer screening with virtual colonoscopy: Promise, polyps, politics,” *Am. J. Roentgenol.*, vol. 177, pp. 975–988, 2001.
- [22] FLEMING, W. and SONER, H., *Controlled Markov Processes and Viscosity Solutions*. Springer-Verlag, 2003.
- [23] FLETCHER, T., TAO, R., JEONG, W., and WHITAKER, R., “A volumetric approach to quantifying region-to-region white matter connectivity in diffusion tensor MRI,” *IPMI*, 2007.
- [24] FRIMAN, O., FARNEBÄCK, G., and WESTIN, C., “A Bayesian approach for stochastic white matter tractography,” *IEEE Transactions on Medical Imaging*, vol. 25, no. 8, p. 965, 2006.
- [25] GAGE, M., “Evolving plane curves by curvature in relative geometries,” *Duke J. Math.*, vol. 72, pp. 441–466, 1993.
- [26] GAGE, M. and HAMILTON, R., “The heat equation shrinking convex plane curves,” *J. Differential Geometry*, vol. 23, pp. 69–96, 1986.

- [27] GERING, D., NABAVI, A., KIKINIS, R., GRIMSON, W., HATA, N., EVERETT, P., JOLESZ, F., and WELLS, W., “An integrated visualization system for surgical planning and guidance using image fusion and interventional imaging,” *MICCAI 99: Proceedings of the Second International Conference on Medical Image Computing and Computer Assisted Intervention*, pp. 809–819.
- [28] GÖKTÜRK, S. B., TOMASI, C., BURAK, A., BEAULIEU, C. F., PAIK, D. S., BROOKE JEFFREY JR., R., YEE, J., and NAPEL, S., “A statistical 3-D pattern processing method for computer-aided detection of polyps in CT colonography,” *IEEE Trans. Medical Imaging*, vol. 20, pp. 1251–1260, Dec 2001.
- [29] GRAYSON, M., “The heat equation shrinks embedded plane curves to round points,” *Journal of Differential Geometry*, vol. 26, pp. 285–314, 1987.
- [30] HAGMANN, P., REESE, T. G., TSENG, W.-Y. I., MEULI, R., THIRAN, J.-P., and WEDEEN, V. J., “Diffusion spectrum imaging tractography in complex cerebral white matter: an investigation of the centrum semiovale,” in *ISMRM*, 2004.
- [31] HAKER, S., SAPIRO, G., and TANNENBAUM, A., “Knowledge-based segmentation of SAR data with learned priors,” *Image Processing, IEEE Transactions on*, vol. 9, no. 2, pp. 299–301, 2000.
- [32] HAREWOOD, G. C., WIERSEMA, M. J., and III, L. J. M., “A prospective, controlled assessment of factors influencing acceptance of screening colonoscopy,” *The American Journal of Gastroenterology*, vol. 97, pp. 3186–3194, Dec. 2002.
- [33] IBANEZ, L., SCHROEDER, W., NG, L., and CATES, J., “The ITK Software Guide. Kitware, Inc,” tech. rep., ISBN 1-930934-10-6, <http://www.itk.org/ItkSoftwareGuide.pdf>, 2003.
- [34] JACKOWSKI, M., KAO, C., QIU, M., CONSTABLE, R., and STAIB, L., “White matter tractography by anisotropic wavefront evolution and diffusion tensors imaging,” *Medical Image Analysis*, vol. 9, pp. 427–440, 2005.
- [35] JEMAL, A., SIEGEL, R., WARD, E., MURRAY, T., XU, J., and THUN, M. J., “Cancer statistics, 2007,” *CA Cancer J. Clin.*, vol. 57, no. 1, pp. 43–66, 2007.
- [36] JEREBKO, A., LAKARE, S., CATHIER, P., PERIASWAMY, S., and BOGONI, L., “Symmetric curvature patterns for colonic polyp detection,” in *Medical Image Computing and Computer-Assisted Intervention*, (Copenhagen, Denmark), pp. 169–176, Oct. 2006.
- [37] JONASSON, L., BRESSON, X., HAGMANN, P., CUISENAIRE, O., MEULI, R., and THIRAN, J., “White matter fiber tract segmentation in DT-MRI using geometric flows,” *Medical Image Analysis*, vol. 9, no. 3, pp. 223–236, 2005.

- [38] JONASSON, L., HAGMANN, P., POLLO, C., BRESSON, X., WILSON, C., MEULI, R., and THIRAN, J., “A level set method for segmentation of the thalamus and its nuclei in DT-MRI,” *Signal Processing*, vol. 87, no. 2, pp. 309–321, 2007.
- [39] KAO, C., OSHER, S., and QIAN, J., “Lax–Friedrichs sweeping scheme for static Hamilton–Jacobi equations,” *Journal of Computational Physics*, vol. 196, no. 1, pp. 367–391, 2004.
- [40] KAO, C., OSHER, S., and TSAI, Y., “Fast sweeping methods for static Hamilton–Jacobi equations,” *SIAM journal on numerical analysis*, vol. 42, no. 6, pp. 2612–2632, 2005.
- [41] KAPUR, T., “Model based three dimensional Medical Imaging Segmentation,” *Massachusetts Institute of Technology*, 1999.
- [42] KASS, R. and RAFTERY, A., “Bayes factors,” *J. Am. Stat. Assoc.*, vol. 90, pp. 773–795, Sep. 1995.
- [43] KICHENASSAMY, S., KUMAR, A., OLVER, P., TANNENBAUM, A., and YEZZI, A., “Conformal curvature flows: from phase transitions to active vision,” *Arch. Rational Mech. Anal.*, vol. 134, no. 3, pp. 275–301, 1996.
- [44] KIMMEL, R. and BRUCKSTEIN, A., “Regularized zero-crossings as optimal edge detectors,” *Int. Journal Computer Vision*, vol. 53, no. 3, pp. 225–243, 2003.
- [45] KISS, G., VAN CLEYNENBREUGEL, J., DRISIS, S., BIELEN, D., MARCHAL, G., and SUETENS, P., “Computer aided detection for low-dose CT colonography,” in *Medical Image Computing and Computer-Assisted Intervention*, (Palm Springs, USA), pp. 859–867, Oct. 2005.
- [46] KOLMORGOROV, V. and BOYKOV, Y., “What metrics can be approximated by geo-cuts or global optimization of length/area and flux,” in *Proceedings IEEE International Conference Computer Vision*, 2003.
- [47] KUBICKI, M., WESTIN, C., NESTOR, P., WIBLE, C., FRUMIN, M., MAIER, S., KIKINIS, R., JOLESZ, F., MCCARLEY, R., and SHENTON, M., “Cingulate fasciculus integrity disruption in schizophrenia: a magnetic resonance diffusion tensor imaging study,” *Biological Psychiatry*, vol. 54, no. 11, pp. 1171–1180, 2003.
- [48] LANGER, P. and TAKACS, A., “Why are taeniae, haustra, and semilunar folds differentiated in the gastrointestinal tract of mammals, including man?,” *J. Morph.*, vol. 259, no. 3, pp. 308–315, 2004.
- [49] LEFERE, P., GRYSPEERDT, S., BAEKELANDT, M., and VAN HOLSBEECK, B., “Laxative-free CT colonography,” *Am. J. Roentgenol.*, vol. 183, pp. 945–948, Oct. 2004.

- [50] LENGLET, C., ROUSSON, M., and DERICHE, R., “DTI segmentation by statistical surface evolution,” *IEEE Transactions on Medical Imaging*, vol. 25, no. 6, pp. 685–700, 2006.
- [51] LENGLET, C., ROUSSON, M., DERICHE, R., FAUGERAS, O., LEHERICY, S., and UGURBIL, K., “A Riemannian Approach to Diffusion Tensor Images Segmentation,” *Proceedings of the 19th International Conference on Information Processing in Medical Imaging (IPMI)*, Glenwood Springs, CO, USA, pp. 591–602, 2005.
- [52] LIN, Q., *Enhancement, extraction, and visualization of 3D volume data*. Department of Electrical Engineering, Linköping University, 2003.
- [53] MAGNUS, J. R. and NEUDECKER, H., *Matrix Differential Calculus with Applications in Statistics and Econometrics*. Wiley Series in Probability and Mathematical Statistics, New York: John Wiley & Sons, 1995.
- [54] MASSACHUSETTS GENERAL HOSPITAL, C. F. M. A., “Internet brain segmentation repository,” 1998. <http://www.cma.mgh.harvard.edu/ibsr/>.
- [55] MELONAKOS, J., GAO, Y., and TANNENBAUM, A., “Tissue tracking: applications for brain MRI classification,” in *Proceedings of SPIE*, vol. 6512, p. 651218, SPIE, 2007.
- [56] MELONAKOS, J., MENDONCA, P., BHOTKA, R., and SIROHEY, S., “A Probabilistic Model for Hausdorff Curvatures with Applications to Colon CAD,” *LECTURE NOTES IN COMPUTER SCIENCE*, vol. 4792, p. 420, 2007.
- [57] MELONAKOS, J., MOHAN, V., NIETHAMMER, M., SMITH, K., KUBICKI, M., and TANNENBAUM, A., “Finsler Tractography for White Matter Connectivity Analysis of the Cingulum Bundle,” *LECTURE NOTES IN COMPUTER SCIENCE*, vol. 4791, p. 36, 2007.
- [58] MELONAKOS, J., NIETHAMMER, M., MOHAN, V., KUBICKI, M., MILLER, J., and TANNENBAUM, A., “Locally-Constrained Region-Based Methods for DW-MRI Segmentation,” in *Computer Vision, 2007. ICCV 2007. IEEE 11th International Conference on*, pp. 1–8, 2007.
- [59] MELONAKOS, J., PICHON, E., ANGENENT, S., and TANNENBAUM, A., “Finsler Active Contours,” *IEEE Transactions on Pattern Analysis and Machine Intelligence*, vol. 30, no. 3, pp. 412–423, 2008.
- [60] MENDONCA, P. R. S., BHOTIKA, R., and MILLER, J. V., “Probability distribution of curvatures of isosurfaces in Gaussian random fields,” May 2007. arXiv.
- [61] MENDONÇA, P. R. S., BHOTIKA, R., ZHAO, F., and MILLER, J. V., “Lung nodule detection via Bayesian voxel labeling,” in *Information Processing in*

- Medical Imaging* (KARSSEMEIJER, N. and LELIEVELDT, B., eds.), (Kerkrade, The Netherlands), pp. 134–145, July 2007.
- [62] MOBERTS, B., VILANOVA, A., and VAN WIJK, J., “Evaluation of Fiber Clustering Methods for Diffusion Tensor Imaging,” *Visualization, IEEE 2005*, pp. 9–9, 2005.
  - [63] MOREL, J.-M. and SOLIMINI, S., *Variational Methods for Image Segmentation*. Birkhauser, 1994.
  - [64] MORI, S., CRAIN, B., CHACKO, V., and VAN ZIJL, P., “Three-dimensional tracking of axonal projections in the brain by magnetic resonance imaging,” *Ann Neurol*, vol. 45, no. 2, pp. 265–9, 1999.
  - [65] MORI, S. and VAN ZIJL, P., “Fiber tracking: principles and strategies- a technical review,” *NMR in Biomedicine*, vol. 15, no. 7-8, pp. 468–480, 2002.
  - [66] MORTENSEN, E., MORSE, B., BARRETT, W., and UDUPA, J., “Adaptive boundary detection using live-wire two-dimensional dynamic programming,” in *IEEE Proceedings of Computers in Cardiology*, pp. 635–638, 1992.
  - [67] MULSHINE, J. L., “Clinical issues in the management of early lung cancer,” *Clin. Cancer Res.*, vol. 11, pp. 4993s–4998, July 2005.
  - [68] MUMFORD, D., “Bayesian rationale for energy functionals,” in *Geometry-driven diffusion in Computer Vision*, pp. 141–153, 1994.
  - [69] NIETHAMMER, N., ZACH, C., MELONAKOS, J., and TANNENBAUM, A., “Near-Tubular Fiber Bundle Segmentation for Diffusion Weighted Imaging: Segmentation Through Frame Reorientation,” *NeuroImage*, 2008. accepted for submission.
  - [70] OAKS, J. A., “Singularities and self-intersections of curves evolving on surfaces,” *Indiana Univ. Math. J.*, vol. 43, no. 3, pp. 959–981, 1994.
  - [71] O’DONNELL, L., “Cerebral white matter analysis using diffusion imaging,” 2006.
  - [72] OLVER, P., SAPIRO, G., and TANNENBAUM, A., “Invariant Geometric Evolutions of Surfaces and Volumetric Smoothing,” *SIAM Journal on Applied Mathematics*, vol. 57, no. 1, pp. 176–194, 1997.
  - [73] OSHER, S. and FEDKIW, R., *Level Set Methods and Dynamic Implicit Surfaces*. Springer Verlag, 2003.
  - [74] O’DONNELL, L., HAKER, S., and WESTIN, C., “New Approaches to Estimation of White Matter Connectivity in Diffusion Tensor MRI: Elliptic PDEs and Geodesics in a Tensor-Warped Space,” *Computing and Computer Assisted Intervention, LNCS*, vol. 2488, pp. 459–466, 2002.

- [75] PAIK, D. S., BEAULIEU, C. F., RUBIN, G. D., ACAR, B., JEFFREY, JR., R. B., YEE, J., DEY, J., and NAPEL, S., “Surface normal overlap: A computer-aided detection algorithm with application to colonic polyps and lung nodules in helical CT,” *IEEE Trans. Medical Imaging*, vol. 23, pp. 661–675, June 2004.
- [76] PARKER, G., HAROON, H., and WHEELER-KINGSHOTT, C., “A framework for a streamline-based probabilistic index of connectivity(PICo) using a structural interpretation of MRI diffusion measurements,” *Journal of Magnetic Resonance Imaging*, vol. 18, no. 2, pp. 242–254, 2003.
- [77] PARKER, G., WHEELER-KINGSHOTT, C., and BARKER, G., “Estimating distributed anatomical connectivity using fast marching methods and diffusion tensor imaging,” *Medical Imaging, IEEE Transactions on*, vol. 21, no. 5, pp. 505–512, 2002.
- [78] PERRIN, M., POUPON, C., COINTEPAS, Y., RIEUL, B., GOLESTANI, N., PALLIER, C., RIVIERE, D., CONSTANTINESCO, A., and LE BIHAN, D., “Fiber tracking in Q-ball fields using regularized particle trajectories,” *Proc. of IPMI*, vol. 2, no. 3, 2005.
- [79] PICHON, E., *Novel methods for multidimensional image segmentation*. PhD thesis, Georgia Institute of Technology, 2005.
- [80] PICHON, E., SAPIRO, G., and TANNENBAUM, A., *Directions in Mathematical Systems Theory and Optimization*, ch. Segmentation of diffusion tensor imagery, pp. 239–247. No. 286 in LNCIS, 2003.
- [81] PICHON, E. and TANNENBAUM, A., “Curve Segmentation Using Directional Information, Relation to Pattern Detection,” in *Image Processing, 2005. ICIP 2005. IEEE International Conference on*, vol. 2, 2005.
- [82] PICHON, E., WESTIN, C., and TANNENBAUM, A., “A Hamilton-Jacobi-Bellman approach to high angular resolution diffusion tractography,” *Eighth International Conference on Medical Image Computing and Computer-Assisted Intervention. Lecture Notes in Computer Science*, vol. 3749, pp. 180–187, 2005.
- [83] PICKHARDT, P., “Target lesion: The radiologist’s perspective,” in *Sixth International Symposium on Virtual Colonoscopy*, (Boston, MA), pp. 60–62, Oct 2005.
- [84] POHL, K., FISHER, J., GRIMSON, W., KIKINIS, R., and WELLS, W., “A bayesian model for joint segmentation and registration,” *NeuroImage*, vol. 31, no. 1, pp. 228–239, 2006.

- [85] PRADOS, E., LENGLET, C., PONS, J., WOTAWA, N., DERICHE, R., FAUGERAS, O., and SOATTO, S., “Control Theory and Fast Marching Techniques for Brain Connectivity Mapping,” *Proceedings of the 2006 IEEE Computer Society Conference on Computer Vision and Pattern Recognition-Volume 1*, pp. 1076–1083, 2006.
- [86] RAJAPAKSE, J. and KRUGGEL, F., “Segmentation of MR images with intensity inhomogeneities,” *IMAGE VISION COMPUT*, vol. 16, no. 3, pp. 165–180, 1998.
- [87] RATHI, Y., MICHAILOVICH, O., MALCOLM, J., and TANNENBAUM, A., “Seeing the unseen: Segmenting with distributions,” in *Intl. Conf. Signal and Image Processing*, 2006.
- [88] ROUSSON, M., LENGLET, C., and DERICHE, R., “Level Set and Region Based Surface Propagation for Diffusion Tensor MRI Segmentation,” *Computer Vision and Mathematical Methods in Medical and Biomedical Image Analysis*, vol. 3, no. 5, p. 36, 2004.
- [89] SAPIRO, G., *Geometric Partial Differential Equations and Image Analysis*. Cambridge University Press, 2001.
- [90] SCHMAHMANN, J. and PANDYA, D., *Fiber Pathways of the Brain*. Oxford University Press, 2006.
- [91] SEGONNE, F., DALE, A., BUSA, E., GLESSNER, M., SALAT, D., HAHN, H., and FISCHL, B., “A hybrid approach to the skull stripping problem in MRI,” *NeuroImage*, vol. 22, no. 3, pp. 1060–1075, 2004.
- [92] SETHIAN, J., *Level Set Methods and Fast Marching Methods*. Cambridge University Press, 1999.
- [93] SETHIAN, J. and VLADIMIRSKY, A., “Ordered upwind methods for static Hamilton-Jacobi equations: Theory and applications,” *SIAM J. Numerical Analysis*, vol. 41, no. 1, pp. 325–363, 2003.
- [94] SMITH, R. A., COKKINIDES, V., and EYRE, H. J., “American cancer society guidelines for the early detection of cancer, 2006,” *CA Cancer J. Clin.*, vol. 56, pp. 11–25, Jan/Feb 2006.
- [95] SONER, H., “Dynamic programming and viscosity solutions,” in *Proceedings of Annual AMS Meeting*, AMS, 1999.
- [96] SPIVAK, M., *Introduction to Differential Geometry, Volume 2*. Publish or Perish, Boston, 1974.
- [97] SPIVAK, M., *A Comprehensive Introduction to Differential Geometry*, vol. III. Houston, TX, USA: Publish or Perish, 3rd ed., 1999.

- [98] SPRAYCAR, M., ed., *PDR Medical Dictionary*. Baltimore, MD: Williams and Wilkins, 1st ed., 1995.
- [99] STIELTJES, B., KAUFMANN, W., VAN ZIJL, P., FREDERICKSEN, K., PEARLSON, G., SOLAIYAPPAN, M., and MORI, S., “Diffusion Tensor Imaging and Axonal Tracking in the Human Brainstem,” *NeuroImage*, vol. 14, no. 3, pp. 723–735, 2001.
- [100] SUMMERS, R. M., JOHNSON, C. D., PUSANIK, L. M., D., M. J., YOUSSEF, A. M., and REED, J. E., “Automated polyp detection at CT colonography: Feasibility assessment in a human population,” *Radiology*, vol. 219, pp. 51–59, 2001.
- [101] SUMMERS, R. M., YAO, J., and ET AL, P. P. J., “Computed tomographic virtual colonoscopy computer-aided polyp detection in a screening population,” *Gastroenterology*, vol. 129, pp. 1832–1844, Dec 2005.
- [102] SUMMERS, R. M., BEAULIEU, C. F., PUSANIK, L. M., MALLEY, J. D., JEFFREY, R. BROOKE, J., GLAZER, D. I., and NAPEL, S., “Automated polyp detector for CT colonography: Feasibility study,” *Radiology*, vol. 216, no. 1, pp. 284–290, 2000.
- [103] TAO, X. and MILLER, J. V., “A method for registering diffusion weighted magnetic resonance images,” in *MICCAI (2)* (LARSEN, R., NIELSEN, M., and SPORRING, J., eds.), vol. 4191 of *Lecture Notes in Computer Science*, pp. 594–602, Springer, 2006.
- [104] TEO, P., SAPIRO, G., and WANDELL, B., “Anisotropic smoothing of posterior probabilities,” *Image Processing, 1997. Proceedings., International Conference on*, vol. 1, 1997.
- [105] TEO, P., SAPIRO, G., and WANDELL, B., “Creating connected representations of cortical gray matter for functional MRI visualization,” *Medical Imaging, IEEE Transactions on*, vol. 16, no. 6, pp. 852–863, 1997.
- [106] TSITSIKLIS, J. N., “Efficient algorithms for globally optimal trajectories,” *IEEE Transactions on Automatic Control*, vol. 50, no. 9, pp. 1528–1538, 1995.
- [107] TU, Z., ZHOU, X. S., BOGONI, L., BARBU, A., and COMANICIU, D., “Probabilistic 3D polyp detection in CT images: The role of sample alignment,” in *Proc. Conf. Computer Vision and Pattern Recognition*, vol. II, (New York, USA), pp. 1544–1551, June 2006.
- [108] VAN LEEMPUT, K., MAES, F., VANDERMEULEN, D., and SUETENS, P., “Automated model-based tissue classification of MR images of the brain,” *Medical Imaging, IEEE Transactions on*, vol. 18, no. 10, pp. 897–908, 1999.

- [109] VAN WIJK, C., VAN RAVESTEIJN, V. F., VOS, F. M., TRUYEN, R., DE VRIES, A. H., STOKER, J., and VAN VLIET, L. J., "Detection of protrusions in curved folded surfaces applied to automated polyp detection in CT colonography," in *Medical Image Computing and Computer-Assisted Intervention*, (Copenhagen, Denmark), pp. 471–478, Oct. 2006.
- [110] VASILEVSKY, A. and SIDDIQI, K., "Flux maximizing geometric flows," *IEEE PAMI*, vol. 24, pp. 1565–1579, December 2002.
- [111] VOS, F. M., SERLIE, I. W. O., VAN GELDER, R. E., POST, F. H., TRUYEN, R., GERRITSEN, F. A., STOKER, J., and VOSSEPOEL, A. M., "A new visualization method for virtual colonoscopy," in *Medical Image Computing and Computer-Assisted Intervention*, (Berlin), pp. 645–654, 2001.
- [112] WANG, F., SUN, Z., CUI, L., DU, X., WANG, X., ZHANG, H., CONG, Z., HONG, N., and ZHANG, D., "Anterior Cingulum Abnormalities in Male Patients With Schizophrenia Determined Through Diffusion Tensor Imaging," 2004.
- [113] WESTIN, C.-F., MAIER, S. E., KHIDHIR, B., EVERETT, P., JOLESZ, F. A., and KIKINIS, R., "Image processing for diffusion tensor magnetic resonance imaging," in *MICCAI*, pp. 441–452, 1999.
- [114] WHITAKER, R., "A Level-Set Approach to 3D Reconstruction from Range Data," *International Journal of Computer Vision*, vol. 29, no. 3, pp. 203–231, 1998.
- [115] YANG, Y., TANNENBAUM, A., and GIDDENS, D., "Knowledge-based 3D segmentation and reconstruction of coronary arteries using CT images," *Engineering in Medicine and Biology Society, 2004. EMBC 2004. Conference Proceedings. 26th Annual International Conference of the*, vol. 1, 2004.
- [116] YOSHIDA, H. and NÄPPI, J., "Three-dimensional computer-aided diagnosis scheme for detection of colonic polyps," *IEEE Trans. Medical Imaging*, vol. 20, pp. 1261–1274, Dec. 2001.
- [117] YOUNG, L. C., *Calculus of Variations and Optimal Control Theory*. W. B. Saunders Company, 1969.
- [118] ZIJDENBOS, A., DAWANT, B., MARGOLIN, R., and PALMER, A., "Morphometric analysis of white matter lesions in MR images: method and validation," *Medical Imaging, IEEE Transactions on*, vol. 13, no. 4, pp. 716–724, 1994.